การจับยึดคาร์บอนไดออกไซด์จากฟลูแก๊สโดยตัวดูดซับฐานโพแทสเซียมในฟลูอิไดซ์เบดแบบปั่นป่วนหมุนเวียน

นางสาวพิไลวรรณ ไชยวัง

วิทยานิพนธ์นี้เป็นส่วนหนึ่งของการศึกษาตามหลักสูตรปริญญาวิทยาศาสตรดุษฎีบัณฑิต
สาขาวิชาเคมีเทคนิค ภาควิชาเคมีเทคนิค
คณะวิทยาศาสตร์ จุฬาลงกรณ์มหาวิทยาลัย
ปีการศึกษา 2559

CO_2 CAPTURE FROM FLUE GAS BY POTASSIUM-BASED SORBENT IN CIRCULATING-TURBULENT FLUIDIZED BED

Miss Pilaiwan Chaiwang

A Dissertation Submitted in Partial Fulfillment of the Requirements
for the Degree of Doctor of Philosophy Program in Chemical Technology
Department of Chemical Technology
Faculty of Science
Chulalongkorn University
Academic Year 2016

Thesis Title	CO_2 CAPTURE FROM FLUE GAS BY POTASSIUM-BASED SORBENT IN CIRCULATING-TURBULENT FLUIDIZED BED
By	Miss Pilaiwan Chaiwang
Field of Study	Chemical Technology
Thesis Advisor	Professor Pornpote Piumsomboon, Ph.D.
Thesis Co-Advisor	Associate Professor Benjapon Chalermsinsuwan, Ph.D. Professor Dimitri Gidaspow, Ph.D.

Accepted by the Faculty of Science, Chulalongkorn University in Partial Fulfillment of the Requirements for the Doctoral Degree

....Dean of the Faculty of Science
(Associate Professor Polkit Sangvanich, Ph.D.)

THESIS COMMITTEE

....Chairman
(Associate Professor Prasert Reubroycharoen, Ph.D.)

....Thesis Advisor
(Professor Pornpote Piumsomboon, Ph.D.)

....Thesis Co-Advisor
(Associate Professor Benjapon Chalermsinsuwan, Ph.D.)

....Thesis Co-Advisor
(Professor Dimitri Gidaspow, Ph.D.)

....Examiner
(Associate Professor Prapan Kuchonthara, Ph.D.)

....Examiner
(Professor Pattarapan Prasassarakich, Ph.D.)

....External Examiner
(Boonrod Sajjakulnukit, Ph.D.)

พิไลวรรณ ไชยวัง : การจับยึดคาร์บอนไดออกไซด์จากฟลูแก๊สโดยตัวดูดซับฐานโพแทสเซียมในฟลูอิไดซ์เบดแบบปั่นป่วนหมุนเวียน (CO_2 CAPTURE FROM FLUE GAS BY POTASSIUM-BASED SORBENT IN CIRCULATING-TURBULENT FLUIDIZED BED) อ.ที่ปรึกษาวิทยานิพนธ์หลัก: ศ. ดร. พรพจน์ เปี่ยมสมบูรณ์, อ.ที่ปรึกษาวิทยานิพนธ์ร่วม: รศ. ดร. เบญจพล เฉลิมสินสุวรรณ, Dimitri Gidaspow, 164 หน้า.

งานวิจัยนี้มีวัตถุประสงค์เพื่อศึกษากระบวนการจับยึดแก๊สคาร์บอนไดออกไซด์ด้วยตัวดูดซับของแข็งในเครื่องปฏิกรณ์ฟลูอิไดซ์เบดแบบหมุนเวียน จากผลการวิจัยก่อนหน้าพบว่าสภาพการไหลในเครื่องปฏิกรณ์ฟลูอิไดซ์เบดในช่วงการไหลแบบปั่นป่วนหมุนเวียนเป็นรูปแบบที่จะส่งเสริมการทำงานของตัวดูดซับของแข็งได้ดีเนื่องจากสภาพการไหลดังกล่าวได้รวมข้อดีของช่วงการไหลแบบฟูลอิไดเซชันแบบความเร็วสูงและช่วงการไหลแบบปั่นป่วน ตัวดูดซับที่ใช้ในงานวิจัยนี้คือโพแทสเซียมคาร์บอเนตบนตัวรองรับอะลูมินา งานวิจัยจึงเริ่มจากการหาภาวะดำเนินการที่ทำให้อุทกพลศาสตร์ภายในเครื่องปฏิกรณ์อยู่ในช่วงการไหลแบบปั่นป่วนหมุนเวียน จากผลทดลองพบว่า ภาวะดังกล่าวเกิดขึ้นเมื่อใช้ความเร็วแก๊ส 1.0 เมตรต่อวินาที โดยพิจารณาได้จากการกระจายตัวของอนุภาคในแนวดิ่งในช่วงการไหลดังกล่าวจะมีความสม่ำเสมอตลอดความสูงของท่อไรเซอร์ ในการศึกษานี้พบว่าสัดส่วนโดยปริมาตรของแข็งเฉลี่ยอยู่ที่ 0.15 ต่อมาทำการศึกษาจลนศาสตร์ของการดูดซับภายใต้ช่วงการไหลแบบต่างๆ ในเครื่องปฏิกรณ์ฟลูอิไดซ์เบดเพื่อกำหนดค่าพารามิเตอร์ของปฏิกิริยาโดยใช้แบบจำลองการเสื่อมสภาพเป็นเครื่องมืออธิบายปรากฏการณ์ ค่าพารามิเตอร์ของแบบจำลองแสดงให้เห็นว่าจลนศาสตร์ของปฏิกิริยาการดูดซับที่เกิดภายใต้ช่วงการไหลแบบปั่นป่วนหมุนเวียนมีค่าใกล้เคียงกับช่วงการไหลแบบฟองแก๊ส เพื่อความสมบูรณ์ของระบบดักจับแก๊สคาร์บอนไดออกไซด์ งานวิจัยนี้ได้ศึกษาเครื่องปฏิกรณ์ด้านดาวเนอร์ที่ทำหน้าคืนสภาพตัวดูดซับ โดยศึกษาอุทกพลศาสตร์และจลนศาสตร์ที่เกิดขึ้นภายในเครื่องปฏิกรณ์นี้ การศึกษาอุทกพลศาสตร์ทำโดยการจำลองพลศาสตร์ของไหลด้วยวิธีการคำนวณแบบสองมิติ ด้วยการปรับเปลี่ยนความดันลด (0.90 ถึง 0.99 atm) ภายในเครื่องปฏิกรณ์ และการปรับอัตราการหมุนเวียนของของแข็งในระบบ (250 ถึง 1000 kg/m^2 s) ผลที่ได้พบว่า เมื่ออัตราการหมุนเวียนของอนุภาคในระบบมีค่าต่ำ อนุภาคจะมี mean free path มากกว่าเมื่ออัตราการหมุนเวียนของอนุภาคในระบบมีค่าสูง สำหรับการศึกษาจลนศาสตร์ของการคืนสภาพของโพแทสเซียมไฮโดรเจนคาร์บอเนต ทำโดยใช้วิธีเทอร์โมกราวิเมทริกแบบอุณหภูมิไม่คงที่เพื่อหาค่าพารามิเตอร์ทางจลนศาสตร์และใช้แบบจำลองเชิงวิเคราะห์ ในการคำนวณค่าการคืนสภาพของโพแทสเซียมไบคาร์บอเนต

ภาควิชา เคมีเทคนิค
สาขาวิชา เคมีเทคนิค
ปีการศึกษา 2559

ลายมือชื่อนิสิต ....
ลายมือชื่อ อ.ที่ปรึกษาหลัก ....
ลายมือชื่อ อ.ที่ปรึกษาร่วม ....
ลายมือชื่อ อ.ที่ปรึกษาร่วม ....

5373816523 : MAJOR CHEMICAL TECHNOLOGY
KEYWORDS: CO2 CAPTURE / FLUIDIZATION / COMPUTATIONAL FLUID DYNAMIC / KINETIC

PILAIWAN CHAIWANG: CO_2 CAPTURE FROM FLUE GAS BY POTASSIUM-BASED SORBENT IN CIRCULATING-TURBULENT FLUIDIZED BED. ADVISOR: PROF. PORNPOTE PIUMSOMBOON, Ph.D., CO-ADVISOR: ASSOC. PROF. BENJAPON CHALERMSINSUWAN, Ph.D., PROF. DIMITRI GIDASPOW, Ph.D., 164 pp.

The purpose of this research is to study the carbon dioxide capture process using solid sorbent in a circulating fluidized bed reactor. From previous research work, it was found that the hydrodynamics under circulating turbulent fluidized bed (CTFB) regime can promote the solid sorbent for CO_2 capture process, due to the combination of advantages of fast fluidization and turbulent regimes. The solid sorbent being used in this study was potassium carbonate on alumina supporter. The study started with finding the operating condition in the riser so that the particles flow in the reactor fell in the circulating turbulent fluidization regime. The experiment showed that when the gas velocity is 1 m/s, the flow will be performed in the CTFB regime and it was confirmed by the uniform distribution of solid volume fraction along the riser. The solid volume fraction in this case was 0.15. Then, the kinetic of the adsorption under several operating flow regimes in the riser was studied and the kinetic parameters corresponding to each regime were determined using deactivation kinetic model. The estimated parameters showed that the kinetic of the circulating turbulent fluidized bed and the bubbling fluidized bed were quite similar. For the completion of the system, the research also studied the downer reactor which functions to regenerate the spent sorbent by studying the hydrodynamics and kinetic inside the reactor. The hydrodynamic was studied by using 2D computational fluid dynamic model. The adjustment of pressure drop (0.90 – 0.99 atm) and recirculating rate of the particles (250 – 1000 $kg/m^2.s$) were simulated and the results showed that the particles have higher mean free path when the recirculating rate of the particles was lower. For the kinetic of $KHCO_3$ sorbent regeneration, the thermogravimetric method was conducted under nonisothermal condition to determine the kinetic parameters and the analytical method model was selected to represent the regeneration model.

Department: Chemical Technology
Field of Study: Chemical Technology
Academic Year: 2016

Student's Signature ....
Advisor's Signature ....
Co-Advisor's Signature ....
Co-Advisor's Signature ....

ACKNOWLEDGEMENTS

First of all, I would like to extend my heartfelt gratitude to my adviser, Prof. Dr. Pornpote Piumsomboon, without his advice, never-ending patience, and seemingly inexhaustible knowledge of mathematical models of my research would not have been completed.

It is impossible to thank him enough for his time and effort. He is without a doubt the best teacher I have ever known and I have learned so much through the graduate school experience because of him. And also Assoc. Dr. Benjapon Chalermsinsuwan and Prof. Dr. Dimitri Gidaspow through the graduate school experience.

I gratefully acknowledge the full financial support of the The Thailand Research Fund (TRF) and Chulalongkorn University, under the Royal Golden Jubilee Ph.D. Program. I would also like to thank all the members of the Cybernetics Research Laboratory for the meaningful discussions and great friendships.

Finally, no one has supported and encourage me more over the course of my graduate work than my family and friends. I want to thank my parents for always supporting me in all of my endeavors.

CONTENTS

Page

Page

LIST OF FIGURES

Page

LIST OF TABLE

Page

Chapter I

Introduction

1. Background information and problem statement

Growth of the economy, quality of life and well-being of the people leads to demand for more energy consumption. From the previous research, they discovered that more than 70 percent of fuel for electrical generation in Thailand comes from natural gas [1]. Therefore, the primary energy resource that can be used instead of natural gas is coal and biomass since they are abundant and the latter is renewable. However, It is quite clear that coal will continue to be used as a fuel in power plants. However, coal has limitation due to the issue of greenhouse gas emissions. Carbon dioxide (CO_2) is the primary greenhouse gas produced by the conventional energy source. At present, the power plants are focused on the strategy for increasing the highly efficient energy conversion and the elimination of CO_2 from the waste gas of burning. Therefore, there are several methods have been studied by many researchers for carbon dioxide capture.

In recent years, a solid sorbent method has been reported in many literatures as an innovative concept for capturing carbon dioxide from flue gas due to the cost-effective and energy efficient. Many researchers have been studied a solid sorbents containing alkali and alkali earth metals for carbon dioxide sorption (Na_2CO_3 and K_2CO_3) [2-11]. The various types of support materials that are supported on K-based sorbent are investigated, such as activated carbon, TiO_2, MgO, ZrO_2, Al_2O_3, CaO, SiO_2 and Zeolite [2, 3]. One of the efficient techniques to eliminate carbon dioxide is the chemical absorption of carbon dioxide with dry alkali-metal carbonate (Na_2CO_3 or K_2CO_3) sorbent. This separation technique has been widely used to capture carbon dioxide from flue gas. However, the carbonation reaction rate of Na_2CO_3 was rather slow. The attrition resistance (AI) and the corrected attrition index (CAI) of K_2CO_3 are higher than those of Na_2CO_3 sorbent [5, 6, 12].

The system for carbon dioxide (CO_2) capture with dry regenerable potassium carbonate sorbent consists of carbonation and regeneration reactions. The following reaction occurs in each reactor.

Carbonation: $K_2CO_3(s) + CO_2(g) + H_2O(g) \leftrightarrow 2KHCO_3(s) + \text{Heat}$ (1.1)

For continuous processes, the sorbent must be rapidly regenerated after the carbonation reaction. So the $KHCO_3$ is then removed from the carbonation reactor and delivered to the regeneration reactor.

Regeneration: $2KHCO_3(s) \leftrightarrow K_2CO_3(s) + CO_2(g) + H_2O(g)$ (1.2)

The forward reaction in Eq.(1.1) is an exothermic reaction, so heat transfer will be important factors that have to be controlled carefully in the carbonation reaction. Thus, a fluidized-bed reactor can be a good solution for this gas-solid process in order to avoid hot spot formation which can lead to solid sorbent degradation. The characteristic of fluidized-bed system describe as two-phase flow in a vertical direction. The advantages of this fluidized-bed system are improving the contact between gas and solid in the reactor, lacking of bubbles, making up solid conveniently and excellent mixing of the reactant [13].

Fluidization has been widely applied for many industrial processes involving gas-solid contact such as combustion, gasification, calcination and etc. In general, there are four types of flow regimes to clarify the fluidization behavior. It is consisting of bubbling (slugging) fluidization, turbulent fluidization, fast fluidization and pneumatic transport. The most operational regimes in commercial gas-solid fluidized-bed reactors are the turbulent and fast fluidization regimes [14]. Recently, a novel circulating-turbulent fluidized bed was discovered as a new regime which is combining the advantage of circulating fluidized bed and turbulent fluidized bed. The flow behavior in the circulating-turbulent fluidized bed is characterized by its nature which is different from those in circulating fluidized bed (CFB), turbulent fluidization bed (TFB) and high density circulating fluidized bed (HDCFB) reactors. The hydrodynamic behavior of a high-flux gas-solid fluidized bed is described by a complex interaction between the individual phases. Previous studies indicated that this flow has high solid concentration at the bottom of the riser and dilute solid concentration in the upper section. Furthermore, there is also an area of solid dilution at the center zone with high velocities for both fluid and solids. It also has high solid concentration near the wall. This phenomenon is called core-annulus [15, 16]. However, the circulating-turbulent fluidized bed can be operated at low superficial gas velocities and high solids circulation rate, resulting in a high density and uniform axial flow characteristics [14, 17]. To improve the understanding of fluidized bed such as fluid flow and chemical reactions behaviors for applying in many novel applications, computational fluid dynamics (CFD) simulation is a modern tool that is appropriate for multiphase flow studies, such as fluidization.

Computational fluid dynamics (CFD) is a popular numerical method and algorithm to solve problems. It uses for analyzing phenomena associated with the flow of fluid and chemical reactions. An important characteristic of the CFD is its capability of precise multiphysics-flow simulations such as a conjugate heat transfer with non-isothermal flow, fluid-structure interactions, non-Newtonian flow with viscous heating, and fluids with concentration-dependent viscosity. Porous-media flow user interfaces is available and it allows for isotropic or anisotropic media, as well as automatically combined free flow and porous domains. Tools for modeling of stirring vessels with rotating parts are available for both 2D and 3D flows. Kinetic theory of granular flow (KTGF) approaches is commonly used for simulating flows in the riser section of a circulating fluidized bed [17, 18].

1.2 Research objectives

1. Design and simulate a two-dimensional circulating fluidized bed reactor using computational fluid dynamics which regenerate sorbent by pressure process in the downer.

2. Determine the operating condition to operate the reactor in a circulating turbulent fluidized bed (CTFB) regime.

3. Study the chemical kinetics and reaction rate of adsorption of potassium carbonate in a circulating turbulent fluidized bed regime.

1.3 Scope of the Dissertation

1. Design and construct a fluidized bed model to operate in the real experiment and two-dimensional simulation using computational fluid dynamics.
2. Design a binary mixture of solid particles of a sorber for CO_2 capture without bubbles.
3. Investigate the effect of the hydrodynamics flow characteristic of circulating-turbulent fluidized bed regime.
4. Find the CO_2 capture breakthrough on circulating-turbulent fluidized bed regime on potassium carbonate solid sorbent.
5. Develop the chemical kinetics and reaction rate of adsorption and regeneration of potassium carbonate solid sorbent.

1.4 Anticipated benefits

1. Obtain an effective flow and the adsorption rate of the novel circulating-turbulent fluidized bed flow pattern/regime operation.

2. Find the optimum condition for CO_2 regeneration using reducing pressure.

1.5 Format of the Dissertation

The dissertation is divided into six chapters, Chapter I: background information and problem statement, propose and scope of this study were exhibited.

In Chapters II, CO_2 capture systems and theoretical description of fluidization and the detailed each fluidization flow regime characteristics, including a circulating turbulent fluidized bed (C-TFB) and further studies were reviewed.

In Chapters III, the methodology in the CO_2 capture and basic concept of computational fluid dynamics (CFD) with the kinetic theory based were presented.

In Chapters IV, the design of downer modeled using the multiphase kinetic theory of granular flow in hydrodynamics behaviors was studied.

In Chapters V, the chemical kinetic for regeneration of potassium carbonate solid sorbent using temperature was evaluated.

In Chapters VI, the flow pattern/regime characteristics of C-TFB and CO_2 adsorption capacity in this flow characteristics were discussed. Materials used in this work and the performance of CO_2 desorption downer-regenerator was discussed.

In Chapters VII, the final conclusions and recommendations for the future study were provided.

Chapter II

Theory and literature reviews

2.1 CO_2 capture systems

The advances of modern technology leads to the increase of energy demand. Currently, most of energy supplies come from fossil fuels in terms of cost and quantity. Fossil fuels, including coals, natural gas and oil, become useful sources for heat, electricity and transportation. Combustion is an essential reaction for energy production. It releases energy and emits flue gases, when fossil fuel, such as coal, is used. The major problem for using a primary fossil fuel combustion is CO_2 released into the atmosphere causing global warming. Therefore, capturing CO_2 is the main procedures for carbon storage and sequestration (CSS) process. Up to now, four main approaches are widely used depending on power plant processes: pre-combustion capture, post-combustion capture, oxy-combustion and chemical looping combustion as shown in Fig. 2.1.

2.1.1 Pre-combustion capture

Almost pure O_2 stream being produced from the air separation unit (ASU) is reacted with fuels in the gasifier to form syngas which is mainly composed of CO and H_2. Syngas is transferred into the shift reactor, adding up with the steam, then CO is converted into CO_2 and H_2O is converted to H_2 from water gas shift reaction. From this reaction, CO_2 is possibly obtained high concentrations (normally 15-60% by volume on dry basis) and the high pressures. After compression and dehydration, a high concentrate CO_2 separated from the gas stream is ready for storage and transportation. H_2 with less carbon emission is used burnt and driven a gas turbine to generate electricity and heatl. A recovery of an excess heat from a turbine can be used for a steam turbine is an optional. Pre-combustion capture applications are favorable for separating CO_2, though it has the complexity of initial fuel conversion methods and the high-price compared with post-combustion capture applications. The power plants used these applications that operate as a integrated gasification combined cycle (IGCC) technology.

2.1.2 Post-combustion capture

When the exhaust of fossil fuel combustion process, mainly containing small concentrations of CO_2 approximately 3-15% by volume and water vapor, are penetrated into this process, CO_2 is separated and then released clean gas. The obtained CO_2 is compressed and transformed into solid or liquid compound by absorption for transportation and sequestration. Several applications are used for separating CO_2, including amine solvent absorption, low-temperature adsorbent, membrane separation, ionic liquids, cryogenic separate, etc. [19]. Due to the separation after the combustion, the post-combustion capture system is a suitable process for the existing power plants. Typically, the MEA absorption is widely used for post-capture technique at the present for a modern pulverized coal (PC) power plant or a natural gas combined cycle (NGCC) power plant.

2.1.3 Oxy-combustion capture

In this system it requires a purified O_2 with concentration greater than 95% from the air separation unit (ASU) for combustion. Fossil fuels are burned in the O_2 atmosphere, diluted with recycle of the containing of flue gas to maintain temperature systems, instead of an absent N_2, to carry heat to unit operations. The gas products from the systems consist of CO_2 and water vapor. Water vapor can be condensed by cooling water and then separated from the stream to refine higher CO_2 concentration. In this application, the content of CO_2 is higher than 80% by volume. The additional unit operation may also need to remove minor impurities in the high concentration of CO_2 stream which adds more operating cost. Besides, comparing with the post-combustion systems, the efficiency of oxy-combustion systems reduces significantly due to the O_2 production [20].

2.1.4. Chemical looping

Chemical looping combustion system is another alternative. It can be presented for both oxy-combustion and pre-combustion capture systems. Since this alternative process is an indirect fuel combustion since the system has intermediate carrying oxygen between fuel and air reactors. Metal oxide in air reactor is used as an oxygen carrier to produce high concentration of O_2, as well as pre-combustion, and transferred to a fuel reactor where the combustion with fossil fuels takes place. The released gases in fuel reactor are CO_2 and water vapor while air reactor is generated small amount of O_2, N_2 and heat [21].

For the existing fossil fuel power plants, post-combustion CO_2 capture is an appropriate approach when compared with the others. Since post-combustion capture approach has no radical changes while using among the system which is easy to operate. Several techniques, widespread for separating and capturing CO_2, can be described in section 2.2.

2.2 CO_2 capture technologies

A widely practice post-combustion CO_2 capture process technologies consist of

2.2.1 CO_2 Absorption

2.2.2 CO_2 Adsorption

2.2.3 Cryogenics separation

2.2.4 Membranes absorption

2.2.1 CO_2 Absorption

For adsorption process, the condition of physical absorption is to operate at a high pressure and a low temperature based on Henry's law. CO_2 is absorbed through an absorbent and desorbed with pressure reduction and heating or both. At low partial pressures of CO_2 in typical flue gas, which is lower than 15%vol, physical absorption is not suitable for CO_2 capture from combustion generated by power plants due to the lack of driving force [22]. However, chemical absorption with amines are well-known absorbents used for removing CO_2 from flue gas during the fossil fuels combustion of the power plants in the United States.

Various types of alkanolamines in chemical absorption processes in a low partial pressure. The degree of nitrogen substituted with at least one amine group and hydrogen atom could separate amine into primary, secondary and tertiary which are Monoethanolamine (MEA), Diethanolamine (DEA) and Triethanolamine (TEA), respectively. The order of an amine group indicates the CO_2 reactivity. Hence, MEA has the fastest reaction rate when compared with the others [23]. The advantages of chemical absorption using MEA are low costs and operation taking place at an atmospheric pressure and low temperature. The overall reaction can be described from the following equations and Fig 2.2 illustrates amine-based absorption flow diagram processes [24].

$$CO_2 + R_1R_2NH \Leftrightarrow R_1R_2NCOO^- + R_1R_2NH^+$$

$$R_1R_2NCOO^- + H_2O \Leftrightarrow R_1R_2NH + HCO_3^- \qquad (2.1)$$

For many decades, chemical absorption has been extensively commercialized not only power plants, but also the retrofit existing power plants. Nevertheless, this technology has been found, some important problems while using a MEA aqueous solution such as (1) amine degradation in the presence of oxygen in flue gases, which increased makeup solvent; (2) high energy consumption for regeneration process; (3) low CO_2 capacity; (4) high corrosion rate; (5) large equipment size [25]. Blending with other solvent is an alternative choice to overcome problems such as Methyldiethanolamine (MDEA). An appropriate ratio between MEA and MDEA solvent is required lower energy for CO_2 regeneration significantly [26].

2.2.2 CO_2 Adsorption

A process that involves the surface accumulation of gas or liquid known as an adsorbent, forming a thin film of an adsorbate, gas or liquid for releasing adsorbed rich-CO_2 on the surface based on the difference capacity between the adsorption and desorption processes by using the pressure or the temperature.

- Temperature swing adsorption (TSA)

Temperature swing adsorptions (TSA) are one of the potential techniques to be used for CO_2 separation processes. The solid sorbent adsorption occurs at a low temperature level of CO_2 mixture gas stream and terminates when an equilibrium condition reaches. Consequently, CO_2 concentration will break through at the outlet of the bed of solid sorbent. After an equilibrium condition, the bed is being heated via hot gas (N_2/O_2) stream at a high temperature level to release CO_2 from solid particles, called regeneration. The acquired heat for CO_2 desorption process can be provided by direct and indirect ways. Direct desorption usually purged a hot gas stream contacting through the solid sorbent bed while using heat exchanger tubes is the indirect heating. After the regeneration step, the bed of solid particles then cools down at a low temperature level again to prepare next adsorption cycle as shown in Fig.2.5. The green and blue colors implies CO_2 and N_2 gas, respectively and T_d implies the desorption temperature.

Two main forms of heat concerned in term of energy consumption of a TSA process for post-combustion CO_2 capture are the latent and sensible heat. The definition of latent heat is the energy being absorbed or given off by a substance while it is changing its physical state during a constant temperature process. And the energy that affects a change of adsorbent material from the adsorption to desorption temperature in an object by a body or thermodynamics is called sensible heat. Measuring the ratio of partial pressures of CO_2 in the adsorption and desorption cycle can be obtained the minimum temperature difference between adsorption and desorption. There are some disadvantages for TSA operating processes. That is, CO_2 desorption process needed a large amount of energy and required a large solid inventory due to the unstable process for rapid cycle (cold and hot processes).

- Pressure swing adsorption (PSA) and vacuum swing adsorption (VSA)

All of the above, there are PSA, VSA and TSA generally operated for industrial applications. These methods are suitable for solid sorbent adsorption-regeneration cycle. Other regeneration approaches, i.e., Electric swing adsorption (ESA), Pressure and temperature hybrid process (PTSA), still need for further study.

A large-scale of PSA technology for CO_2 adsorption-desorption cycle and H_2 purification were discovered in the 1970s with the PSA multilayer processes from 4 bed [27]. Moreover, the additional beds typically 7 to 10 beds have been included for improving the separation efficiency [28]. PSA is a regeneration process which a porous solid adsorbent is reduced to the partial pressure rapidly to release the adsorbed component on the surfaces. After removing the adsorbed components, a porous solid adsorbent is available for adsorption again. The external heat source is not required for desorption. The cycle steps of PSA adsorption-desorption consist of 4 basic steps having 4 beds as mentioned: pressurization, adsorption, depressurization and regeneration. The four basic steps of pressure swing adsorption-desorption cycle is shown in Fig 2.6. First, a mixture gas stream under high pressure is co-current fed into the bottom of the first vessel containing adsorbent materials commonly alumina, activated carbon, silica gel or molecular sieves. The impurities are adsorbed on the adsorbent internal surface, then released product or clean gas at the top of the vessel.

By removing impurities, the remaining product gas goes back into the gas phase and the adsorption vessel is depressurized. After depressurization step, a small amount of purified product gas is then purged. The exhausted stream in the counter-current blow down in order to complete the regeneration process. Finally, a mixture of product gas from the depressurization step is fed into the adsorption vessel to repressurize [29]. In the conventional PSA process, these steps are repeated every 2-20 minutes. Mostly, there are adsorption and regeneration vessels, but each step could be used in the same vessel due to the cycle is operated a batch process. At the same time, vacuum swing adsorption or VSA is a derivative of PSA technique. The cycle steps of VSA adsorption-desorption is similar with PSA. However, the vacuum condition is used in the depressurization step in order to recover CO_2 from flue gas. The adsorption mechanism is attended higher than an atmospheric pressure to overpower the pressure drop in the column. The CO_2 adsorption consists of physical and chemical adsorption processes.

- *Physical adsorption*

In order to overcome some limitations of amine-based absorption processes, such as, low gas-liquid contact area, corrosion and low CO_2 loading, the alternative option for capturing CO_2 may be physical solid adsorption. Comparing adsorption via diffusion of CO_2 from flue gas in mesoporous adsorbents, it was found that it is three orders of magnitude higher than aqueous amine-based absorption [30]. Alumina, activated carbon, various zeolites and metallic oxides are commercially porous adsorbent types which utilized for CO_2 capture [31].

The conceptual characteristics of solid adsorbents are preferred low cost, not reacting with moisture and high thermal stability. The mechanism of CO_2 capture for these porous materials such as activated carbon and zeolite adsorbents can be described as

$$CO_2 + surface \Leftrightarrow (CO_2)\cdot(surface) \tag{2.2}$$

where the interaction potentials between molecule of CO_2 and adsorbent surface is Van der Waals force and electrostatic including polarization, dipole, and quadrupole interactions [32]. Adsorption and regeneration techniques of adsorbents widely use the reduction of pressure or pressure swing adsorption (PSA) and the heating or temperature swing adsorption (TSA) processes, which is discussed in the regeneration section later.

- *Chemical adsorption*

To improve the efficiency of solid sorbents, the concept for capturing CO_2 by integrating alkali-metal or alkali-earth dispersion on solid sites is invented. Since CO_2 is acid, so the basic site on the surface of the porous materials are capable to capture CO_2.

This promising modification process can increase CO_2 selectivity and CO_2 adsorption capacity. Furthermore, the regeneration temperature is not relatively high (below 200 °C). So, the prominent alkali-metal base type such as sodium (Na), potassium (K), magnesium (Mg) and calcium (Ca) are often used as the solid sorbent for CO_2 capture [2-4, 7, 33, 34].

The dry regenerable solid sorbent for CO_2 capture mechanism is described in the following equations. M represents alkali-metal, Na, K, Mg, Ca, respectively. After desulfurization, the flue gas stream, including CO_2 and water vapor, enters into the adsorption reactor which contains solid sorbent inside. The adsorption temperature in the presence of water is in the range of 60 – 80 °C, as shown in Eq. 2.3. The alkali-metal carbonate is transformed to bicarbonate form.

$$M(Na,K)_2CO_3 + CO_2 + H_2O \Leftrightarrow 2M(Na,K)HCO_3 \tag{2.3}$$

$$M(Mg,Ca)O + CO_2 \Leftrightarrow M(Mg,Ca)CO_3 \tag{2.4}$$

The bicarbonate solid sorbents are transferred into the second reactor to release CO_2 by using temperature swing. The heat of the bicarbonates for regeneration are 100 - 200 °C. While regenerating, moisture is evaporated, the remaining in solid sorbent is pure CO_2. Then the solid sorbent is then cooled and shifted to adsorption reactor again.

Aspect concerning of this process is supporting materials due to after the first cycle, CO_2 capture capacity will be decreased. The characteristics of supporting materials are fast adsorption/desorption kinetics, high surface area, high attrition resistance for long term stability. Various types of support materials have been studied such as activated carbon, Al_2O_3, silica gel, TiO_2, MgO and Zeolite [2, 3]. The results indicated that Al_2O_3 performed excellent total CO_2 capture capacity and possibly regenerate at low temperature.

2.2.3 Cryogenics separation

The cryogenics separation is suggested as a post-combustion process towards the gas-liquid separation. The condition of this process has been done in very low temperature to change gas phase to liquid phase. When gas mixing from the flue gas combustion at high temperature enters into the refrigerating condenser, the contaminants, including water vapor, will firstly condense from cooled gas mixed and then removed from stream.

After removing water from the flue gas stream at an atmospheric pressure, CO_2 in gas phase is compressed at 5 to 7 bars and -107 °C, as a liquid phase. At the same time, the condensed contaminates are removed [35]. Liquid CO_2 is condensed and separated through a distillation column for a facile transportation. The schematic diagram of cryogenic is shown in Fig 2.3. This process can provide purified liquid CO_2 and there is none of chemical adsorbents or adsorbates involved. Nonetheless, high energy usage due to gas compression and a high cost of refrigerant are still considered. A packed bed operation is the novel cryogenic for CO_2 capture process [36].

2.2.4 Membrane absorption

A high selective semi-permeable barriers have been studied for post-combustion CO_2 capture. Commercially, membrane absorption processes have been used for natural gas processing at high CO_2 concentration and high pressure and enhanced oil recovery (EOR). The desired properties for the membrane materials performance which separated the molecules in the gas mixture specifically are uniform micropores, higher surface areas, and exceptional thermal and chemical stability. For decades, there are numerous membrane types for gas separation process. Membrane types using for separation could possibly be either organic including polymeric or inorganic including carbon, zeolite, metal. Simplicity, compact design and uncomplicated operation are the distinctive features of this process, as well as no chemical added. As a result, costs of regeneration and phase changes association are eliminated. A schematic diagram of membrane gas absorption is displayed in Fig 2.4. The CO_2 containing gas stream contacts the pores at the bottom, then the diffusion and absorption by solvent occurred. There are only CO_2 being adsorbed because of the selectivity of solvent. For separating absorbed CO_2 gas from membrane, a regeneration solvent in liquid phase is moving down to remove CO_2. This membrane type is suitable for a low partial pressure of CO_2 due to the small driving force of gas separation. However, membrane separation has not been contributed on a large-scale process and still challenged to the composition and flue gas temperature relatively.

2.3 CO_2 Regeneration system

Various utility industries separate CO_2 from CO_2 capture processes for transportation and storage. Swing adsorption has become well-known commercial techniques, using different adsorption capacity between the individual components in a flue gas mixture from combustion. The regeneration approaches consist of temperature, pressure and vacuum [37].

In summary, the post-combustion CO_2 capture system and the CO_2 separation technologies for the existing fossil fuel power plants, with chemical adsorption using the dry alkali-based regenerable solid sorbent, has been further studied in this research. Heat is the concerning factor since the adsorption and regeneration mechanisms are exothermic and endothermic, respectively. Accordingly, fluidization technique has been used to prevent thermal problems occurred due to the advantage of a good heat transfer.

2.4 Fluidization

Fluidization is a process which solid particles from a static solid-like state are transformed into a fluid-like state. This process occurs when gas or liquid are passed upward through a bed of solid particles. At a low velocity, fluid is percolated by a distributor through the void at the bottom of the bed without moving. This behavior is called fixed bed. In order to move up solid particles, the velocity between the solid drag forces has to increase for counteracting with the gravitational forces. An expanded bed volume as solid particles starts to move apart from each other at the critical point, which the solid drag forces in the upward direction are equal to the gravitational forces in the downward direction. The pressure drops at any region of the bed are adequate to the weight of fluid and solid particles. Then, solid particles start to fluidize. With an increase fluid velocity, the flow behaviors of the fluidized bed will change and become more violent. When fluid velocity increases sufficiently, the terminal velocity of the bed is exceeded and the solid particles are carried through the bed when the fluid velocity higher than the terminal velocity.

Several industrial applications have been using fluidization technology for decades. Due to high heat and mass transfer between gas and solid particles, rapid solid mixing, short contact time, continuous operation and capable of large-scale operation. These fluidized bed characteristics become the advantages for some restricted technologies compared to other applications. Table 2.1 shows the industrial applications of fluidized beds

2.5 Fluidization flow regimes

When increasing a superficial fluid velocity upward through a bed of solid particles, the bed behavior changes in various ways. In fluidization, the transition of flow regimes depends on a superficial fluid velocity. At an initial condition, a batch bed of solid particles stays at the bottom. When a bed approaches with a very low velocity, the bed is not moving. This flow type is in a fixed bed operation. When the gas velocity keeps increasing, solid particles are start moving in a column. Further increasing the fluid velocity, the solid are separated from each other and shifted from one stage regime to another regime. The flow patterns or regimes of gas-solid fluidized bed have been classified with increasing superficial fluid velocity including fixed bed, bubbling fluidization, turbulent fluidization, fast fluidization and pneumatic transport as shown in Fig. 2.7. In the batch process as well as fixed bed and bubbling fluidization, the additional solid particles for make-up are unnecessary, since there are solid particles remaining in the column. While three other regimes or the continuous operation is essential, because of the entrainment of solid particles [38], this behavior are used to transfer solid particles with a high gas velocity from one place to another place.

2.5.1 Fixed bed

A fixed or packed bed occurs when solid particles settled in stationary phase owing to a gravitational force at the bottom of a column, when column is introducing with a low gas velocity. The fluid flows through without the bed moving. In case of introducing a higher velocity, the solid particle drag force or frictional force raises as well as the pressure drop across the bed. The upward solid drag force counteracts with the gravitational force which is in the opposite direction. The frictional pressure drop per unit height of the fixed bed $(\Delta P / L)$ equation is expressed by Ergun [39], containing of the uniform particle size (d_p). For a fixed bed, the frictional pressure drop of the bed is approximately proportional to a gas velocity, as shown in Eq.(2.5). The Ergun equation is described as follow:

$$\frac{\Delta P}{L} = 150\frac{(1-\varepsilon_g)^2}{\varepsilon_g^3}\frac{\mu_g u_g}{(\phi_S d_p)^2} + 1.75\frac{(1-\varepsilon_g)}{\varepsilon_g^3}\frac{\rho_g u_g^2}{\phi_S d_p}$$

(2.5)

where ε_g is the volume fraction of gas, ϕ_s is the sphericity, μ_g is the gas viscosity and ρ_g is the gas density. The superficial gas velocity, u_g , is define as the volumetric flow rate of gas per unit cross-sectional area of total riser.

2.5.2 Bubbling fluidization

It can be seen from Fig. 2.7, as the gas velocity increased further through the critical value for a fixed or packed bed, solid particles in stationary phase initiate to fluidize to bubbling bed. The lowest gas velocity which all solid particles are suspended from a fixed bed through fluidization is defined as the minimum fluidization velocity (u_{mf}). As depicted in Fig 2.8, the pressure drop at of the bed equals to the weight of fluid and solid particles of the bed at the minimum fluidization velocity. It has been shown that, in addition to increase the gas velocity greater than the minimum fluidization velocity, the expanded bed and small gas bubbles are readily visible. And the pressure drop has remained constant even though the gas velocity rises. This is due to the well aerated and can be changed easily without significant resistance of the dense gas-solid phase. The fluid drag force of the upward flow (F_{Drag}) can be calculated by the pressure drop across the bed equals to the weight of bed

$$F_{Drag} = A \cdot \Delta P = A \cdot L(1-\varepsilon_g)(\rho_s - \rho_g) \cdot g \tag{2.6}$$

where A is bed cross-section area, L is bed height, ρ_s is the solid particle density, ρ_g is the gas density and g is the gravity force.

Numerous studies have been explored for minimum fluidization velocity. Wen and Yu [40] were the first to propose that over the wide range of $\mathrm{Re}_{mf} = 0.001$ to 4000, the empirical constant, C_1 and C_2, are nearly constant for different particles. One of these empirical equations, the obtained values C_1 and C_2 in the experiments from Grace [41] are 27.2 and 0.0408, respectively. After solving Eq (2.7) and (2.8), the superficial velocity at minimum fluidization velocity, u_{mf}, is obtained.

$$Ar = 150\frac{(1-\varepsilon_{mf})}{\varepsilon_{mf}^3 \phi_S^2}\left(\frac{\rho_g d_p u_{mf}}{\mu_g}\right) + 1.75\frac{(1-\varepsilon_{mf})}{\varepsilon_{mf}^3 \phi_S}\left(\frac{\rho_g d_p u_{mf}}{\mu_g}\right)^2 \tag{2.7}$$

$$\mathrm{Re}_{mf} = \left(\frac{\rho_g d_p u_{mf}}{\mu_g}\right) = \left(C_1^2 + C_2 Ar\right)^{0.5} - C_1 \tag{2.8}$$

where Ar is the Archimedes number ($Ar = \frac{\rho_g(\rho_s - \rho_g)g d_p^3}{\mu_g^2}$) and ε_{mf} is the gas volume fraction at minimum fluidization condition.

Geldart and Abrahmsen [42] observed the minimum bubbling velocity by measuring different particle sizes and densities to characterize the particle behavior. It was found that when gas velocities are higher than minimum fluidization velocity, the bed expansion of Geldart group A particles essentially occurs before the bubble appear when solid particles are fluidized. The correlation values of minimum bubbling velocity with Geldart group A particles can be described as:

$$u_{mb} = 2.07\exp(0.716F)d_p\left[\frac{\rho_g^{0.06}}{\mu^{0.347}}\right] \tag{2.9}$$

where F is the weight fraction of powder less than 45, d_p is mean solid particle diameter, μ is the gas viscosity. The existence of bubbling fluidized bed occurs when the gas velocity slightly beyond the minimum fluidization velocity. And the fluidizing velocity when the observed bubbles first appear is also known as the minimum bubbling velocity (u_{mb}). In gas-solid fluidized bed system, the appearance of a bubble comes when the gas velocity slightly higher than minimum fluidization velocity. The fluidization index is the ratio of minimum bubbling velocity to minimum fluidization velocity, u_{mb}/u_{mf}, gives a measure of the degree to which the bed can be expanded uniformly. Moreover, the fluidization index was depending on the weight fraction of powder less than 45 μm. Due to the high interparticle forces of the small particles, a bubble-free fluidization exists in Geldart group A. For Geldart's classification, group B particles (40 to 500 μm) and group D particles (higher than 600 μm), the onset bubbling fluidization regime is appeared as soon as the gas velocity slightly increases faster than the minimum fluidization velocity. Therefore, u_{mb} $/u_{mf} \cong$ 1. While Geldart group C particles (20 to 30 μm) are inappropriate for fluidization due to the solid particles are cohesive and it is very fine powders [43].

2.5.3 Slugging fluidization

As increasing the superficial gas velocity further, the gas bubble sizes grow and cover to the cross-section bed entirely. This is called slugging phenomena. The solid particles above bubble are pushed in the upward direction and then rained down breaking the slug. Slugging fluidization generally occurs in a tall and narrow in the bed of high aspect ratio (>>1), which is defined as a ratio between the height of the bed to column diameter. However, the shallow bed (e.g. aspect ratio < 1) and the very large column diameter of fine particles (e.g. d_p < 60 μm) conditions are not included in slugging since the bubbles are unable to grow and expand bubble sizes in covering the column diameter.

The minimum slugging velocity, u_{ms} can be performed by Stewart and Davidson [44].

$$u_{ms} = u_{mf} + 0.07(gD)^{1/2} \tag{2.10}$$

2.5.4 Turbulent fluidization

The definition of turbulent regime is considered as the transition regime from bubbling fluidization and fast fluidization. When the superficial gas velocity (u_g) passed through a bubbling bed above the minimum bubbling velocity (u_{mb}), the bed of solid particles is initially moving. If the gas velocity is increased further, the terminal velocity of solid is exceeded. Then, the bubbling bed expansion changes the pattern into a new regime called a turbulent fluidization. In the turbulent regime, due to the rapid coalescence and break-up reach to the dynamic balance, the bubble phase disappears, as well as, the upper surface of the bed. The bed expansion is increased as a result of the predominance of bubble break-up condition [45]. The gas velocity carried the amount of solid particles out of the expanded bed into the freeboard region. Thus, the turbulent fluidization regime can divide into two main regions, consisting of dense phase in the lower region and dilute dispersed phase in the upper region. [46]

To distinguish the difference between bubbling fluidization and fast fluidization, the two definition of velocities are commonly used. The first is a transition velocity, u_c, defined as the superficial gas velocity when the bubbles or slugs in the bed of particles reach the maximum diameter and the largest standard deviation of the pressure fluctuation [45]. The second velocity is u_k, a critical velocity on entry into the turbulent regime. Continuing increase the gas velocity, the large bubbles in the bed start to erupt into smaller bubbles at which the standard deviation of the pressure fluctuation become less and finally reaches the steady state. However, there is no well-established correlation for calculating u_c and u_k due to the effect of sensitivity of measuring methods for both u_c and u_k velocities, including the column diameter, temperature, solid particle properties and so on. Several researchers investigated the correlation parameter for calculating u_c and u_k in this fluidization regime. The correlations of FCC particles for a transition velocity u_c, is shown below [47], $\mathrm{Re}_c = \dfrac{\rho_g d_p u_c}{\mu_g} = 0.565 Ar^{0.461}$ (2.11)

For a critical velocity, u_k, is predicted by Tsukada et al. [48] based on the differential pressure fluctuation.

$$\mathrm{Re}_k = \frac{\rho_g d_p u_k}{\mu_g} = 1.310 Ar^{0.450} \quad (2.12)$$

When further increased the gas velocity higher than a critical velocity (u_k), the amount of solid particles are carried out at the top of the column. This transition from the turbulent to fast fluidization is also known as the transport velocity, u_{tr}. The correlation between Reynolds number for the transport velocity and Archimedes number has been estimated by Tsukada et al. [49].

$$\mathrm{Re}_{tr} = \frac{\rho_g d_p u_{tr}}{\mu_g} = 1.806 Ar^{0.458} \quad (2.13)$$

2.5.5 Fast fluidization

The definition of fast fluidization regime is determined as the transition between turbulent and pneumatic transport fluidizations regimes. The characteristic of turbulent regime was initially investigated by Yerushalmi and Cankurt [45], Yerushalmi et al. [50] and Avidan and Yerushalmi [51]. It composed of solid volume fraction, somewhere between dense and dilute phases, the relatively high density and pressure fluctuation of dense-phase beds were disappearing, clusters occurred, high solid back mixing. Slip velocity of particles is one order of magnitude larger than terminal velocity (u_t). For both turbulent and fast fluidization regimes are categorized into high velocity fluidization regimes because of containing two main regions, as dense and dilute zones [46]. Above the dense zone, the dilute or freeboard zone where the solid holdup profile decreased exponentially with increasing ε_s equal to 0.02 to 0.05. With this behavior, the axial distribution of average voidage can provide into S-shaped profile in the riser [52]. These different flow behaviors can imply that the solid particles near the annular region flow downward while solid volume fraction near the central core is flowing upward. This is noted as the core-annulus flow structure [53].

Most previous studies have also indicated that there is no identified for the transition definition of the fast fluidization regime to other fluidization gas-solid regime. However, the minimum velocity which is no solid particle reached to fast fluidization regime is called the transport velocity, u_{tr}. This transport velocity expressed the transition from the turbulent to fast fluidization [54, 55]. When superficial gas velocity (u_g) exceeds the transport velocity, u_{tr}, it is a sudden change of pressure drop [45]. If the bed of solid particles velocity beyond the transport velocity, u_{tr}, as a result, the entrainment of solid particles occur unless there is a rapidly solid make-up. After a certain amount of time, the column will be empty.

2.5.6 Pneumatic transportation

As increasing the gas velocity through fast fluidization regime, the transition from fast fluidization to pneumatic transport is occurring. There is no solid accumulation at the bottom of the riser which is relatively a high density and large pressure fluctuation [47, 56]. This critical value is also known as the minimum pneumatic velocity (u_{mp}). In this regime, all the solid particles are well-dispersed in the gas phase and carried out the column. In order to measure the transition velocity, the superficial gas velocity is decreased until the Geldart group A particles choking is occurred at a constant solid circulation rate [56]. However, minimum pneumatic velocity is difficult to detect in the experiments. A correlation equation to predict u_{mp} may be written explicitly as [57]:

$$u_{mp} = 10.1\left(gd_p\right)^{0.347}\left(\frac{G_s}{\rho_g}\right)^{0.310}\left(\frac{d_p}{D}\right)^{-0.139}\left(Ar\right)^{-0.021} \tag{2.14}$$

where Gs is the circulation rate or mass flux of the solid particles and D is the column diameter.

2.6 Circulating fluidized bed

2.6.1 Concepts

Over the past decades, a gas-solid system in industrial applications has been successful in maintaining solid stabilities and continuing of solid circulation rate such as chemical process industry, mineral processing, energy-related processes and so on. The quantity of solid particles becomes a great interest in the large-scale operations at a high superficial gas velocity since the loss of solid particles can affect the reactor performance directly. Therefore, circulating fluidized bed (CFB) has come to prominence, since 'circulating' is defined as the particle separation and particle return system are integrated and it is crucial component of the overall reactor configuration 'fluidized bed' is referred to the solid particles being supported by fluid [58].

To maintain solid holdup in this circulating fluidized bed reactor type, the solid particle has to feed continuously. The captured solid particles are leaving at the top and returning at the bottom of the column by a recirculation system [59]. The most common circulating fluidized bed systems are generally operated between low velocity fluidized bed to fast fluidization regime.

A typical configuration for a CFB reactor is illustrated in Fig. 2.9 , consisted of a tall vessel or riser, cyclone for gas-solid separation, a downcomer or standpipe and a return system. Firstly, solid particles are introduced into the riser column near the bottom and carried out to the top after contacted with a sufficient flow of a gas. The entrained solid particles in the upward are separated from a gas stream by a cyclone using centrifugal force exerted on solid particles in the radial direction. From the top of the cyclone, the solid particles fall to the bottom in the downer or standpipe. The solid particles flow from the lower pressure region near the outlet to a higher pressure region which is at the bottom. Finally, solid particles are returned into the riser.

2.6.2 Circulating turbulent fluidized bed and further studies

Recently, Zhu and Zhu [14, 17] promoted a novel circulating-turbulent fluidized bed (C-TFB) which was investigated a new regime combining the advantages of circulating fluidized bed riser and turbulent fluidization regime. The flow behavior in the C-TFB has its inherent characteristics, different from those in CFB, turbulent fluidization (TFB) and high density CFB (HDCFB) reactors. Because the C-TFB can operate in a low superficial gas velocities and high solids circulating rates, it is then resulting in a highly dense suspension and uniform axial flow.

Zhu and Zhu [14] studied a hydrodynamics of circulating-turbulent fluidized bed (C-TFB). The system consists of six sections: A C-TFB column, a quick discharging section at the top, a downer, a solid circulation rate measurement, a loop recycling and a solid return pipe. The axial differential pressure profiles in C-TFB are nearly uniform. The differential pressures profiles increased with increasing solid mass flux, G_s and decreasing superficial gas velocities, U_g. In addition, the distribution profile of solid in the C-TFB was found to be uniform and dense gas-solid suspension has been achieved along the whole column. The standard deviations for the radial solid velocity profile showed the fluctuation in the middle of the riser. It is indicated that there is a strong interaction between gas-solid at the corresponding radial position. Such a phenomenon shows the peak of standard deviation at the middle radial position for a high density circulating fluidized bed (HDCFB).

At high solid flux (300 $kg/m^2 s$), Pärssinen et al. [15] observed the axial and radial solid distribution in a high-flux circulating fluidized bed (HFCFB) riser (height 10 m, i.d. 76 mm). As increasing the superficial gas velocity, the onset of dense and dilute phase can be observed at lower axial levels. However, when the solid flow increases, there is no significant effect on the measured properties of the development at a constant gas velocity in the radial solid distribution. In this experiment, the particle acceleration (and consequently the development of the flow) remained constant in the center.

Bastos et al. [16] investigated a two-phase three-dimensional model fluid flow at a high flux compared with the experiment of Pärssinen and Zhu [15]. They divided solid velocity into three cases: case 1 there was no solid viscosity with 15 sec simulation time, case 2 it was using the Newtonian coefficient with 15 sec simulation time and case 3 was the same as case 2 but increasing the simulation time to 37 seconds. The solid velocity profiles in the radial distribution of the HFCFB are split into three zones with a dense-phase flow at the bottom section, a developmental flow in the intermediate and dilute zone at the top. The simulation result in case 3 was consistent with the experiment, but overpredicted at the bottom zone. The core-annular in the wall region showed at a low particle velocity until the middle zone and disappeared when reaching a dilute zone at the top.

Issangya et al. [60] and Grace [61] claimed this CTFB phenomenon as a special characteristic for HDCFB operation under relatively high superficial gas velocity, but it was clearly shown in C-TFB as well. The solid backmixing phenomenon result, which was obvious in both turbulent fluidized bed and circulating fluidized bed, was greatly reduced for C-TFB as reflected by the fact that the net mean time of the flow was always positive at all radial positions. There are comparisons between the radial solids distribution between the C-TFB, turbulent fluidized bed (TFB) and conventional circulating fluidized bed (CFB), the result showed that the C-TFB became much more uniform than that in the CFB, and closer to that of a conventional TFB. Although there was still a radial gradient in solids concentration distribution in C-TFB, the variation was continuous, rather than exhibiting a sharply demarcated core-annulus flow structure observed in the CFB. Even in high density and/or high flux CFB risers, it still exists a definite dilute core region surrounded by a dense region adjacent to the riser wall.

2.7 Literature reviews

Zhao et al., 2009 [3] studied CO_2 adsorption-regeneration cyclic operation and physical characteristics on different supports of K_2CO_3-based sorbents by conventional impregnation method using thermogravimetric analysis (TGA) and a bubbling bed. Different supports included activated charcoal, coal captive carbon, silica gel and activated alumina. It can be concluded that the K_2CO_3-based on activated alumina exhibited mesoporous pore structure and gave the excellent CO_2 capture capacity with the total conversion of 95.2% and 87.6% in TG test and a bubbling bed, respectively. The XRD pattern results showed that the carbonation reactivity of $K_2CO_3 \cdot 1.5H_2O$ phase was enhanced on activated alumina. In addition, this phase reacts with CO_2 quickly than K_2CO_3 phase.

Durán-Guevara, M. B., et al. (2015) [62] studied CO_2 capture capacity of mesostructure γ-Al_2O_3 powder as supported by preparing several methods on K_2CO_3-based. The results explored that the poly-ethylene glycolsorbitanmonolaurate (Tween) gave the excellent physical properties. And the CO_2 sorption capacity increased proportionately with the loading of K_2CO_3-based. Beside the loading amount of K_2CO_3-based, temperature and moisture content, the textural properties of the support also affected the CO_2 capture capacity.

Luo, H. et al. (2015) [63] studied kinetics analysis and structural changes of K_2CO_3 under water vapor conditions using thermogravimetric analysis (TGA). Potassium bicarbonate ($KHCO_3$) was decomposed from ambient temperature to 473 K under several partial pressures of CO_2. The reaction time was held 0-120 min for all experiments. The obtained CO_2 capture capacity from experimental results increased when CO_2 flow rate was increased under moisture conditions. When increasing CO_2 concentration, the presence of $K_2CO_3 \cdot 1.5H_2O$ was appeared first and then transform into $K_4H_2(CO_3)_3 \cdot 1.5H_2O$ phase in all samples for reacting with CO_2 gas to form $KHCO_3$. The morphology of K_2CO_3 solid particle after various reaction times, such as 5, 10 20 and 120 min initiated the small granules on the surface and disappeared the pores volume after 20 min.

Park et al. (2009) [12] investigated the effect of bed height on CO_2 capture capacity and regeneration on K_2CO_3-based sorbents in a bubbling fluidized-bed reactor with inner diameter 0.05 m and the height 0.8 m. The four different ratios of L/D (length/diameter) represented one, two, three and four ratio that the CO_2 capture capacity increasing when L/D ratio was decreased. The L/D ratio equal to one performed the highest total CO_2 capture capacity. In addition, the fractional CO_2 removal obtained from the L/D ratio of one also reported the excellent amount.

Lee, S. C et al. (2011) [7] investigated the new alumina was modified K_2CO_3/Al_2O_3 sorbent for enhancing the regeneration process at temperature below 200°C. The modified sorbent contained $KAl(CO_3)(OH)_2$ phase, which is not reactive at the beginning of the sorption process. Since this phase is stable and unable to eliminate at temperature below 350°C. The comparison between fresh sorbent and after adsorption-regeneration complete reaction 5 cycles showed the CO_2 capture capacity were 80-90% of the theoretical values which can calculate from the loading amount of K_2CO_3-based.

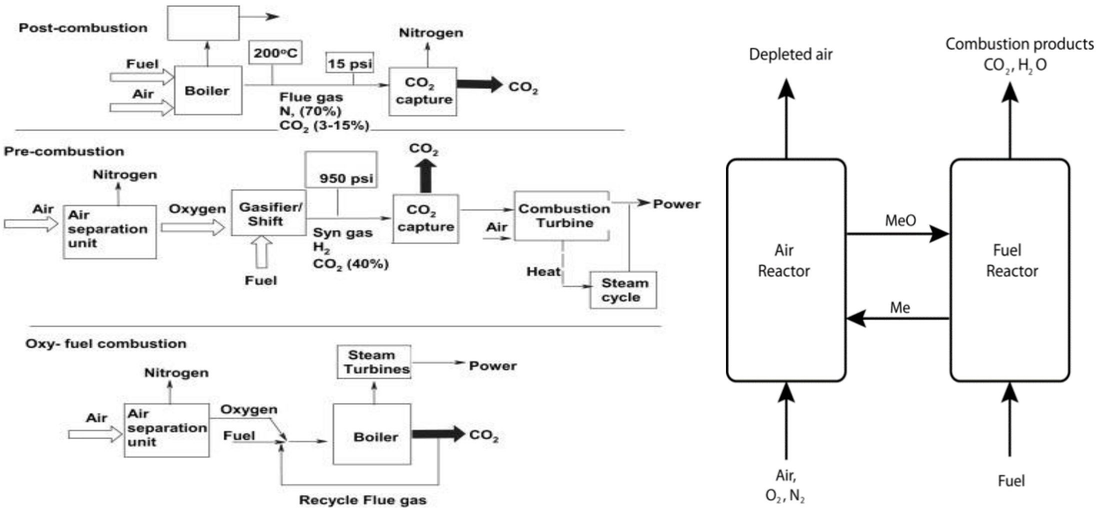

(a) (b)

Fig. 2.1 Schematic diagrams illustrating CO_2 capture systems: (a) pre-combustion capture, post-combustion capture and oxy-combustion (b) chemical looping combustion [37].

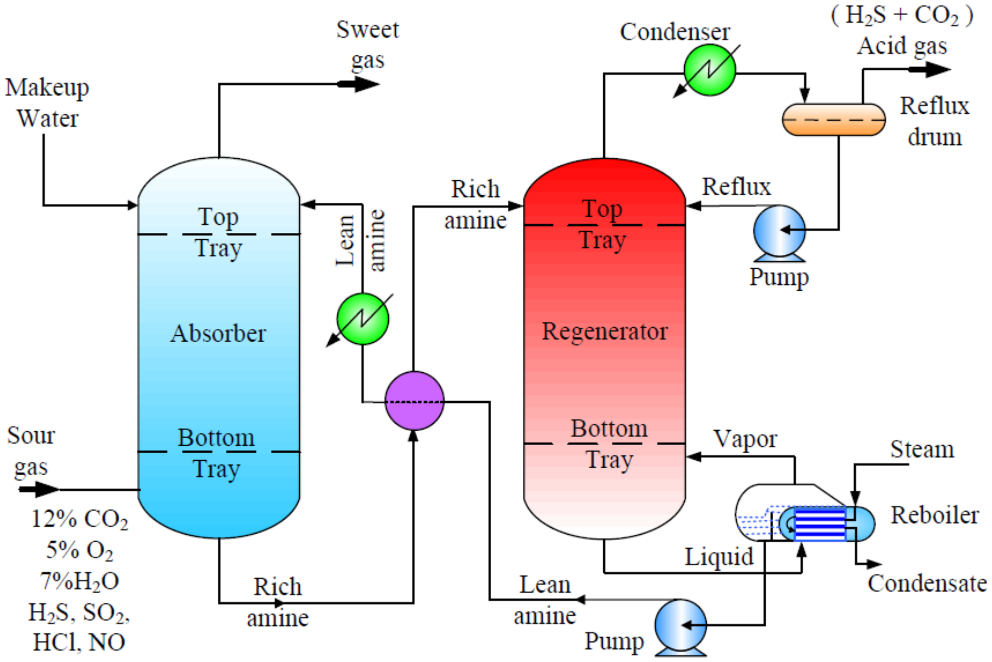

Fig. 2.2 illustrated amine-based absorption flow diagram processes [24]

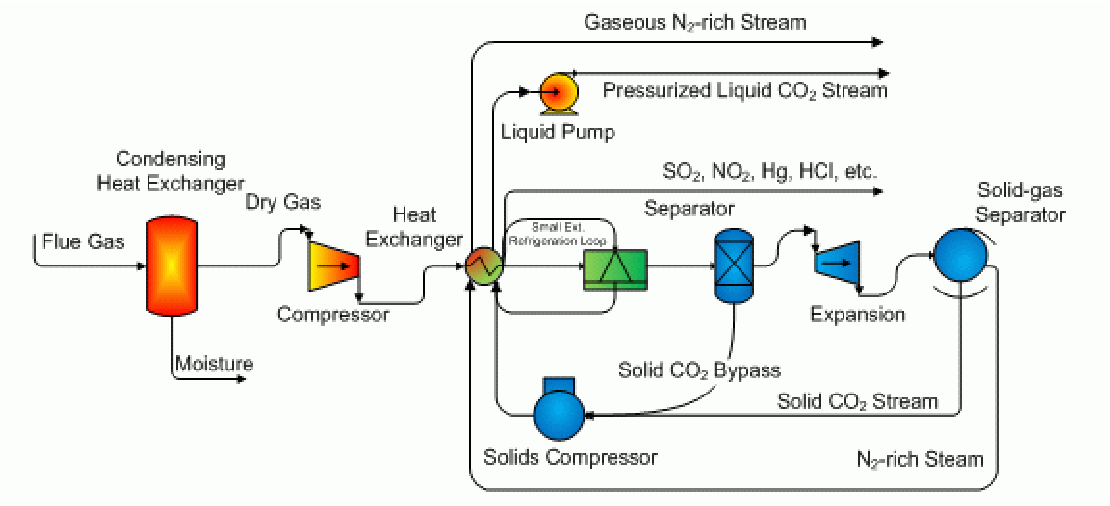

Fig. 2.3 Schematic diagram of cryogenic carbon capture process (CCC) [36].

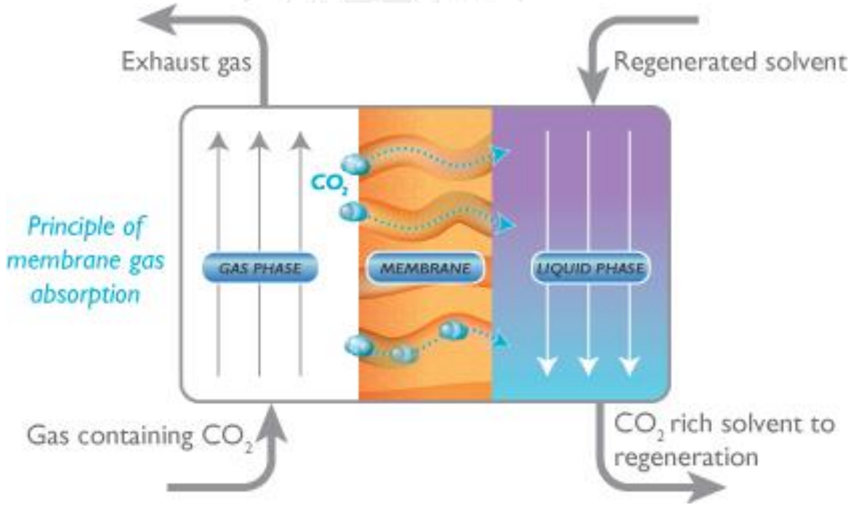

Fig. 2.4 Schematic diagram of membrane gas separation [64].

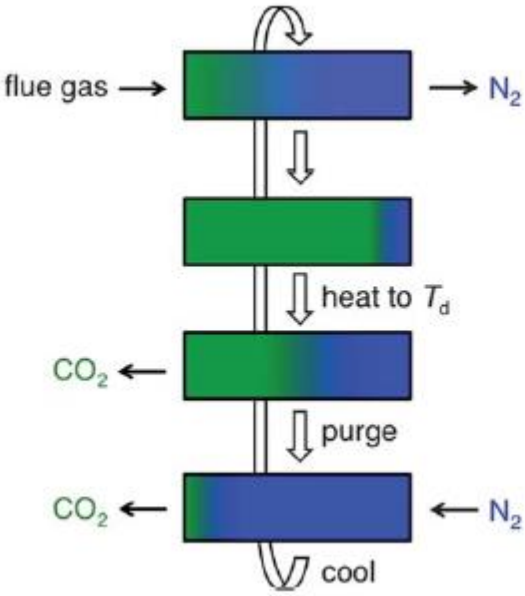

Fig. 2.5 Schematic diagram of idealized temperature swing adsorption-desorption cycle

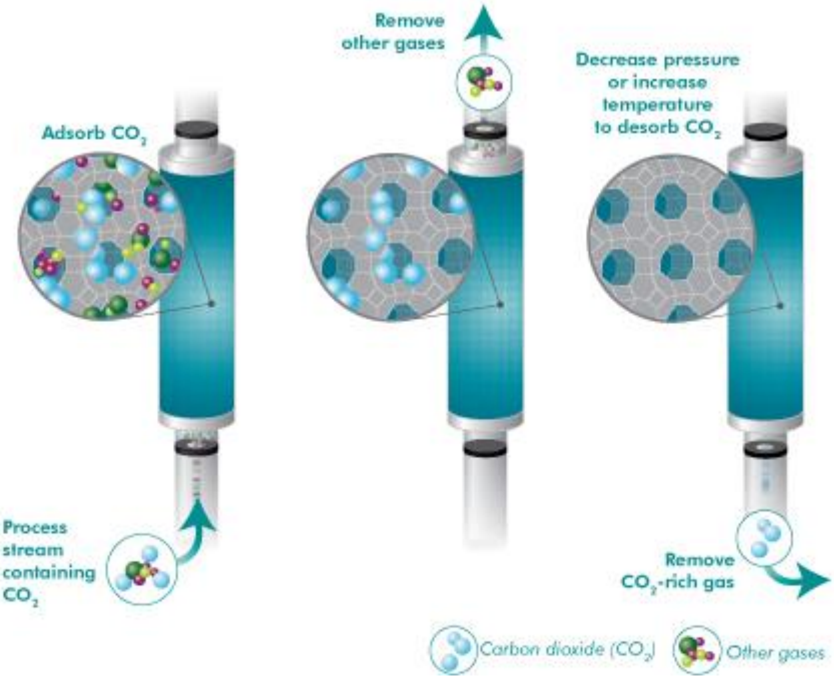

Fig. 2.6 Basic steps of pressure and vacuum swing adsorption-desorption cycle [29].

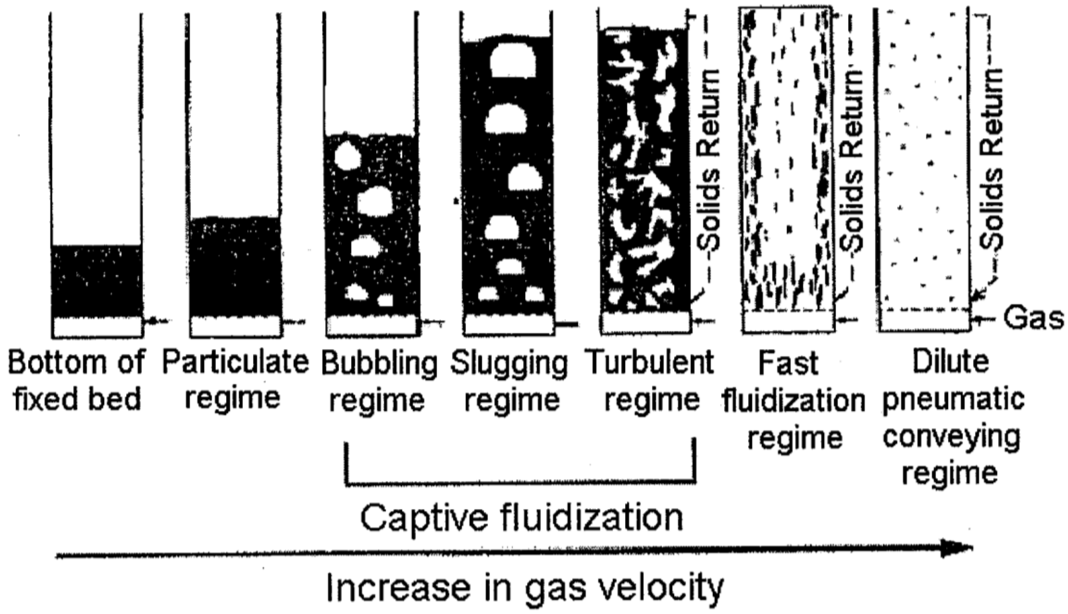

Fig. 2.7 The computed flow patterns or regimes in fluidized bed [65].

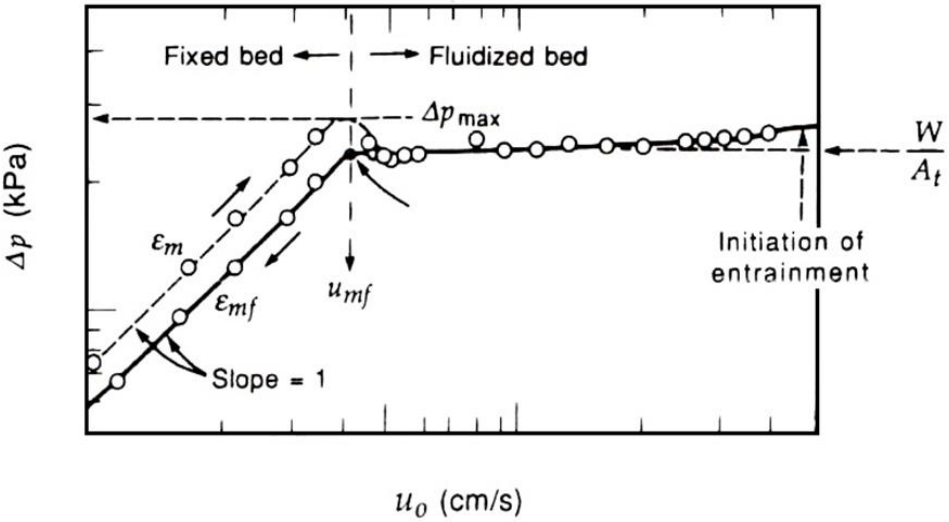

Fig. 2.8 Pressure drop versus the gas velocity for determining of minimum fluidization velocity [66].

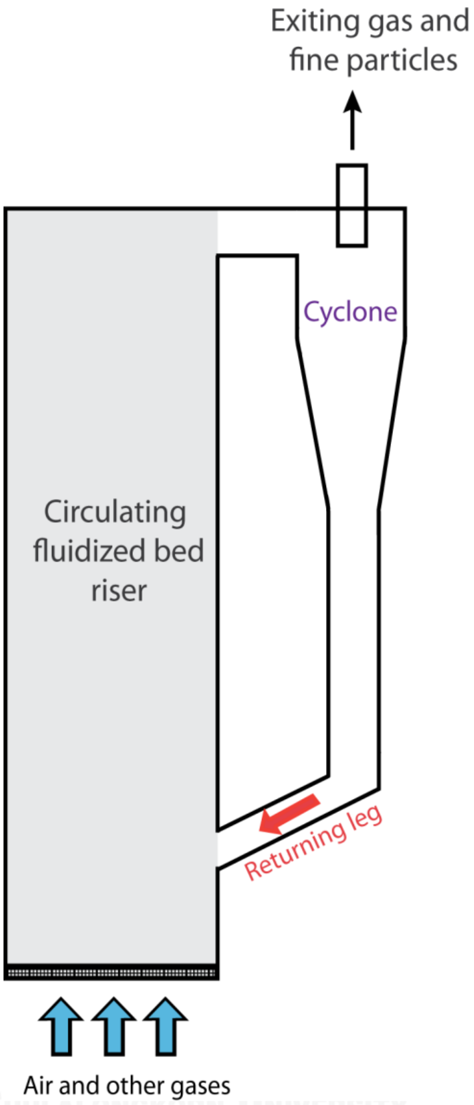

Fig. 2.9 A typical configuration for a CFB reactor.

Table 2.1 Industrial applications of CFB reactors [67]

Industrial types	Applications
Combustion	Coal combustion
	Solid waste incineration
	Reduction of iron ore
Chemical Synthesis	Calcination of alumina, phosphate rock
	Fisher-Tropsch synthesis
	Cement production
	Oxidative dehydrogenation of butane to butadiene
Petroleum Processing	Decomposition of sulfate, chloride and carbonate
	Butane oxidation to maleic anhydride
	Gasification of coal, biomass, etc.
Physical Operations	Simultaneous NO_x and SO_2 removal from off-gas
	Recovery/cleaning of flue gas
	Dehydration of boric acid

Chapter III

An investigation of CO_2 adsorption in circulating-turbulent fluidized bed flow regime

The conceptual characteristics of solid adsorbents are preferred due to low cost, not reacting with moisture and high thermal stability. In this chapter, the experiments were conducted to investigate the effect of flow pattern/regime characteristics inside the reactor, especially circulating-turbulent fluidized bed flow regime (C-TFB), on CO_2 adsorption and regeneration processes when using K_2CO_3/Al_2O_3 solid sorbent. The preparation of K_2CO_3/Al_2O_3 solid sorbent was described. The employed experimental materials, equipment, and procedure are illustrated in sections 3.1 to 3.3.

3.1 Materials

3.1.1 Chemicals

- Anhydrous potassium carbonate (K_2CO_3), AR grade M.W. = 138.21g mol^{-1} from Merck.
- Activated Alumina (γ-Al_2O_3), M.W. = 101.9 g mol^{-1} from Merck.

3.1.2 Gases

- Gas mixture of 12%v/v CO_2 with balanced N_2 from Thai-Japan Gas Co., Ltd.
- Ultra high purity (99.99%) N_2 from Praxair (Thailand) Co., Ltd.

3.2 Equipment and Apparatus set-up

3.2.1 Equipment

- Gas flow rate controller: K-1013 and K-1014 series glass rotameters Nitto instruments. The range of flow rate of K-1013 and K-1014 are 1-10 and 2-20 lpm, respectively. The accuracies of the gas flow rate controller of K-1013 and K-1014 are ±5 lpm.

- Temperature controller: TCL series temperature controller. Input is TC or RTD/ PT 108 types. The output control is relayed or SSR (solid state relay). The control type is ON/OFF control/PI. The operation conditions temperature and relative humidity are 0-200°C and 45-85%, respectively.
- Heater tape: Fiberglass heating tape. The maximum temperature is 250°C. The insulating resistance is more than 2 mΩ^3.
- Tube and valves.
- Glass fluidization reactor: The maximum operation conditions temperature is 500°C.
- Pressure sensor: An absolute gas pressure sensor which can measure applied external pressure relative to zero pressure reference sealed inside the sensor. The sensor's range is 150 – 1150 mbar (0.148 – 1.134 atm or 15 – 115 kPa).
- Temperature transducer: E52-CA1D temperature sensor E52. The temperature range is 0-500 °C. The element type is J (C). Conductor type is grounded type.
- Gas bag: Tedlar gas sampling bags. The maximum volume is 2 l. The maximum temperature is 100 °C.
- Vacuum pump

3.2.2 Apparatus set-up

The conducted experiments in a lab-scale circulating fluidized bed unit are illustrated in Fig. 3.1. The system includes four main parts: a gas-mixing system, a gas bubbler, a lab-scale circulating fluidized bed and temperature, pressure and CO_2 concentration measuring systems.

The circulating fluidized bed made of glass consists of four main parts: a riser, a downcomer, a cyclone and a solid storage for recirculating solid particles. In this study, the riser part has the total height of 0.70 m and inside diameter of 0.025 m. Eight pressure sensors were mounted at measurement ports along the height at every 0.10 m height from the bottom for measuring pressure along the column instantaneously. The connecting position of each pressure and temperature sensors were covered with 400 mesh sieve to prevent the blockage of small particles. The cyclone separator was connected at the exit of the riser part to separate solid particles from gas and transfer them down to the downcomer part. Then, solid particles returned to the riser through the transfer line. Make-up air was also added in perpendicular direction at the center of the transfer line to move and support solid particles in the downer part to the riser part. Three temperature sensors were installed and measured at bottom (0.05 m), middle (0.35 m) and top sections (0.70 m) of the riser part above the gas distributor. Then, the signals were sent to the temperature controller.

Gas velocity was supplied at the bottom through a 100 mesh glass distributor, resulting in the uniform flow, the superficial gas velocity was measured by a rotameter. The gas bubbler was used to produce water vapor and the vapor was mixed into the gas stream before entering the riser part. The liquid temperature in the gas bubbler was used to determine the water vapor content in the feed gas.

3.3 Experimental Procedure

The conventional impregnation solid sorbent, the flow pattern characterization, the CO_2 adsorption, the regeneration capacity, the regeneration kinetics, the CO_2 evaluation and solid sorbent characterization are explored in section 3.3.1 to 3.3.6, respectively.

3.3.1 K_2CO_3/Al_2O_3 solid sorbent preparation by impregnation method

Five (5.0) grams of activated-alumina (γ-Al_2O_3) as a support were added into an aqueous solution containing 5.0 grams of anhydrous potassium carbonate (K_2CO_3) and were dissolved in 25 ml of deionized water. The solid sorbent consists of 50% K_2CO_3 and

50% supporter for adsorption process. Then, the precursors were mixed in a shaker for 24 hours at room temperature to form a solution. After stirring, the solution was filtered and dried at 105°C in a vacuum oven. The dried solid sorbents were grinded and sieved to obtain the solid particle in the range between 75-150 µm. After collection of desired size, the sample were calcined for 4 hrs. at 300°C with 3°C/min ramping rate. The outline of approaches used for preparing K_2CO_3/Al_2O_3 solid sorbent process is shown in Fig. 3.2. To identify the amount of composing elements of alkaline metal on solid sorbent was observed by using an X-ray fluorescence analysis (XRF). The properties of prepared solid sorbent in this research are illustrated in Table 3.1.

3.3.2 The flow pattern characterization

Before the CO_2 capture and regeneration procedures, the gas-solid fluidization flow patterns/regimes had become an important feature to provide a high contacting level of gas-solid particle flow, also high heat and mass transfers. Fluidization flow patterns/regimes had distinguished hydrodynamics behavior due to the contacting between gas-solid, resulted in the different amount of CO_2 adsorption capacity. The flow patterns/regimes of fluidized bed/circulating fluidized bed included bubbling, slugging, turbulent, fast fluidization and homogeneous dilute transport regimes. Recently, a novel C-TFB is found as mentioned in the previous chapter. To further understanding of C-TFB hydrodynamics behavior, the flow pattern characterization of C-TFB was evaluated by measuring voidage in the system in this study.

To investigate C-TFB flow patterns/regimes, the pressure drop measurement between pressures sensors at the axial direction were assembled along the riser height. Gas velocities become an effecting parameter in this study since when the gas velocity increased, the flow patterns/regimes changed. The computation of the pressure drop profile were used to calculate the axial solid volume fraction profile by connecting to MultiLab data logger version 4.0. It was recorded and collected data, then exported into MS Excel. The comparison between the conventional flow pattern gas velocity such as bubbling fluidization and fast fluidization and the novel C-TFB were distinguished in term of solid volume fraction (ε_s).

A more detailed analysis of the solid volume fraction can be done by examining the instantaneous solid volume fraction distribution. This can be used to classify different flow patterns/regimes to identify observed behavior. The calculation was determined by the obtained differential pressure between two separate pressure sources or pressure drop, ΔP. A two-detector setup aligned with 0.1 m apart (ΔH) was used to detect particles in the riser. The relationship between ΔP and ε_s is shown in the equation as followed,

$$\Delta P = \rho_s g H \varepsilon_s \tag{3.1}$$

which ρ_s is the solid density (kg/m^3), g is the gravity acceleration (m/s^2) and H is the distance between two pressure taps, respectively.

The experimental operating conditions used in this study are: (i) three different superficial gas velocities varying from 0.01 to 2.5 m/s; (ii) constant of solid loading of 0.5 kg; (iii) ambient conditions (atmospheric pressure and room temperature).

3.3.3 CO_2 adsorption

For CO_2 adsorption process, the major consideration for the measurement of CO_2 capture capacity, including adsorption temperature, water pre-treatment in the inlet feed gas are concerned. These parameters have a greater effect on the CO_2 adsorption procedure. In this study, the inlet feed gas composition for the direct adsorption containing 12%vol CO_2, dry basis and balance N_2 constantly for all experiments. The K_2CO_3/Al_2O_3 solid sorbents of 500 grams were loaded into the riser. A mixed gas of CO_2 and N_2 was passed through a temperature controlled gas bubbler associated with water vapor in order to simulate a real flue gas condition. To prevent water vapor condensation, the transfer tube was heated with heating tape along the height of the circulating fluidized bed system. Assuming the mixed gas stream from the gas bubbler was saturated with water vapor. Then, it can estimate the system relative humidity or water vapor percentage. At the exit of the riser, the filter was installed to get rid of water vapor from an unadsorbed portion of the feed gas stream containing CO_2 and water vapor, then the flue gas at the outlet was kept in gas bags for measuring the amount of CO_2 concentration by Gas Chromatography (GC). Table 3.2 shows experimental conditions of an adsorption temperature effect on CO_2 adsorption.

3.3.4 CO_2 Evaluation

- CO_2 capture capacity

In this study, the breakthrough curve was represented the term of outlet CO_2 concentration adsorbed by K_2CO_3 in solid sorbent with time (the measurement data is shown in Appendix A) which can determine by the area under the breakthrough curves for obtaining the CO_2 capture capacity. The expression of the capture capacity is the amount of the adsorbed CO_2 per 1 g of K_2CO_3 when the sorbent is saturated.

- CO_2 removal fraction (F)

The investigation of CO_2 adsorption efficiency can observe from the CO_2 removal fraction (F). The CO_2 removal fraction was defined as the follows:

$$F = 1 - \frac{[CO_2]_{output} \cdot Fr_{output}}{[CO_2]_{input} \cdot Fr_{input}} \tag{3.2}$$

where $[CO_2]$ is CO_2 concentration (%vol.), Fr is the gas flow rate (l/min). The calculation of output flow rate, Fr_{output}, is come from the difference between the input flow rate, and adsorbed CO_2 flow rate.

3.3.5 Solid sorbent characterization

- Brunner-Emmett-Teller (BET) method is used for measuring the specific surface area of solid material by N_2 adsorption at -196 ^{o}C.
- Particle size analysis is used to measured particle size and size distribution of K_2CO_3/Al_2O_3 sorbent.
- X-ray fluorescence analysis (XRF) is used for observing the amount of composing elements of alkaline metal impregnated on solid material.

- X-ray diffraction (XRD) is used to identify crystalline structure of solid material phase.

3.3.6 Regeneration kinetics

Potassium hydrogen carbonate ($KHCO_3$) AR grade from Ajex Finechem Pty Ltd was heated by using the Pyris Diamond Perkin Elmer thermogravimetric the analyzer apparatus. Constant flow rate of 50 ml/min N_2 was used as an inert gas throughout the experiment in order to maintain the thermal decomposition. An approximate weight of samples to test per one experiment was 10-30 mg. All sample conditions started with initial and final temperatures of 40 and 600°C, respectively. Four different heating rates, 5, 10, 20 and 40°C/min under N_2 atmosphere and TG and DTA operating conditions were shown in Table 3.3. The results of TG and DTA data were reported in previous chapter, Fig. 5.3.

3.3.7 Kinetic model parameters

For better understanding the CO_2 sorption process, the chemical kinetics is needed to consider. In general, the mass transfer term and reaction kinetics may be expressed in the chemical kinetic term. For the non-catalytic gas-solid particle, there are various mathematical models that have been developed for analyzing the reaction progress including the shrinking-core, homogeneous, phenomenological and deactivation simplified models. Among these models, Zhao et al. [68] discovered that the deactivation model showed a good agreement between the mathematical model and the breakthrough curve. Moreover, this model had been used to explain the behavior of solid sorbent activity during CO_2 sorption process. The deactivation model is defined as the diffusion resistance due to the deposition of a product layer over the solid surface. According to this resistance, the reaction rate with time was decreased. The activity of the deactivating solid sorbent, a, may be explained according to the equation

$$a = r / r_0 \tag{3.3}$$

where r_0 is the initial rate of reaction of a fresh solid sorbent and r is the rate of reaction determined at any time. Also, the following conditions can be assumed: The reaction is operated under isothermal condition, the water vapor content is then constant. With the above assumptions, the pseudo-steady state species conservation equation without axial dispersion is expressed as follows:

$$-Q_0 \frac{dC}{dW} - ak_0 C = 0 \tag{3.4}$$

where a is the activity of the sorbent, W is the weight of sorbent, C is the outlet concentration of CO_2, Q_0 is the volumetric flow rate and k_0 is the initial sorption rate constant.

$$\int_{C_0}^{C} \frac{dC}{C} = \left(\frac{k_0 a}{Q_0}\right) \int_0^W dW \Rightarrow \ln\left(\frac{C}{C_0}\right) = -\left(\frac{k_0 a}{Q_0}\right) W \tag{3.5}$$

where C_0 is the initial concentration of CO_2. For the deactivation effect, the calculation of K_2CO_3/Al_2O_3 solid sorbent activity will depend on the hypothesis. There are various forms of deactivation reactions. For independent reaction, which assumed if the first-order with respect to the solid active site and zeroth-order with respect to the concentration of CO_2 (m = 1, n = 0), the activity of solid sorbent can then be described by the following equation:

$$\frac{-da}{dt} = k_d C^n a^m \qquad \text{which } a = a_0 \exp(-k_d t) \tag{3.6}$$

where t is the time, k_d is the deactivation rate constant and *a* is the initial activity of the solid sorbent. Combining Eqs. (3.5) and (3.6) with the initial activity of the solid sorbent as the unity,

$$C = C_0 \exp\left(\frac{k_0 W}{Q_0}\right) \exp(-k_d t) \tag{3.7}$$

After arranging Eq. (3.6), we obtained

$$\ln\left[\ln\left(\frac{C_0}{C}\right)\right] = \ln\left(\frac{k_0 W}{Q_0}\right) - k_d t \tag{3.8}$$

The kinetic parameters, k_d and k_0 were obtained from a linear equation of Eq. (3.7) with the slope of the plot between ln[ln(C_0/C] versus time and the intercept of ln(k_0W/Q_o), respectively.

However, it is possible that the CO_2 concentration can involve in the deactivation rate. The first-order with respect to the solid active site and the concentration of CO_2 are considered (m = 1, n = 1). The parameters in Eq. (3.7) was substituted back in Eq. (3.6) then integrated to get the first correction activity which then substituted again in Eq. (3.4) to obtain correcting solution by integration as follow.

$$\frac{C}{C_0} = \exp\left[\frac{\left[1-\exp\left(\frac{k_0 W}{Q_0}\left(1-\exp\left(-k_d t\right)\right)\right)\right]}{1-\exp\left(-k_d t\right)} \exp\left(-k_d t\right) \right] \tag{3.9}$$

3.4 Results and discussion

This part can divided into two main sections. The first part was investigating the flow regime of a circulating-turbulent fluidized bed since a circulating-turbulent fluidized bed regime combines the advantage of turbulent and circulating fast fluidization regimes as described in section 3.4.1. Usually, the effective operation of a circulating fluidized bed is performed in fast fluidization regime, the transition velocity of the bubbling to turbulent fluidization velocity and transport velocity (U_{tr}) of fast fluidization was investigated to identify a range of flow rate of circulating-turbulent fluidized bed. Measuring the solid hold up along the height of the riser is used to determine the flow pattern of solid in the riser. This result is discussed in section 3.4.2. The second part of this study represented CO_2 adsorption capacity and determined the kinetic parameter for CO_2 adsorption using K_2CO_3/Al_2O_3 solid sorbent by deactivation kinetic model obtained from a circulating-turbulent fluidized bed regime was shown in section 3.4.3 and 3.4.4, respectively.

3.4.1 A circulating-turbulent fluidized bed flow pattern regime

A number of regime transitions were used to determine the flow pattern/regimes in the circulating fluidized bed riser including transition velocity (U_c) and transport velocity (U_{tr})

3.4.1.1 The transition from the bubbling to turbulent fluidization velocity (Transition velocity determination, U_c)

The transition from the bubbling to turbulent fluidization depends on the pressure fluctuations of dynamic pressure and of the pressure drop across the bed. Two transition criteria have been suggested to distinguish the transition from bubbling/slugging to turbulent fluidization. The first criterion is transition velocity, U_c, as the superficial gas velocity when the bubbles or slugs in the bed of particles reach to maximum diameter and the largest standard deviation of the pressure fluctuation. U_c can be defined as the onset of the turbulent fluidization flow regime. The other transition criterion is critical velocity, U_k, a critical velocity on entry into the turbulent regime. When increased the gas velocity, the large bubbles in the bed start to erupt into smaller bubbles at which the standard deviation of the pressure fluctuation become less and stabilize. Several studies have developed correlations for transition velocity comparing with the available correlations and this experiment were given in Table 3.4

In this study, the transition velocity was estimated by determining the standard deviation of pressure fluctuation with different gas velocities. The measurement of pressure fluctuations were obtained by the pressure probes which were located at an axial position of 0.10 m at the bottom of the riser as shown in Fig. 3.3. As gas velocity was increased, the standard deviation of pressure fluctuation in bubbling flow regime increased rapidly due to the coalescence of small bubbles into large bubbles/slugs and break-up reach a balance. It is established that the transition velocity is corresponding to the gas velocity at which this standard deviation reached a maximum.

Therefore, the transition velocity in this study was found to be 0.82 m/s. It can be seen that, above the transition velocity, the standard deviation decreased gradually when the gas velocity increased.

In addition, the comparison between the transition velocity values obtained from the several literatures based on the available correlations and this study was given in Table 3.4. The measured transition velocity by observing the standard deviation of pressure fluctuation at the bottom of the riser in this study is consistent with the range of transition velocity values from the correlations.

3.4.1.2 Transition from turbulent to fast fluidization (Transport velocity, U_{tr})

The transport velocity is defined as the transition between turbulent and fast fluidization regime. The minimum gas velocity required to bring a significant number of particles discharged from the riser. Several approaches were used to calculate the transport velocity of solid in the fluidized bed such as flooding point velocity determination [61], pressure drop calculation as a function of solids circulation rate and superficial gas velocities at the bottom of the column [74] and emptying-times measurement technique of a fast fluidization column [107,108]. Among these approaches, the emptying-times is performed the most interesting technique because this method is simple and quick [81]. Therefore, in this study, the empty-time was used to estimate the transport velocity. This approach is investigated time required corresponded to all solids entrainment when increased the superficial gas velocity. For all experiments, there are no fresh solid required to feed into the column since this approach measurement was not sensitive to the initial solid loading mass in the column. The initial solid loading was conducted with the sample of 60 grams. At low superficial gas velocities, the result from Fig. 3.4 showed that there was no significant particle entertainment from the riser. As a result, the measurement of time required to empty the bed was longer than high superficial gas velocities. When the gas velocity is increased, the solid particle could be carried out from the riser in a shorter period of time because there is no make-up solid recycle in the system. The transport velocity was taken to be the intersection of the lines of low and high slopes and was found to be 2.20 m/s. Several studies have developed correlations for transport velocity as shown in Table 3.5, the obtained transport velocity was compared with the available correlations are shown.

The transition velocity of the bubbling to turbulent fluidization velocity (U_c) and transport velocity (U_{tr}) were investigated in this topic. A summary of the transition velocities from correlations comparing with this experiment is provided in Table 3.4. There are 3 different ranges of gas velocities including fixed bed, bubbling and turbulent fluidization, corresponding with various flow patterns. Consequently, the operating velocity for a circulating-turbulent fluidized bed regime should be operated between these velocities.

3.4.2 Time-average solid volume fraction in the circulating-turbulent fluidized bed (C-TFB)

The measurement of the axial profiles of the pressure along the height of the riser were obtained by pressure probes which can display in term of pressure transducers. Consequently, all pressure probes at axial direction were used to determine the solid volume fraction as described in the experimental part. The comparison of axial solid volume fraction profiles between bubbling fluidization, turbulent fluidization, circulating-turbulent fluidized bed (C-TFB) and fast fluidization regimes are shown in Fig. 3.5. It can be seen that, the solid volume fractions of the bubbling fluidization were nearly uniform at the bottom of the bed and then was suddenly decreased to zero at a position higher than 0.35 m from the distributor, because there were no solid left in this region. When the superficial gas velocity increased to reach the transition velocity (U_c), the solid volume fraction in the riser become dense at the bottom and dilute at the top of the bed which is the flow behavior of the turbulent fluidization. Due to solid in the bed could be easily distributed by gas in the turbulent regime, the solid volume fraction at the bottom was lower than that of bubbling regime. Therefore, the solid volume fraction profiles along the height of the turbulent regime were gradually decreased along the height. To distinguish the circulating-turbulent fluidized bed regime or at a superficial gas velocity of 1.0 m/s, it can be seen that the solid volume was relatively similar to the turbulent fluidization regime. However, the solid volume fraction shows the dense region at the top of the bed. The averaged solid volume fraction was 0.15. For the fast fluidization regime or at a superficial gas velocity of 2.2 m/s, the solid volume fraction profile became S-shaped as is typical of a riser operated with the fast fluidization regime.

In summary, the axial solid volume fraction profiles of the circulating-turbulent fluidized bed regimes can be obtained at superficial gas velocity of 1.0 m/s. This operating condition will be applied to study further in the single-cycle CO_2 adsorption using K_2CO_3/Al_2O_3 solid sorbent.

3.4.3 CO_2 adsorption process in circulating-turbulent fluidized bed

After obtaining the hydrodynamic of C-TFB, the CO_2 adsorption were used to study this regime CO_2 capture behavior. The experiments were carried out with 60°C at the CO_2 concentration of 12 %vol. dry basis. The effect of water contents in feed gas in fluidized bed reactor was investigated by Jaiboon et al. [69], the results showed that the appropriate water content for CO_2 adsorption is related to the CO_2 concentration in flue gas inlet due to the stoichiometry in Eq.(1.1). So, this study will use 18.4 %vol. of water content in the feed gas. Figure (6.6a) shows the effect of CO_2 adsorption on different flow patterns/regimes and CO_2 capture capacity. At 60°C, the CO_2 breakthrough curve of fixed bed, bubbling fluidization and C-TFB showed similar behavior. At the beginning of time, the CO_2 breakthrough curves showed that outlet fraction become constant then decreased when the reaction time increased. When the inlet velocity increased to turbulent fluidization regime, the constant CO_2 breakthrough curve could not be obtained visibly at the beginning of time.

The comparison of CO_2 capture capacity between the different regimes are shown in Figure (3.6b), it can be seen that, C-TFB regime provided the highest CO_2 adsorption capacity after 4 minute, then the CO_2 removal fraction of C-TFB decreased and remained constant until 20 minutes. This is due to the characteristic of circulating fluidized bed which solid sorbent can be returned at the bottom of the riser. In this regime 500 grams of solid sorbent was used in order to provide a sufficient time to complete cycle for determining the CO_2 capture capacity. The calculation of the deactivation model and experimental breakthrough curves were consistent with each other.

3.4.4 Evaluation kinetic parameters

Table 3.6 showed the corresponding kinetic parameter of CO_2 sorption between different flow patterns/regimes. The k_0 parameter are increased with increasing inlet gas velocity. C-TFB fluidization regime provided similar values of k_0 and k_d with bubbling fluidized bed while turbulent fluidization regime obtained lower k_0 and k_d. As can be seen from Fig.3.5a, the breakthrough curve pattern of C-TFB was quite similar bubbling fluidized bed regimes. At the beginning of time, the CO_2 breakthrough curves showed a maximum removal fraction when the system was initiated and then the removal decreased when the reaction time increased. On the other hand, the dimensionless k_0 of turbulent fluidization gave the lowest value due to the flow could not possibly removed the concentration of CO_2 at the beginning. In addition, turbulent fluidization regime acquired the highest the deactivation rate, k_d. The slightly deviation is due to the diffusion resistance of unreacted reactant layer over the solid sorbent. Similar to the previous reason, the backward reaction and the activation energy explained the observed results. The low deactivation of solid sorbents then found.

3.5 Conclusion

In this study, the investigations of the pressure drop profile at different height of the riser were obtained for observing the circulating-turbulent fluidization regimes (C-TFB) solid volume fraction profile. The hydrodynamic behavior of the C-TFB provided that the solid volume fraction showed uniformly profile along the bed height at the gas velocity at 1.0 m/s. For CO_2 capture study, C-TFB regime provided the highest CO_2 adsorption capacity. Moreover, C-TFB fluidization regime provided similar breakthrough curve pattern and values of k_0 and k_d with bubbling fluidized bed.

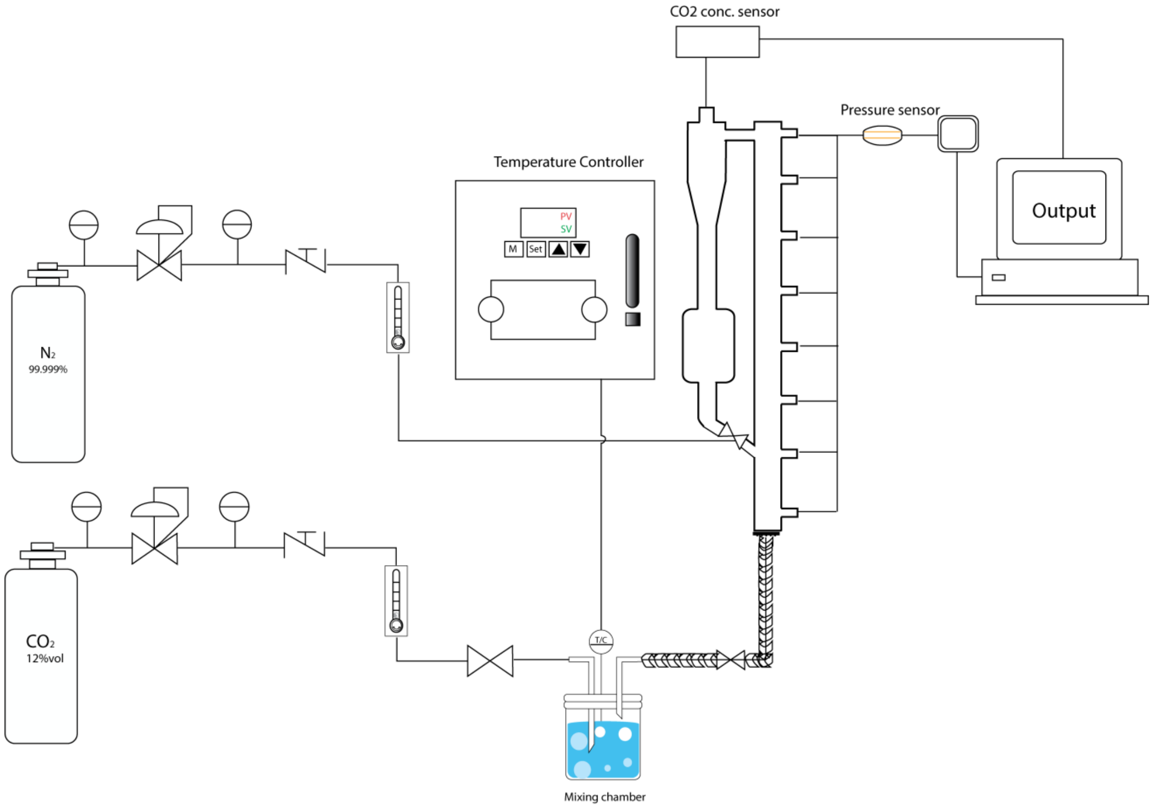

Fig. 3. 1 Schematic diagram of a lab-scale circulating fluidized bed unit in this research.

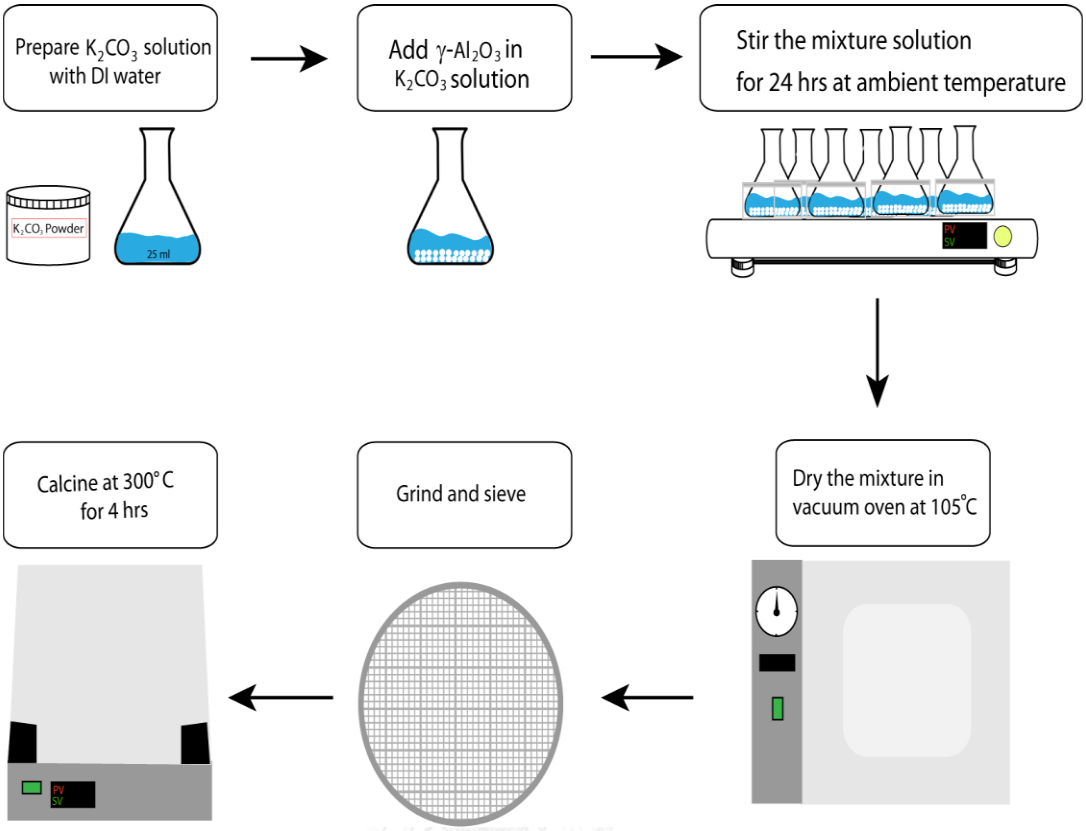

Fig. 3. 2 The outline of the procedure used for preparing K_2CO_3/Al_2O_3 solid sorbent process.

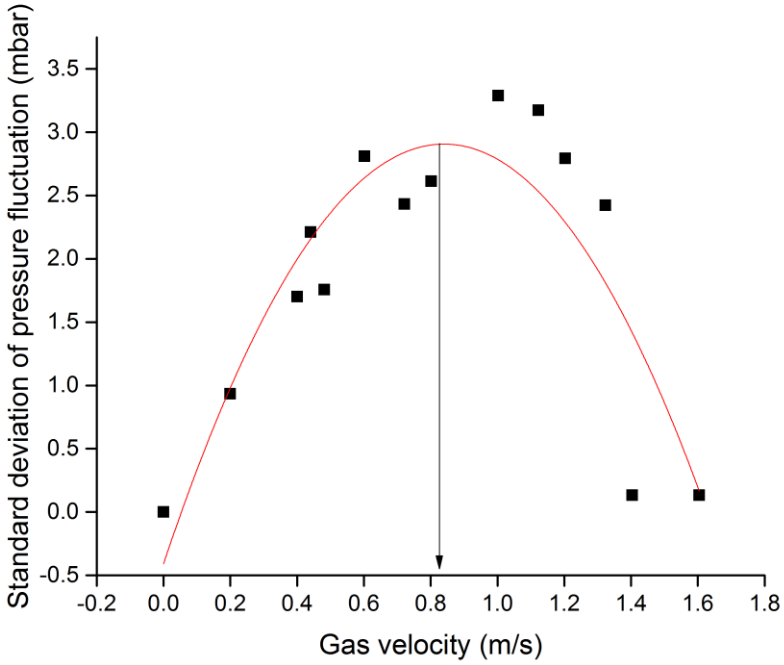

Fig. 3. 3 Transition velocity by standard deviation of pressure fluctuation-gas velocity curve, position of the probe: 0.20 m

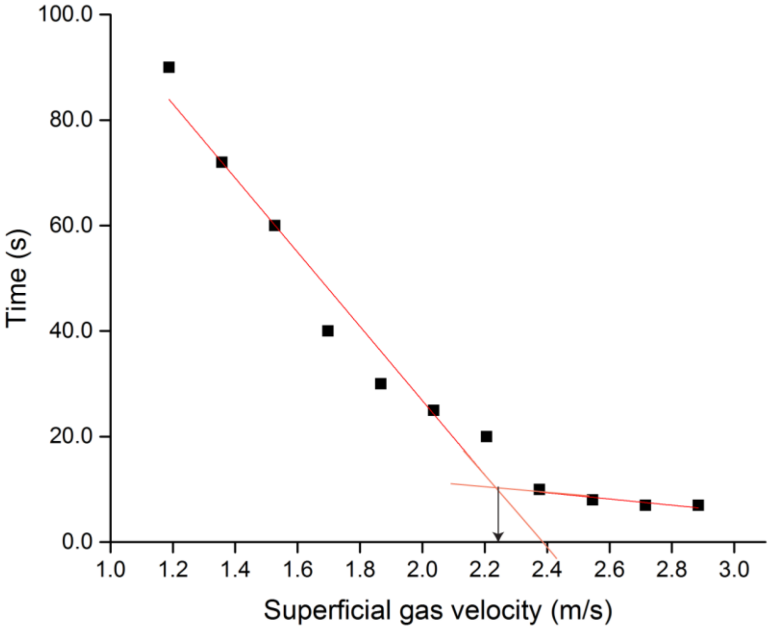

Fig. 3. 4 Emptying–time of solid used in this study at various superficial gas velocities for solid loading of 60 grams.

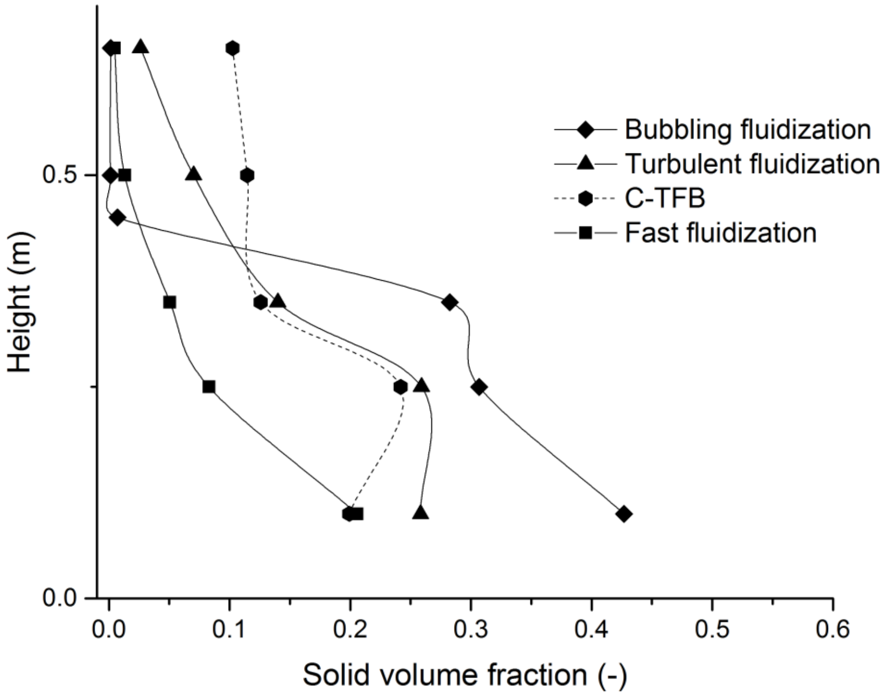

Fig. 3. 5 Solid volume fraction profiles along the height of the riser at different superficial gas velocities (U_g).

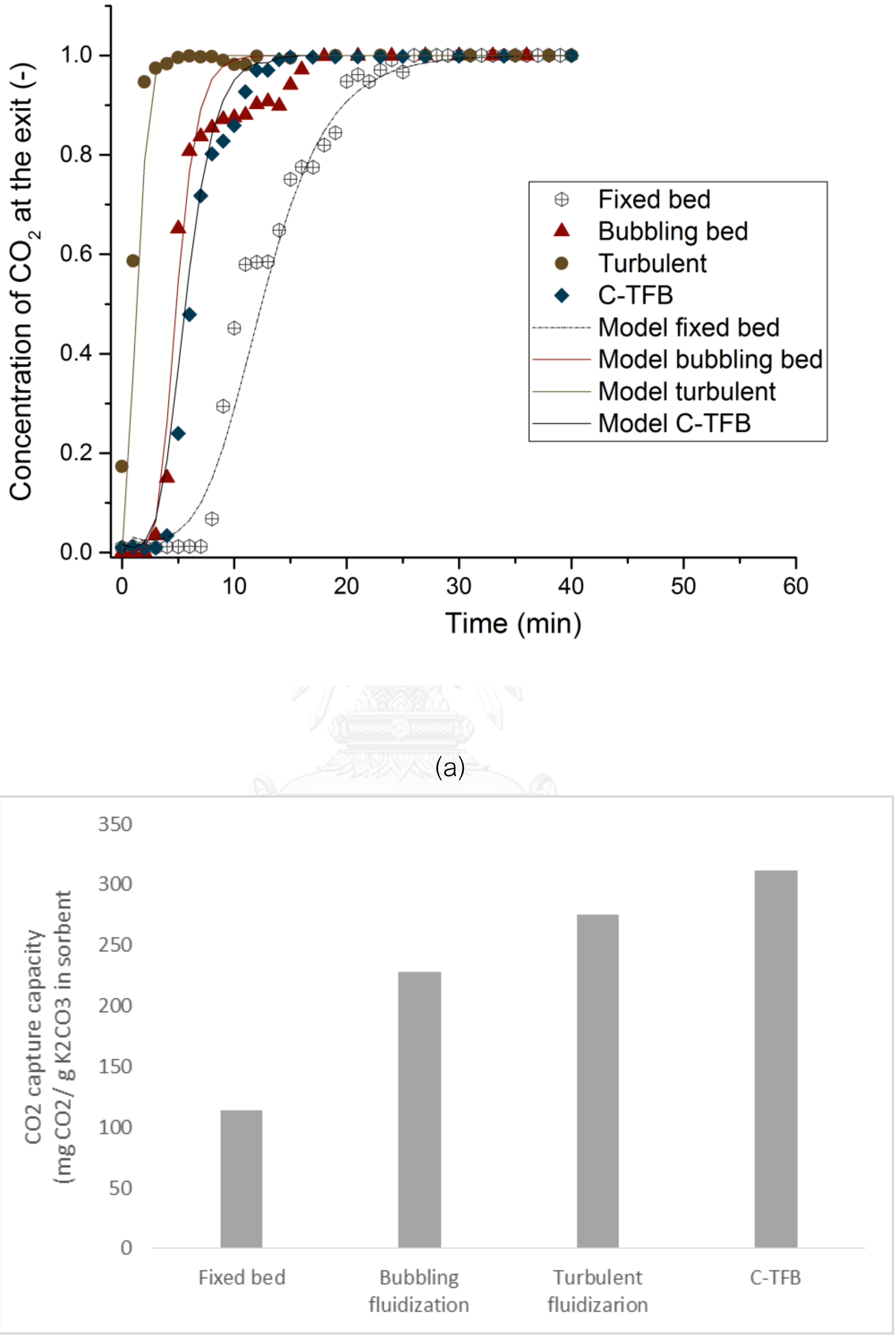

Fig. 3. 6 Effect of adsorption on CO_2 removal fraction at different regimes

(a) different flow patterns/regimes (b) CO_2 capture capacities.

Table 3. 1 Characteristics of prepared K_2CO_3/Al_2O_3 solid sorbent in this research.

Sorbent Properties	Value
K_2CO_3/Al_2O_3 BET surface area (m^2/g)	99.51
Pure Al_2O_3 BET surface area (m^2/g)	117.94
K_2CO_3/Al_2O_3 Pore volume (cm^3/g)	0.17
Pure Al_2O_3 Pore volume (cm^3/g)	0.21
Actual weight of K_2CO_3 impregnated on γ-Al_2O_3 (%wt)	12.9
Diameter (d_p, μm)	150
Density (ρ_s, kg/m^3)	3,900

Table 3. 2 Experimental conditions of an adsorption temperature effect on CO_2 adsorption.

Conditions	Value
Adsorption temperature (°C)	60
Pressure (atm)	1
Flow pattern regime	Circulating-turbulent fluidized bed
Gas velocity (m/s)	1.0
Solid loading (kg)	0.5
Gas composition (vol%)	12% CO_2 dry basis with H_2O 18.5%, N_2 balance

Table 3. 3 Experimental conditions for determining regeneration kinetics.

Conditions	Value
Initial temperature (°C)	40
Terminate temperature (°C)	600
Pressure (atm)	1
Diameter (μm)	500
Density (kg/m_3)	2,170
N_2 Flow rate (ml/min)	50
Heating rate (°C/min)	5, 10, 20, 40

Table 3. 4 Comparison between transition velocities from correlations and velocity determined in this research.

References	Correlations of U_c	U_c (m/s)
Yerushalmi and Cankurt (1979)	$U_c = 3(\rho^*d_p)^{0.5} - 0.77$	0.32
Lee and Kim (1988)	$Re_c = 0.7Ar^{0.455}$	1.00
Leu, Huang and Gua (1990)	$Re_c = 0.568Ar^{0.578}$	1.60
Horio (1991)	$Re_c = 0.936Ar^{0.472}$	1.46
Bi and Grace (1995)	$Re_c = 0.565Ar^{0.461}$	0.83
This work		0.82

Table 3. 5 Comparison between transport velocities from correlations and velocity determined in this research

References	Correlations of U_{tr}	U_{tr} (m/s)
Parales et al.	$U_c = 3(\rho * d_p)^{0.5} - 0.77$	2.36
Bi and Fan (1992)	$Re_c = 0.7Ar^{0.455}$	2.66
Lee and Kim (1990b)	$Re_c = 0.568Ar^{0.578}$	2.37
Adanez et al. (1993)	$Re_c = 0.936Ar^{0.472}$	3.01
Chehbouni et al.	$Re_c = 0.565Ar^{0.461}$	1.13
This work		2.20

Table 3. 6 Effect of different flow regimes on breakthrough curves of outlet CO_2 fraction and their corresponding kinetic parameters with m = 1, n = 1 and 18.4 vol%. water content).

Fluidization regime	$k_0\tau$ (dimensionless)	k_d (m^3/kmol·s)	R^2
Fixed bed	3.102	0.269	0.99
Bubbling	3.813	0.851	0.99
Turbulent	1.595	1.900	0.96
C-TFB	3.627	0.8630	0.98

CHAPTER IV

Chemical Kinetic for regeneration of potassium carbonate solid sorbent using temperature

In an adsorption process, CO_2 was adsorbed onto the potassium carbonate solid sorbent, resulting in the increasing of solid sorbent weight due to CO_2 and water vapor depositions. With sufficient CO_2, proper amount of H_2O and suitable temperature conditions, potassium carbonate on alumina support (K_2CO_3/Al_2O_3) is transformed to potassium bicarbonate ($KHCO_3/Al_2O_3$) and physically blocks on the surface of porous solid sorbents. The process which is used to remove CO_2 from particulate phase is called regeneration. Thus, in this chapter, kinetic study of solid state decomposition of potassium bicarbonate will be investigated.

4.1 Kinetic study of solid state decomposition

The kinetic study for the degradation mechanism of potassium bicarbonate solid sorbent is considered as an irreversible first-order reaction. Using the clarification of the single-step kinetic equation of solid state decomposition, the equation is shown as following equation [70, 71]. The single-step equation provides all the solid reactant that can be converted to the products by using the same amount of the initial input of energy.

$$A(solid) \rightarrow B(solid) + C(volatile) \tag{4.1}$$

For the first order reaction, the general rate law can be expressed in the form below,

$$Rate = \frac{d[A]}{dt} = -k[A] \tag{4.2}$$

Eq. (4.2) is considered in term of concentration. Since the concentration of solid cannot be measured, so this concentration is practically replaced by the extended conversion of the reactant, α , describing the weight of potassium bicarbonate used at the presence of time divided by the total weight loss of potassium bicarbonate.

$$\alpha = \frac{w_0 - w}{w_0 - w_f} \tag{4.3}$$

where w_0 is the initial weight of potassium bicarbonate (mg), w is potassium bicarbonate (mg) at any temperature T and w_f is the final weight of potassium bicarbonate (mg). This conversion is in the range of $0 \le \alpha \le 1$ which comes from weight loss or heat of reaction evaluation. Substituting the extended conversion, α , in Eq. (4.2)

$$Rate = \frac{d\alpha}{dt} = k\left(1-\alpha\right) \tag{4.4}$$

Integrating this equation we obtain,

$$-\ln(1-\alpha) = kt \tag{4.5}$$

Eqs. (4.4) and (4.5) represents the reaction model obtained from first-order model in the differential, $f(\alpha)$, and integral forms, $g(\alpha)$, respectively. Table 4.1 shows various forms of the reaction models. Therefore, the governing kinetic equation can be arranged the rate constant considering as a function of temperature-dependent and the extended conversion of reactant, as follows

$$\frac{d\alpha}{dt} = k(T)f(\alpha) \tag{4.6}$$

$$g(\alpha) = kt \tag{4.7}$$

The temperature-dependent rate constant can be investigated by substituting Arrhenius equation, which gives

$$\frac{d\alpha}{dt} = A\exp\left(\frac{-Ea}{RT}\right)f(\alpha) \tag{4.8}$$

where t is time (min), the Arrhenius parameters composed of A and E_a are the pre-exponential factors (K^{-1}) and the activation energy (kJ/mol). R is the gas constant $(kJ/mol \cdot K)$.

Typically, to investigate the kinetic parameters of many solid phase chemical reactions which is recommended by the International Confederation of Thermal Analysis and Calorimetry (ICTAC) Kinetics Committee, the multiple heating rates will be applied than using only one heating rate to overcome the deficiency problems. On the basis of experiments, the kinetic parameters can be provided under two methods, isothermal and non-isothermal methods. For the isothermal method $(i.e., T = const.)$, the rate constant of each appropriate reaction model was evaluated from the integral form as result of Eq.(4.7) at several temperatures. And the kinetic parameters were obtained from the slope of the plot between $g(\alpha)$ and temperature. While the non-isothermal method, potassium bicarbonate samples are heated at a multi-constant heating rate mechanisms. At any heating rate, $\beta = \frac{dT}{dt}$ we obtain,

$$\frac{d\alpha}{dT} = \frac{d\alpha}{dt} \times \frac{dt}{dT} \tag{4.9}$$

substituting $\frac{d\alpha}{dT}$ in Eq. (4.8)

$$\frac{d\alpha}{dT} = \frac{A}{\beta} \exp\left(\frac{-Ea}{RT}\right) f(\alpha) \tag{4.10}$$

$$g(\alpha) = \int_0^\alpha \frac{d\alpha}{f(\alpha)} = \frac{A}{\beta} \int_0^T \exp\left(\frac{-E_a}{RT}\right) dT \tag{4.11}$$

Substituting x ≅ Ea/RT in Eq.(5.11),

$$g(\alpha) = \frac{AE_a}{\beta R} \int_\alpha^\infty \frac{exp^{-x}}{x^2} dx = \frac{AE_a}{\beta R} p(x) \tag{4.12}$$

where p(x) in Eq.(4.12) is the temperature integral which cannot generally define the exact solution. However, this term can be estimated from some empirical interpolation equations by numerical integration.

There are two methods were used for analyzing non-isothermal solid-state kinetic data from TGA: model-fitting and model-free types. Both can be determined in isothermal and non-isothermal conditions [71]. The selected methods in this study covered all the literature method.

4.1.1 Kissinger-Akahira-Sunose (KAS) Method

This method was developed by Kissinger-Akahira-Sunose [72, 73]. The assumption for the temperature integral was used, $p(x) \cong e^{-x}/x^2$, for $20 \leq x \leq 50$, as shown,

$$\ln\frac{\beta}{T^2} = \ln\frac{AR}{E_a g(\alpha)} - \frac{E_a}{RT} \tag{4.13}$$

To determine the order of the reaction, n, using the shape index factor, S, can be obtained from Eqs.(4.14) and (4.15) by Kissinger index [72, 74] which measures the absolute value of the ratio between the slope of the curve at the inflecting point toward the left (a) and the right (b) of its TG tangent lines.

$$S = \left|a / b\right| \tag{4.14}$$

$$n = 1.26\sqrt{S} \tag{4.15}$$

4.1.2 Flynn-Wall-Ozawa (FWO) Method

Flynn-Wall-Ozawa [75, 76] proposed the temperature integral function using Doyle's approximation ($\log p(x) \cong -2.315 - 0.4567x$) obtained from the thermal decomposition of octamethylcyclotetrasiloxane and polytetrafluoroethylene powders in Eq.(4.16) [77, 78]. The order of reaction, n, can be determined by the same method as KAS method using Eqs. (4.14) and (4.15).

$$\log\beta = \log\frac{AE_a}{g(\alpha)R} - 2.315 - 0.4567\frac{E_a}{RT} \tag{4.16}$$

4.1.3 Park-Kim Method

Kim and Park approach [79] developed the mathematical model shown the relationship of heating rate and derivative thermogravimetric curves as follows:

$$\ln\beta = \ln Z + \ln\left(\frac{E_a}{R}\right) + \ln\left[1 - n + \frac{n}{0.944}\right] - 5.3305 - 1.0516\left(\frac{E_a}{RT_m}\right) \tag{4.17}$$

$$n = (E_a(1-\alpha_m)/((RT_m^2)(d\alpha/dT)_m))) \tag{4.18}$$

To calculate the order of reaction, n, for this method, the parameters in Eq.(4.18) [80], α_m , T_m and $(d\alpha/dT)_m$ in Eqs.(4.17) and (4.18) are represented the maximum conversion, maximum decomposition temperature and maximum weight loss rate, respectively.

4.1.4 The Analytical Method

This method is generally derived from the expression of the reaction rate of the solid state mechanism in Eq. (4.10) where the reaction conversion, $f(\alpha)$, is the nth reaction order from Table 4.1. The relationship between the weight loss and temperature can be written in term of the activation energy and the frequency factor. It can be calculated by using Eq.(4.19), when n≠1 [81];

$$\alpha = 1 - \left\{1 - (n-1)\left(\frac{ART^2}{\beta E_a}\right)\left(1 - \frac{2RT}{E_a}\right)\exp\left(\frac{E_a}{RT}\right)\right\}^{\frac{1}{1-n}} \tag{4.19}$$

4.2 Experimental

Ajex Finechem Pty Ltd AR grade Potassium hydrogen carbonate ($KHCO_3$) was used to investigate on the Pyris Diamond Perkin Elmer thermogravimetric analyzer apparatus. The average particle size was 500 μm and density was 2,170 kg/m^3. The weight of the sample for each run was 20 mg. All samples were operated from 40 to 600°C by utilizing heating rates of 5, 10, 20 and 40°C/min under a flow of N_2 atmosphere (50 ml/min), were used to carry out TG and DTG data.

4.3 Results and discussion

4.3.1 Thermogravimetric the analysis

As stated in the experimental section, the decomposition of $KHCO_3$ particles in N_2 atmosphere corresponding to a chemical reaction studied can be provided. The results are illustrated in term of fraction of mass loss (TG) which represented the relationship between mass losses of four different heating rates. The rate of fraction of mass loss (DTG) which represented the relationship between rate of mass loss and temperature of the same heating rates as TG in Fig 4.1(a) and 4.1(b), respectively. For the chemical reaction characteristic, $KHCO_3$ particle started heating process between 40°C for initial temperature and the final temperature of 600°C. Apparently, TG results displayed only one stage for thermal decomposition of each heating rate. The particle is decomposed at 120°C and thermally abrogated within relatively narrow regions between 200 and 300°C. As the temperature increases, the fraction of weight loss also increases, because the decomposition process is irreversible reaction. Moreover, when particles reached the decomposition temperature, the releasing of CO_2 is observed, which led to a fraction of mass loss. Fig. 4.1(b) shows DTG curves of $KHCO_3$ particles at heating rates of 5, 10, 20 and 40°C/min had one maximum decomposition temperature peak. The maximum slope of mass loss and the slope gradually decreased with the increase of heating rates. Since the decomposition temperature at the beginning of 5°C and the decomposition range is narrower than the others, there is not much difference temperature lag between environment and system when the system is heated. Particles entirely have time to absorb the heat and start to decompose earlier. Therefore, a heating rate of 5°C/min provided the maximum slope and 40°C/min provided the minimum slope, respectively.

It can be seen from the TG and DTG graphs, the rate of fraction of mass loss increased when the decomposition temperature increased accordingly. At the highest heating rate, TG and DTG curves displayed similar trends which were sharply decomposed peak. Besides, the temperature gradient between the experimental system and the environment apparently shifts to the highest fraction of mass loss at higher temperature regions when increasing heating rate.

4.3.2 Kinetic parameter analysis

In order to evaluate the kinetic parameters such as the order of the reaction (n), the activation energy (Ea) and the pre-exponential factor (A), the acquiring results obtained from four maximum mass loss peaks of each heating rate from thermogravimetric analysis were used. The KAS method plot between $\ln(\beta/T^2)$ versus temperature, the FWO method plot between $\log(\beta)$ versus temperature and Park-Kim method plot between $\ln(\beta)$ versus temperature are displayed in Fig.4.2(a), 4.2(b) and

4.2(c), respectively. The order of the reaction (n) for each heating rate of KAS method was obtained from the absolute value of the ratio of the slope from the inflecting point toward the left and the right of its TG tangent lines. The linear regressions and the correlation coefficients (R^2) are also shown. The activation energy (Ea) and the pre-exponential factor (A) can be calculated from the slope and intercept of linear regression plot, respectively.

The results obtained from the analytical method in Eq.4.19 were determined using MATLAB software. Table 4.2 shows the results of n, A and Ea of $KHCO_3$ obtained by KAS, FWO, Park-Kim and the analytical methods. While n of bicarbonates are close to 2. It can be seen that, the obtained n values of KAS and FWO methods were the same and A and Ea were quite similar. Due to these two methods being derived from the same origin, Eq.(2), they are developed an approximate solution in terms of temperature integral function, *p(x)*. The computational results obtained from the analytical method were derived from the equations of single decomposition. This is due to the decomposition of $KHCO_3$ are the second-order reaction. The exact order of reaction in these equations should be 2. According to Hisatsune and Adl experiments [82], it was found that, at the high range temperature (420 to 500°C), the thermal decomposition of $KHCO_3$ provided the second order reaction in the bicarbonate monomer form. And the obtained frequency factor, A, was 7.6 x 10^{13}. The calculation obtained from the analytical method used all of the raw data from initial temperature to the final temperature, then converted to the extent conversion (α) in following equation from TG. Whereas KAS, FWO and Kim-Park methods used the range of data from the beginning of the decomposition temperature until the terminated temperature.

4.3.3 Comparison of variation of conversion (α) with temperature during thermal decomposition

The kinetic parameters in Table 4.2 were substituted back in the analytical method (Eq.(4.15)) which order of reaction, $n \neq 1$, to find the reaction conversion (α). Therefore, the reaction conversion versus temperature of KAS, FWO and the analytical methods of $KHCO_3$ particles with correlation coefficients (R^2) values are displayed in Figure 4.3(a) to

4.3(d). The comparison between the actual conversions with heating rates of 5, 10, 20 and 40°C/min and the model estimates are depicted in Figure 4.3(a) to 4.3(d). It can be seen that, the obtained results from the analytical method fitted well with all the experimental data. Their correlation coefficients (R^2) values were higher than 0.95 for all heating rates. While the conversion of KAS, FWO and Kim-Park methods versus temperature were slightly far off from the experimental data during the decomposition reaction.

The reason for the deviation might be as follows, the results from KAS and FWO calculation methods rely on a slope to compute the order of reaction from the inflecting point toward the left or the right of its TG of each heating rate. While Kim-Park method used the maximum decomposition temperature values of DTG for calculating the order of reaction. Moreover, these three methods were used numerical method calculation which was arranged in the integral function terms, *p(x)*, caused the obtained values can be lower than the actual values, while the analytical method was calculated directly from the single decomposition equation. Moreover, correlation coefficients (R^2) values and temperature in Fig.4.3 also showed the reaction conversions (α), which obtained from KAS, FWO and Kim-Park methods have the high deviation at the initial and terminate temperature for all heating rates comparing with the experiment data. This values are the proportion of variability in the experiment data set that is accounted for by a statistical model.

4.4 Conclusion

In this study, TG and DTG experimental data were examined to observe the kinetic parameters including the order of reaction (n), the pre-exponential factor (A) and activation energy (Ea) of $KHCO_3$ decomposition characteristics using non-isothermal analysis. The computational results showed that the analytical method provided the most accurate results comparing with KAS, FWO and Kim-Park methods. According to the experimental data, the correlation coefficients (R^2) values for analytical method were higher than 0.95 for all the heating rates while others were slightly far off. The order of the thermal decomposition of $KHCO_3$ provided the second order reaction. Then, the results of A and Ea will be applied as parameters in models to simulate the chemical reaction and to use for the model optimization.

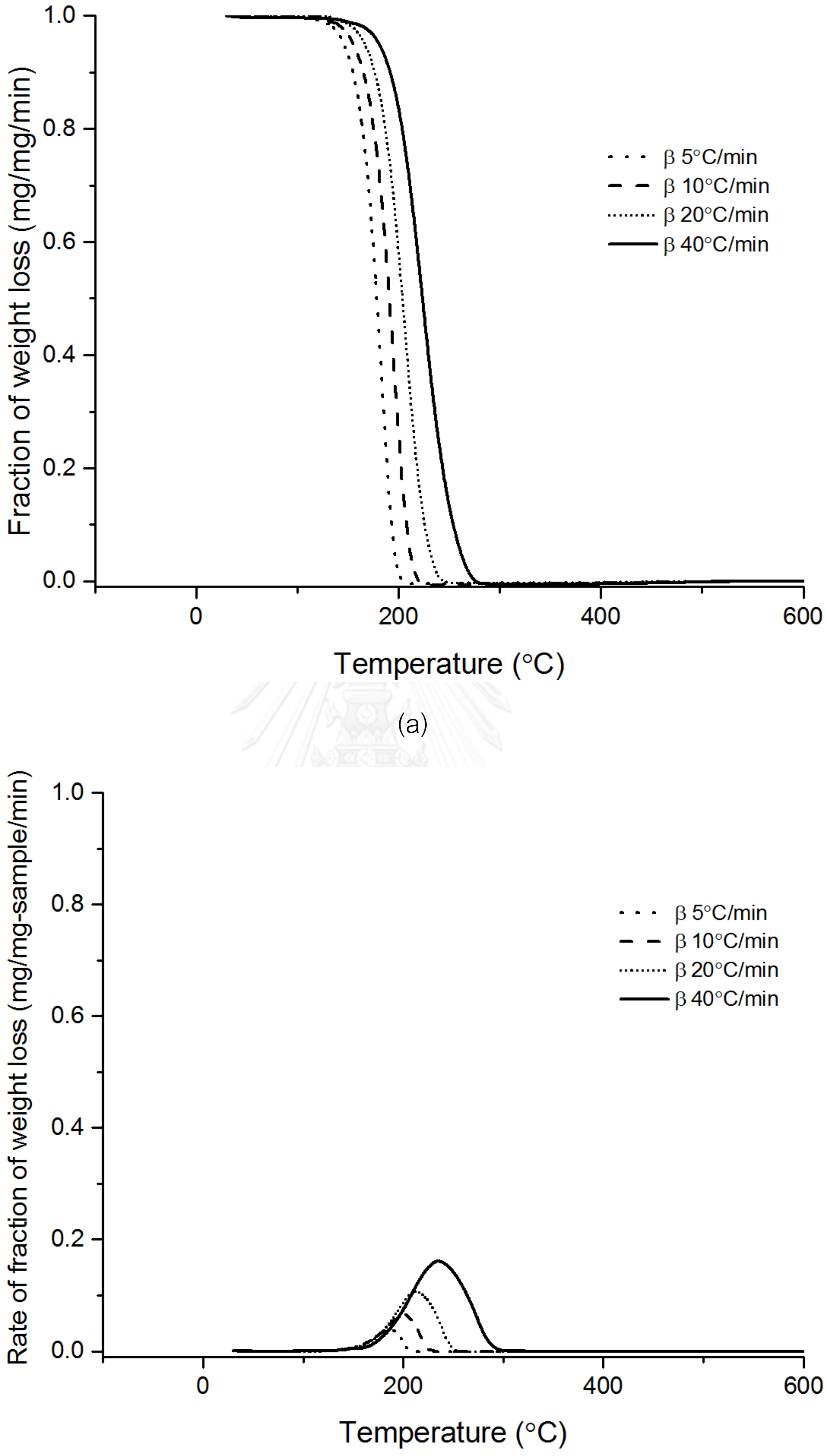

(a)

(b)

Fig. 4. 1 (a) TG curves of $KHCO_3$ using four different heating rates. (b) DTG curves of $KHCO_3$ using four different heating rates.

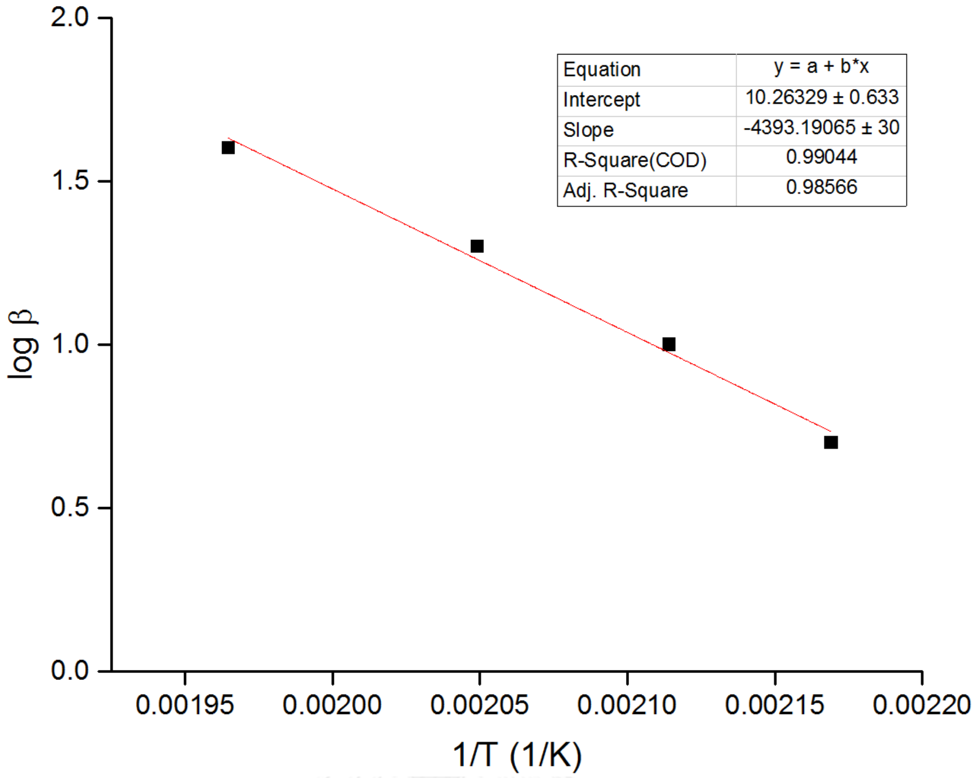
2.0
1.5
1.0
0.5
0.0
log β
0.00195
0.00200
0.00205
0.00210
0.00215
0.00220
1/T (1/K)
Equation
y = a + b*x
Intercept
10.26329 ± 0.633
Slope
-4393.19065 ± 30
R-Square(COD)
0.99044
Adj. R-Square
0.98566

(a)

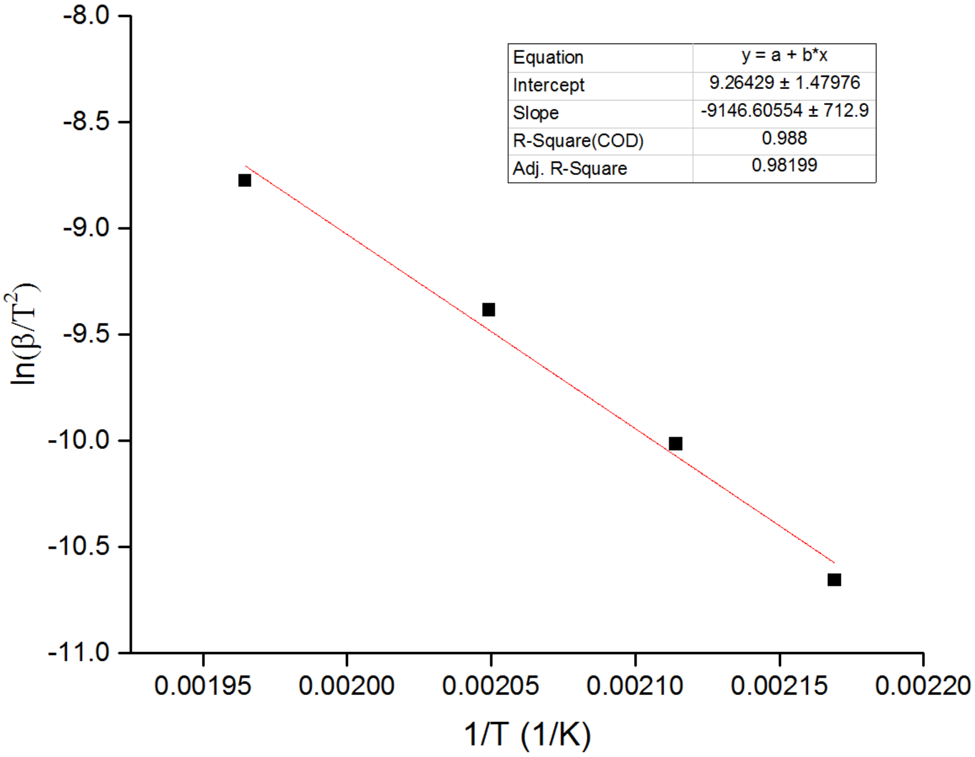
-8.0
-8.5
-9.0
-9.5
-10.0
-10.5
-11.0
ln(β/T²)
0.00195
0.00200
0.00205
0.00210
0.00215
0.00220
1/T (1/K)
Equation
y = a + b*x
Intercept
9.26429 ± 1.47976
Slope
-9146.60554 ± 712.9
R-Square(COD)
0.988
Adj. R-Square
0.98199

(b)

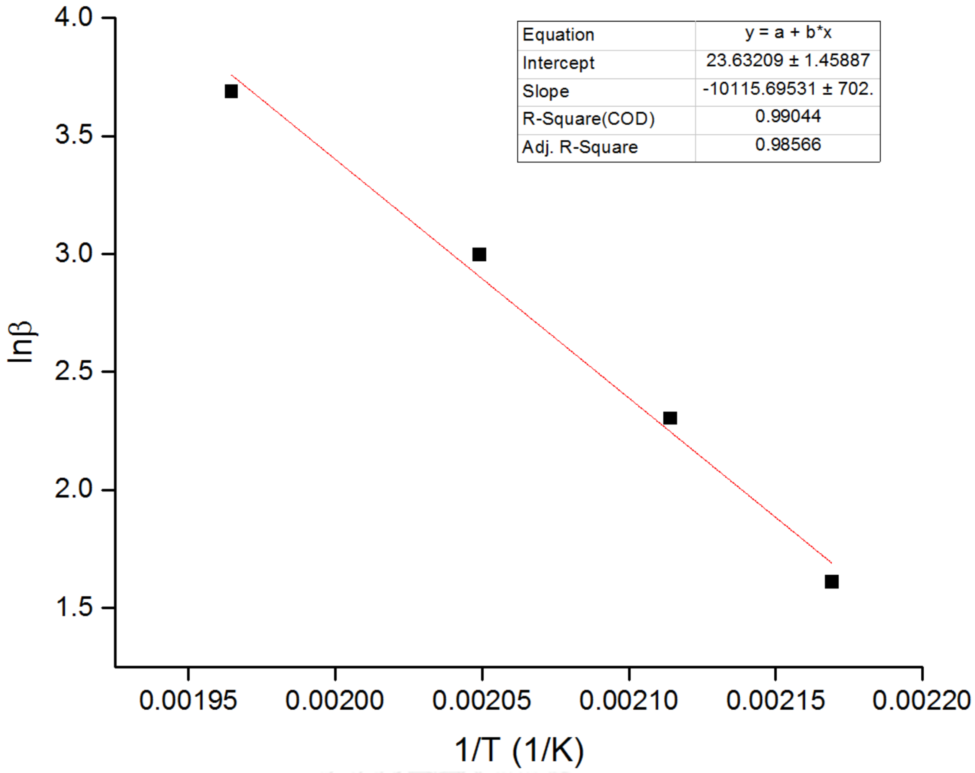

(c)

Fig. 4. 2 (a). The plots of ln(β /T^2) versus temperature of KAS method in Eq.(4.13),

(b) the plots of ln(β) versus temperature of FWO method in Eq.(4.16),

(c) the plots of ln(β) versus temperature of Kim-Park method in Eq.(4.18).

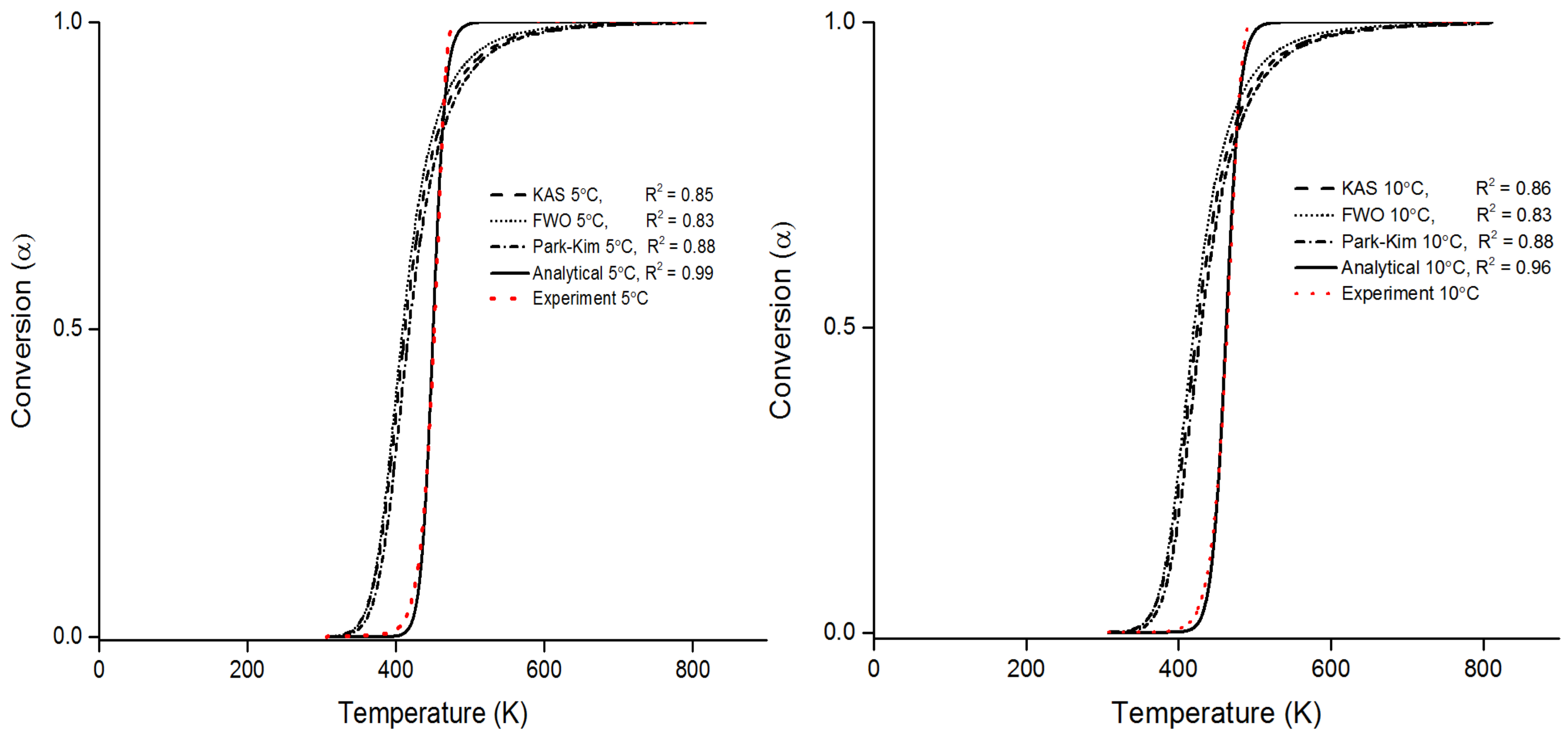

(a)

(b)

Fig. 4. 3 The $KHCO_3$ conversion versus temperature of KAS, FWO, Kim-Park and analytical methods for heating rate of (a) 5, (b) 10, (c) 20 and (d) 40°C/min comparing with the experiments.

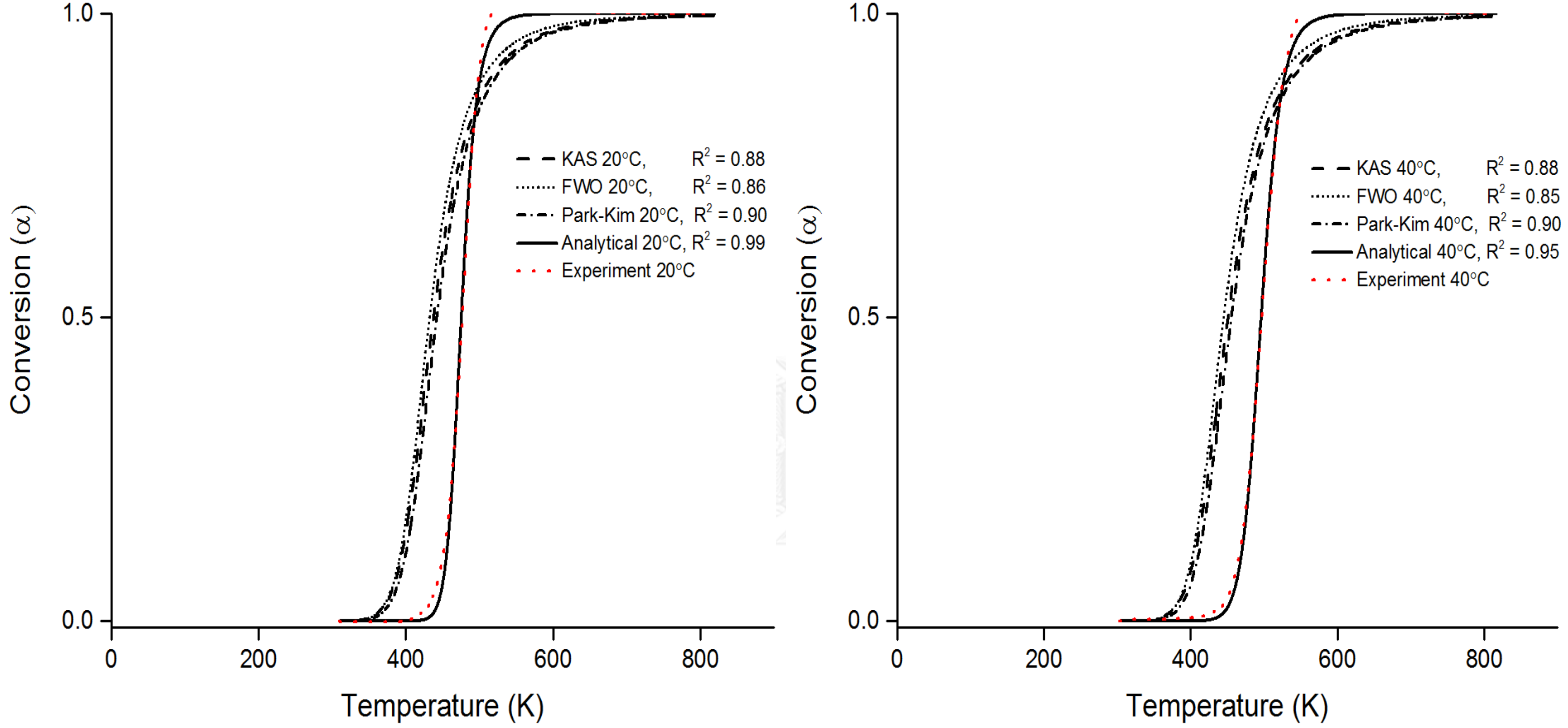

(c) (d)

Fig. 4. 4 The $KHCO_3$ conversion versus temperature of KAS, FWO, Kim-Park and analytical methods for heating rate of (a) 5, (b) 10, (c) 20 and (d) 40°C/min comparing with the experiments.

Table 4. 1 The solid state reaction mechanisms in the general form [83]

Reaction model	$f(\alpha) = (1/k)(d\alpha/dt)$	$g(\alpha) = kt$
Reaction order		
Zero order	$(1-\alpha)^n$	α
First order	$(1-\alpha)^n$	$-\ln(1-\alpha)$
nth order	$(1-\alpha)^n$	$(n-1)^{-1}(1-\alpha)^{(1-n)}$
Nucleation		
Power law	$n(\alpha)^{(1-1/n)}$; n = 2/3, 1, 2, 3, 4	α^n; n = 3/2, 1, 1/2, 1/3, ¼
Exponential law	$\ln\alpha$	α
Avrami–Erofeev (AE)	$n(1-\alpha)[-\ln(1-\alpha)]^{(1-1/n)}$; n = 1, 2, 3, 4	$[-\ln(1-\alpha)]^{1/n}$; n = 1, 2, 3, 4
Prout–Tompkins (PT)	$\alpha(1-\alpha)$	
Diffusional		$\ln[\alpha(1-\alpha)^{-1}] + C\underline{a}$
1-D	$1/2\alpha$	
2-D	$[-\ln(1-\alpha)]^{-1}$	α^2
3-D (Jander)	$3/2(1-\alpha)^{2/3}[1-(1-\alpha)^{1/3}]^{-1}$	$(1-\alpha)\ln(1-\alpha)+\alpha$
3-D(Ginstling-	$3/2[(1-\alpha)^{-1/3}-1]^{-1}$	$[1-(1-\alpha)^{1/3}]^2$
Brounshtein)		$1-2/3\alpha-(1-\alpha)^{2/3}$
Contracting geometry		
Contracting area	$(1-\alpha)^{(1-1/n)}$; n = 2	$1-(1-\alpha)^{1/n}$; n = 2
Contracting volume	$(1-\alpha)^{(1-1/n)}$; n = 3	$1-(1-\alpha)^{1/n}$; n = 3

$\underline{a}$ = Integration constant.

Table 4. 2 The results of n, A and E_a obtained by KAS, FWO, Kim-Park and analytical methods.

$KHCO_3$			
Method	*n*	*A* (min^{-1})	E_a *(kJ/mol)*
Kissinger-Akahira-Sunose (KAS)	1.49	1.40E+08	76.05
Flynn-Wall-Ozawa (FWO)	1.49	5.72E+08	79.98
Kim-Park	1.46	3.90E+08	79.98
Analytical	2.01	5.00E+19	178.10

Chapter V

CFD Design of a Sorber for CO_2 Capture

For the past two decades, computational fluid dynamics (CFD) has become widely accepted tools for solving complex problems. Their results provide better understanding of the hydrodynamics inside the system. Today chemical reactions have been coupling into the model, the change of fluid properties due to the chemical change has been taking into account, leading to more realistic result of the simulation. In this chapter, the simulation of a fluidized bed system with a binary mixture of particles without formation of bubbles described by Gidaspow and Chaiwang [98] was extended by including chemical reactions with heat generations. The energy equations being used by Syamlal and Gidaspow [84] would be applied in this chapter.

.

5.1. Introduction

Global greenhouse gases have increased over the past century because of the intense burning of fossil fuels. Thus, the obliteration of CO_2 in waste gases from fossil fuel burning with the lowest energy requirement becomes a challenge. There are various methods such as adsorption, absorption, membrane separation, cryogenic separation being studied for capturing CO_2.

From The DOE NETL website and recent literatures represented the energy consumption used for commercial amine as a liquid solvent for capturing CO_2 from flue gases is 15 to 30% of the power plants [85-87]. The energy requirement for CO_2 absorber and stripper for a conventional coal fired power plant is 329 MWe [87]. The sections consist of four absorber columns of 8.8 m diameter and 24.4 m height and four strippers will have a diameter of 4.9 m and a height of 22.9 m. The steam requirement is 552 million kg/hr at 0.3 MPa. The diameters are large due to large flue gas emissions. The heights are large due to the use of aqueous amines with low sorption rates and low diffusion coefficients of CO_2 in liquids. The absorption towers are designed using measured rates of rate reaction [88]. The solid potassium carbonate sorbent (K_2CO_3) sheets developed at IIT by Gidaspow and Onischak [10, 89] and the sodium carbonate (Na_2CO_3) pellets developed at RTI [90] both have shown high sorption rates. However, RTI throws away the large heat of adsorption, which leads to reduce performance by using the cooling tubes in their sorbers.

Chalermsinsuwan et al. [91] have shown CO_2 removal performance in a circulating fluidized bed. The simulation results show the average gas gives a few degrees change in temperature. This is due to the fact that the density of the particles entering and leaving the bed is about three orders of magnitude larger than that of the flue gas. Consequently, no cooling equipment is required. Moreover, Kongkitisupchai [92] and Kongkitisupchai and Gidaspow [93] have shown that 88% of heat liberated in a riser-sorber can be recovered in a downer-regenerator. However, the limits of equilibrium of CO_2 removal conditions showed that 90% of CO_2 cannot be removed in one-sorber regenerator system [94].

The equilibrium system of Na_2CO_3 to $NaHCO_3$ and K_2CO_3 to $KHCO_3$ is presented in Fig. 5.1. The equilibrium curve shows the pressures of CO_2 and H_2O are directly proportional to the temperature. A small change in temperature will probably affect the adsorption or desorption capacity. For example, if the operation temperature is 65°C, the decomposition pressure for the Na_2CO_3 is 12.2 kPa. At equilibrium the mixture contains 6.1 mole% CO_2. Hence, with 15% inlet CO_2 in the flue gases, less than half of CO_2 can be removed at this temperature. For the K_2CO_3, the equilibrium pressure is 3.3 mole% CO_2. Park et al. [12] used dry regenerable potassium-based sorbents. To remove 90% of CO_2 from the flue gases, a staged fluidized bed design concept, as shown in Fig. 5.2, may be used. Hence, the alternative method to achieve 90% CO_2 removal is used bubbling fluidized beds. Solid sorbents other than Na_2CO_3 or K_2CO_3 are being actively developed to achieve high rates of reactions e.g. Zhang et al. [95] and Petit and Park [96]. The conceptual design and well-mixed model are shown in Appendix A.

In view of this, a modified bubbling bed concept was explored, different from that used at RTI [90]. The design purpose of fluidized beds in this study is to operate a binary mixture of particles without bubbles. CFD model was developed and computed for a binary mixture of particles of an average size of 75 μm, as used by RTI. A reasonably high rate of reaction has an effective rate constant, k=1.0 s^{-1}. As sorption proceeds in the batch reactor, this effective rate constant decreases with time. This theory is reviewed by Gidaspow [97]. Since this decrease is very slow due to the high sorbent capacity, the CFD simulations are repeated for an order of magnitude lower rate of reaction. A reasonable residence time in a sorber is one second. Then, a plug flow model [66] shows the outlet concentration of CO_2 to be as follows,

$$\frac{C_{out}}{C_{in}} = \exp\left[\frac{-kL}{V}\right] \tag{5.1}$$

where L is the expanded bed height of particles with V, the superficial gas velocity of gases. Here, we perform our CFD simulations at a constant temperature. As a first approximation, we included the effect of water vapor on the rate of reaction into the effective rate constant, k. Syamlal and O'Brien [98] performed a similar CFD simulation for ozone decomposition in a bubbling bed and compared their simulations to experiments.

5.2. Computational fluid dynamics (CFD) simulation model

In this CFD simulations were performed in a 1.2 m reactor height and 0.25 m for width as shown in Fig. 5.3. Table 5.1 shows the description of the input data for fine and coarse grid simulations. The simulation of a fluidized bed system with a binary mixture of particles without formation of bubbles was already described by Gidaspow and Chaiwang [99] for isothermal fluidization without reaction. In current study, the extents of chemical reactions with heat generations were included. The energy equations are those used by Syamlal and Gidaspow [84]. The computational fluid dynamics which including computational fluid dynamics theories, two computational fluid dynamics approaches, the conservation and constitutive equations for Eulerian-Eulerian approach including the system details are shown in following section.

Computational fluid dynamics (CFD) is a useful analysis tool which uses mathematical and numerical methods to solve problems by means of computer-based simulation, such as fluid flow, chemical reactions, heat transfer and other associated phenomena. Computational fluid dynamics show the virtual visualization and behavior of the apparatus or unit design which is difficult to measure through experimental. It also predicts the design performance under at the various operating conditions, even though there are no any experiments. This technique is widely used for industrial and non-industrial applications due to its many advantages. First, it is cost-saving and it helps the design to meet environmental regulations and industrial standards. Many examples are succeeding using computational fluid dynamics to improve the performance of a design in real world industries [100-103].

Fluidization or multiphase flow system is one of the most processes which are suitable for computational fluid dynamics. The Navier-Stokes equations are used for the hydrodynamics model. Two different computational fluid dynamics modeling approache are consisting of Lagrangian and Eulerian approaches. The calculation of motion and path of each solid particle are calculated with the Lagrangian approach. Consequently, the large memory resource and the long calculation time are required, which are drawbacks for the Lagrangian approach. While the Eulerian approach treats the solid particle as a continuum phase and the averages out motion on the scale of individual solid particles. There are no large memory resources and computing power requirement in this approach. Therefore, the Eulerian approach enables users to simulate the system domains at realistic dimensions within the reasonable time frames. It can be seen, the Eulerian approach is the appropriate approach for performing fluidization or multiphase flow studies [46, 104-107] .

5.2.1 Approaches for multiphase computational fluid dynamics modeling

Advances in the study of computational fluid dynamic have provided the basis for further insight into the dynamics of multiphase flows. There are generally two main approaches for modelling multiphase computational fluid dynamics which compose of Eulerian- Eulerian and Eulerian-Lagrangian approaches [108].

5.2.1.1 The Eulerian-Lagrangian or Lagrangian approach

The Eulerian-Lagrangian, also called Lagrangian approach, implies the combination in term of the continuous fluid flow which can be described with Eulerian framework while the disperse of solid particles phase behavior is used a Lagrangian framework. A continuous gas phase can be solved by the time-average Navier-Stokes equations. In the meantime, based on mathematical model formulation for each phase of the solid particle (called parcel) is considered as a disperse phase, interacting gas and possessing in a large number through fluid flow with the same properties representing the concentration of disperse phase is solved by Newtonian equations. In the principle of Lagrangian approach, when the solid particles concentration is increased, the particle-particle collision becomes important. The interactions between solid particles in multiphase flow are detected and calculated in order to track through the flow field simultaneously. There is the exchange of momentum, mass and energy with the fluid phase. The collision of the solid particles can be provided by collision laws. Two models are generally used, the hard sphere and the soft sphere models [109]. In the hard sphere model, the collisions of particle interactions are taken into account for non-spherical particles by means of the empirical coefficient of restitution and friction coefficient, Coulomb friction and tangential restitution [110, 111]. On the other hand, in the soft sphere model, the collisions between particle-particle and between particles-wall processes is solved by numerical integration of the motion using Hooke's linear spring, dash pot and friction slider [112, 113]. Even though the soft sphere model uses the computation time longer than the hard sphere model, it is more applicable than hard sphere model.

In order to determine the average behavior of the Lagrangian system, increasing computational powers and capacities are mostly required for calculating a large number of solid particle trajectories. The drawbacks of this approach are due to the prerequisite of the large memory capacity requirement and the long computational time [58].

Therefore, the Lagrangian approach is suitable for simulating dilute systems [114, 115] which contained a low solid volume fraction (<12%) of solid particles. This model are used to follow the particle along its trajectory when the solid particles characteristics, such as composition, size and/or shape, are varying with time owing to mechanical effects and chemical reaction. So, this model seems appropriate for focusing on small groups of particles applications such as spray dryer, droplet and particle-laden (discrete solid particles in a gas phase) flows, but inappropriate for any applications with large groups of particles, such as fluidized bed, or any applications where volume fraction of the discrete phase is considering. Nonetheless, there are some literatures studies using this model for fluidization application. The interparticle force effect [116, 117], mixing and segregation characteristics [118, 119] and particle residence time [120] on fluidization have been investigated. This Eulerian-Lagrangian approach can be found in Deen et al. (2007) [121] for more details.

5.2.1.2 The Eulerian- Eulerian or Eulerian approach.

In the Eulerian-Eulerian or Eulerian approach describes the dispersed or solid particle phase as the continuous fluid interpenetrating and interacting with gas or fluid phase by generalizing the Navier-Stokes equations. Phase coupling between the fluid and the particulate phases is take place through the pressure and interphase exchange properties, including momentum, heat and mass transfer. Furthermore, the Eulerian approach requires specific closures laws to explain the solid particles rheology for representing the continuum of the interfacial forces and turbulence of the solid particle phase. At present, the constitutive equations are generally used the viscosity and the kinetic theory of granular flow approaches for the solid particles. The expressions for solid viscosity gives the closure based on empirical correlations and experimental values, accounting for solid stress modulus, solid pressure and solid viscosity [122, 123]. In contrast, the kinetic theory of granular flow computed at the explicit closures that specify the energy dissipation due to the inelastic collisions of solid particles (non-ideal particle-particle collisions) into account by means of the restitution coefficients [46, 124].

The Eulerian approach should be widely applicable for modeling a multiphase flow process which contained a large solid volume fraction of the dispersed phase (gas-solid dense flow character). In the disperse flow, the solid particles can be treated as a continuous phase. Due to the relatively small memory capacity requirement and the short computational time comparing with the Lagrangian approach, this approach is suitable to fluidized bed or other particle suspension columns applications. In order to measure volume fractions of each phase, the physical volume fraction is proposed. An assumption of the particles and fluid pass by are identified as continuous functions of space and time. Since the volume fraction concept is applied because each phase cannot occupy together. The volume fraction concepts of each phase have been developed with the conventional conservation equations [107]. There are several studies using Eulerian approach model for fluidization application [101, 104, 124, 125].

5.2.2 The Eulerian model

The governing equations for the Eulerian-Eulerian approach consist of mass, momentum, energy, and species equations, well-known as conservation equations. The multiphase flow system which excluded the chemical reaction and/or heat transfer in the system is called cold flow model. Only mass and momentum equations are calculated for the cold flow model. In terms of the hot flow model, the system requires the energy and specie equations as a part of conservation equations. The conservation equations are based on the consideration of the quantity of each state variable flowing in and out, and generated in the considered region. If the multiphase flow has more than one dispersed or solid particle in the system, each dispersed or solid particle is defined as a phase separately and require its own equations. To solve the gas and solid particle properties in the conservation equations, the constitutive equations are coupling. The conservation and constitutive equations of each phase simulated in this study are discussed in this chapter. For more details about the conservation and constitutive equations, the multiphase flow text book written by Gidaspow (1994) [107] can be used as one of the references.

5.2.2.1 Conservation equations

In this study, the two-dimensional Cartesian coordinate (x- and y- directions) systems are operated with one gas and one solid particle phase.

- The mass conservation equations (continuity equations)

The accumulation of mass in each phase of the continuity equations is balanced by the convective mass fluxes. Assuming that there are no mass exchanges between the phases such as the reaction, absorption, sublimation or vaporization.

For gas phase:

$$\frac{\partial}{\partial t}\left(\varepsilon_g \rho_g\right)+\nabla\cdot\left(\varepsilon_g \rho_g v_g\right)=0 \tag{5.2}$$

For solid particle phase:

$$\frac{\partial}{\partial t}\left(\varepsilon_s \rho_s\right)+\nabla\cdot\left(\varepsilon_s \rho_s v_s\right)=0 \tag{5.3}$$

where ρ_g is the density of the gas phase (kg/m^3), ρ_s is the density of the solid particle phase (kg/m^3), ε_g is the volume fraction of the gas phase (-), ε_s is the volume fraction of the solid particle phase (-), v_g is the velocity of the gas phase (m/s), v_s is the velocity of the solid particle phase (m/s) and t is the time (s).

- The momentum conservation equations

The accumulation of momentum in each phase is balanced by the convective momentum fluxes and the forces exerted inside the system, which are the forces due to gravity, stress tensor, pressure and momentum interphase exchange coefficient.

For gas phase:

$$\frac{\partial}{\partial t}\left(\varepsilon_g \rho_g v_g\right)+\nabla\cdot\left(\varepsilon_g \rho_g v_g v_g\right)=-\varepsilon_g\nabla P+\nabla\cdot\tau_g+\varepsilon_g\rho_g g-\beta_{gs}\left(v_g-v_s\right) \tag{5.4}$$

For solid particle phase:

$$\frac{\partial}{\partial t}(\varepsilon_s \rho_s v_s)+\nabla\cdot(\varepsilon_s \rho_s v_s v_s)=-\varepsilon_s \nabla P+\nabla\cdot\tau_s-\nabla P_s+\varepsilon_s \rho_s g+\beta_{gs}(v_g-v_s) \tag{5.5}$$

where P is the pressure of the gas phase (Pa), P_s is the pressure of the solid particle phase (Pa), τ_g is the stress tensor of the gas phase (N/m^2), τ_s is the stress tensor of the solid particle phase (N/m^2), g is the gravity forces (m/s^2) and β_{gs} is the momentum interphase exchange coefficient between gas and solid phase (kg/m^3 s), other symbols use in momentum equations have the same definition as in mass conservation equations.

- The energy conservation equations

To describe the energy conservation equations, a separate enthalpy equation can be written for each phase. The accumulation of energy in each phase is balanced by the convective energy fluxes, the work due to pressure or volume changes, the heat source due to viscous dissipation (stress) and conduction and the intensity of heat exchange between the phases.

For gas phase:

$$\frac{\partial}{\partial t}(\varepsilon_g \rho_g h_g)+\nabla\cdot(\varepsilon_g \rho_g v_g h_g)=-\varepsilon_g \frac{\partial P}{\partial t}+\tau_g:\nabla\cdot v_g+q_g-Q_{sg} \tag{5.6}$$

with $h_g=\int c_{p,g}\,dT_g$

For solid particle phase:

$$\frac{\partial}{\partial t}(\varepsilon_s \rho_s h_s)+\nabla\cdot(\varepsilon_s \rho_s v_s h_s)=-\varepsilon_s \frac{\partial p_s}{\partial t}+\tau_s:\nabla\cdot v_s+q_s+Q_{sg} \tag{5.7}$$

with $h_s=\int c_{p,s}\,dT_s$

where q_g is the heat conduction flux of the gas phase (W/m^2), q_s is the heat conduction flux of the solid particle phase (W/m^2) and Q_{sg} is the intensity of heat exchange between the phases (W/m^3), h_g is the specific enthalpy of the gas phase (J/kg), h_s is the specific enthalpy of the solid particle phase (J/kg), $c_{p,g}$ is the heat capacity of the gas phase (J/kg

K), $c_{p,s}$ s the heat capacity of the solid particle phase (J/kg K), T_g is the temperature of the gas phase (K), T_s is the temperature of the solid particle phase (K).

- The species conservation equations

Depending on the role of the solid particles, the multiphase flow with chemical reaction can be divided into two main categories. The solid particles can be considered either catalyst (medium) or reactant. In this study, the solid particles are part of chemical reaction. The species conservation equations for gas phase and solid phase are then used and shown as followed. The mass accumulation of i species is balanced by the convective mass fluxes of i species, the diffusive mass fluxes of i species and the homogeneous and/or heterogeneous chemical reactions of i species inside the system.

For gas phase:

$$\frac{\partial}{\partial t}\left(\varepsilon_g \rho_g y_{i,g}\right) + \nabla \cdot \left(\varepsilon_g \rho_g v_g y_{i,g}\right) = \nabla \cdot \varepsilon_g J_{i,g} + r_{i,g} + \varepsilon_g R_{i,g} \tag{5.8}$$

For solid particle phase:

$$\frac{\partial}{\partial t}\left(\varepsilon_s \rho_s y_{i.s}\right) + \nabla \cdot \left(\varepsilon_s \rho_s v_s y_{i,s}\right) = \nabla \cdot \varepsilon_s J_{i,s} + r_{i,s} + \varepsilon_s R_{i,s} \tag{5.9}$$

where $y_{i,g}$ is the mass fraction of i specie in the gas phase (-), $y_{i,s}$ is the mass fraction of i specie in the solid particle phase (-), $J_{i,g}$ is the diffusive mass fluxes of i specie in the gas phase (can be substituted by Fick's first law) (kg/m^2 s), $J_{i,s}$ is the diffusive mass fluxes of i specie in the solid particle phase (kg/m^2 s), $r_{i,g}$ is the net heterogeneous reaction rate of i species in the gas phase (kg/m^3 s), $r_{i,s}$ is the net heterogeneous reaction rate of i species in the solid particle phase (kg/m^3 s), $R_{i,g}$ is the net homogeneous reaction rate of i species in the gas phase (kg/m^3 s), and $R_{i,s}$ is the net homogeneous reaction rate of i specie in the solid particle phase (kg/m^3 s). If the solid particle is considered to be the catalyst (medium) in the system, only the species conservation equations for gas phase is required.

5.2.2.2 Constitutive equations

This section summarizes the general constitutive equations and the specific constitutive equations of solid particle phase properties. The kinetic theory of granular flow model concept is widely used as the constitutive equations.

- The volume fractions

In this study, the concept of volume fraction in the physical system is applied as a continuous function of space and time on this multiphase flow system. A space of each phase can only occupy at a time. Therefore, the summation of the volume fractions for all the phases must be equal to one.

$$\varepsilon_g + \varepsilon_s = 1 \tag{5.10}$$

- The stress tensors

The stress is a measure of the average amount of force exerted per unit surface area within a deformable body on, which internal forces act. One may view the stress as a measure of the intensity of the total internal forces acting within a deformable body. The stress tensors of gas and solid particle phases can be represented as:

For gas phase:

$$\tau_g = \varepsilon_g \mu_g \left[\nabla v_g + \left(\nabla v_g \right)^T \right] - \frac{2}{3} \varepsilon_g \mu_g \left(\nabla \cdot v_g \right) I \tag{5.11}$$

For solid particle phase:

$$\tau_s = \varepsilon_s \mu_s \left[\nabla v_s + \left(\nabla v_s \right)^T \right] - \varepsilon_s \left(\xi_s - \frac{2}{3} \mu_s \right) \nabla \cdot v_s I \tag{5.12}$$

where μ_g is the viscosity of the gas phase (kg/m s), μ_s is the shear viscosity of the solid particle phase (kg/m s), ξ_s is the bulk viscosity of the solid particle phase and I is the unit tensor. In the following chapters, these general stress tensors have been proved to be used for fluidized bed riser and downer simulations.

- The momentum interphase exchange coefficients

Gidaspow [107] is the first to propose classical momentum interphase coefficient or known as Gidaspow model. The coefficient consists of a combination of the Ergun equation and the Wen and Yu model. This model is used for dense gas-solid fluidized beds for any simulation done by using FLUENT software appropriately [126]. The Gidaspow model depends on gas volume fractions, if the gas volume fractions equal or less than 0.8. The model follows Ergun equation. The model changes to Wen and Yu model for gas volume fractions above than 0.8. Therefore, in this study, the Gidaspow model is used to predict the hydrodynamics.

For $\varepsilon_g \leq 0.8$:

$$\beta_{gs} = 150\frac{(1-\varepsilon_g)^2 \mu_g}{\varepsilon_g d_p^2} + 1.75\frac{(1-\varepsilon_g)\rho_g |v_g - v_s|}{d_p} \tag{5.13}$$

For $\varepsilon_g > 0.8$:

$$\beta_{gs} = \frac{3}{4}\frac{(1-\varepsilon_g)\varepsilon_g}{d_p}\rho_g |v_g - v_s| C_{D0}\varepsilon_g^{-2.65} \tag{5.14}$$

with Re<1000; where $C_{D0} = \frac{24}{\mathrm{Re}_k}\left(1 + 0.15\,\mathrm{Re}_k^{0.687}\right)$

with Re≥1000; $C_{D0} = 0.44$

where C_{D0} is the drag function.

- The heat conduction fluxes (in the same phase)

The heat conduction is the transfer of thermal energy between adjacent molecules in a same substance due to a temperature gradient. By using Fourier’s law, the heat conduction fluxes of gas and solid particle phases can be written as following.

For gas phase:

$$q_s = -\varepsilon_g k_g \nabla T_g \tag{5.15}$$

For solid particle phase:

$$q_s = -\varepsilon_s k_s \nabla T_s \tag{5.16}$$

where k_g is the thermal conductivity of the gas phase and k_s is the thermal conductivity of the solid particle phase.

- The heat exchange between the phases

The heat exchange between the phases, so called heat convection, is the transfer of thermal energy between a solid particle and the nearby motion gas. This can be converted with heat conduction, which is the transfer of energy by vibrations at a molecular level. A widely used model for the heat exchange between the phases known is Gunn model [127]

$$Q_{sg} = h_{sg}\left(T_s - T_g\right) \tag{5.17}$$

with $h_{sg} = \dfrac{6k_g \varepsilon_s \varepsilon_g Nu_s}{d_p^2}$ and from Gunn's correlation;

where h_{sg} is the heat transfer coefficient between the phases.

- The kinetic theory of granular flow model concept

The kinetic theory of granular flow is the model for the constitutive equations of the solid particle properties. The basic concept of kinetic theory of granular flow originates from the granular temperature which measured the motion of particles by oscillating randomly. This kinetic theory of granular flow model applied from the thermal temperature in the kinetic theory of gases to gas-solid multiphase flow approach proposed by Chapman and Cowling [128]. Later, Jenkins and Savage [129] developed the application of kinetic theory methods providing the restitution coefficient to exhibit the inelastic collisions between particles. This model was accordingly continued by Lun et al. (1984) [130]. The models based on kinetic theory of granular flow can be able to compute solid viscosity for particulate phase and solid shear stress term which become an optional over viscosity model. By calculating solid fluctuating kinetic energy equation (granular temperature equation) as described in the following section.

Consequently, the kinetic theory of granular flow model is applied as constitutive equation in this study since this model do not required the empirical correlations comparing with the conventional viscous model.

- The solid fluctuating kinetic energy or granular temperature

The granular temperature for the solid particle phase is proportional to the fluctuating kinetic energy equation of the random motion of the solid particles. The solid fluctuating kinetic energy transport equation derived from the kinetic theory of granular flow model is shown below.

$$\frac{3}{2}\left[\frac{\partial}{\partial t}(\varepsilon_s\rho_s\theta)+\nabla\cdot(\varepsilon_s\rho_s\theta)v_s\right]=\left(-\nabla p_s\bar{I}+\tau_s\right):\nabla v_s+\nabla\cdot(\kappa_s\nabla\theta)-\gamma_s+\phi_s \qquad (5.18)$$

where θ is the solid fluctuating kinetic energy or granular temperature (m^2/s^2), κ_s is the conductivity of solid fluctuating kinetic energy (kg/m s), γ_s is the collision dissipation of solid fluctuating kinetic energy (kg/m s^3) and ϕ_s is the exchange of solid fluctuating kinetic energy between phases. The two terms of the left hand side are the accumulation term and convection term of the granular temperature, respectively. The first term of right hand side is the production of fluctuating energy by the pressure and shear stresses, the second term is the conduction due to the gradient of granular temperature, the third term is the dissipation due to the inelastic collision of particles, the fourth term is the solid fluctuation kinetic energy exchange between phases.

- The solid shear viscosity

The solid shear viscosity is calculated from a kinetic and a collisional term arising from particle momentum exchange due to collision and translation.

$$\mu_s=\frac{4}{5}\varepsilon_s\rho_s d_p g_0(1+e)\sqrt{\frac{\theta}{\pi}}+\frac{10\rho_s d_p\sqrt{\pi\theta}}{96(1+e)g_0\varepsilon_s}\left[1+\frac{4}{5}g_0\varepsilon_s(1+e)\right]^2 \qquad (5.19)$$

- The solid bulk viscosity

The solid bulk viscosity represents the resistance of the granular solid particles to compression and expansion.

$$\xi_s = \frac{4}{3}\varepsilon_s \rho_s d_p g_0 (1+e)\sqrt{\frac{\theta}{\pi}} \tag{5.20}$$

- The radial distribution function

The radial distribution function is a correction factor that modifies the probability of collisions between solid particles when the solid particles volume fraction is in the dense regions.

$$g_0 = \left[1-\left(\frac{\varepsilon_s}{\varepsilon_{s,\max}}\right)^{1/3}\right]^{-1} \tag{5.21}$$

where is the volume fraction of the solid particle phase at maximum packing. Usually, is approximately 0.63.

- The solid pressure

The solid pressure is composed of a kinetic term that dominates in the dilute regions and a second term due to particle collisions that is significant in the dense regions:

$$p_s = \varepsilon_s \rho_s \theta \left[1 + 2 g_0 \varepsilon_s (1+e)\right] \tag{5.22}$$

where g_0 is the radial distribution function and e is the particle-particle restitution coefficient.

- The conductivity of solid fluctuating kinetic energy

The conductivity of solid fluctuating kinetic energy describes the diffusion of granular energy:

$$\kappa_s = \frac{150 \rho_s d_p \sqrt{\theta\pi}}{384(1+e)g_0}\left[1+\frac{6}{5}\varepsilon_s g_0 (1+e)\right]^2 + 2\rho_s \varepsilon_s^2 d_p (1+e) g_0 \sqrt{\frac{\theta}{\pi}} \tag{5.23}$$

- The collisional dissipation of solid fluctuating kinetic energy

The collisional dissipation of solid fluctuating kinetic energy represents the rate of energy dissipation within the solid particle phase due to collisions between solid particles:

$$\gamma_s = 3\left(1-e^2\right)\varepsilon_s^2 \rho_s g_0 \theta \left(\frac{4}{d_p}\sqrt{\frac{\theta}{\pi}}\right) \tag{5.24}$$

- The exchange of solid fluctuating kinetic energy between phases

The transfer of solid fluctuating kinetic energy from the solid particle phase to gas phase is defined by:

$$\phi_s = -3\beta_{gs}\theta \tag{5.25}$$

The advancement in the computational fluid dynamics (CFD) field in the past ten years has been prodigious. With a promising future for the computational fluid dynamics, it is anticipated that CFD will make valuable contributions to predicting the performance of multiphase flow system such as fluidized bed riser or downer. Nevertheless, there are no universal computational fluid dynamics models available, which work in wide-range on multiphase flow application. Therefore, one should pay close attention on the current and previous studies on computational fluid dynamics model to ensure that the most appropriate model is selected for the simulation.

5.3. Results and discussion

5.3.1 Grid Independence

To establish grid independence test, the reactor was repeated for a coarser and finer grids. The total number of grids used in radial and axial direction was shown in Table 5.2. In the vertical direction, the grids spacing are doubled. The result of the coarse grid simulation was shown in Fig. 5.4. The initial behavior of 100 μm particles in a binary mixture with reaction was compared at 0.2 and 0.5 s, respectively. It can be seen that, the bubble sizes and shapes for a coarser grid show no difference corresponding to bubbles in a finer grid. According to the results, the fine grid will applied in this simulation.

5.3.2 75 μm fast reaction rate simulations (k=1 s^{-1}) .

The CFD simulations were performed in a 1.2 m reactor height. The bed was initially filled with an equal weight mixture of Geldart A particle 50 and 100 μm and Geldart B 250 and 500 μm particles for 0.7 m. A conical shape inlet of the reactor promoting spouted type flow will be applied in this study. Such geometry and a binary particle size distribution should eliminate undesirable bubble formation. Initially, the reactor was filled with N_2 atmosphere. A mixture gas of 0.228 weight fraction of CO_2, 0.0934 of water vapor and 0.678 of N_2 was introduced into the reactor at zero time.

Figs. 5.5 and 5.6 show an initial behavior for 100 and 50 μm particles for the fast rate of reaction at 0, 0.2, 0.5 and 1 s, respectively, in a binary mixture with CO_2 capture reaction. At an initial time, the volume fraction of the mixture consisted of uniformly mixed 58 percent of 100 and 50 μm particles. A nearly spherical bubble has occurred at 0.2 s, then it has split at 0.5 s. This behavior is very similar to bubble formation of single size 877 μm particles in a KRW fluidized bed [131]. At 1 s, the bed expansion has reached the top of the bed. For this Geldart group A mixture, the bed expansion is larger than that for the KRW group B particles, as expected. The phase behavior of a binary mixture is segregated, with smaller particles near the top of the bed and the larger particles forming a dense region in the conical section.

The time-averaged solid volume fraction in Fig.5.7 shows the segregation behavior of a binary mixture. The small size of 50 μm particles is almost evenly distributed throughout the bed, except for the wall region. The larger 100 μm particles are more concentrated in the lower half of the bed. This behavior is consistent with a spouted bed type [132] behavior shown in Fig. 5.8. The axial fluid velocity in Fig. 5.8(a) and solid axial velocity of 50 μm particles velocities in Fig. 5.8(b) show very high velocity in the center, with strong downflow at the walls, similar to spouted beds behavior. Fig. 5.8(c) shows that the particle velocity in the center of the bed oscillates wildly. The maximum frequency of oscillation is 0.179 s^{-1}. This frequency is much lower than the bubble frequency. The maximum granular temperature of these particles is about 0.35 m^2/s^2 in the center of the bed in the high velocity region. The measured granular temperatures at a solid volume fraction of 0.3 lie between 0.05-0.1 m^2/s^2 [38]. This high turbulence in the center prevents the formation of bubbles after start-up of fluidization in the bed.

Fig. 5.9(a)-(d) depict the time-averaged from 2 to 30 s weight fractions of CO_2, H_2O, N_2 and rate of reaction, respectively. It can be seen that, CO_2 and water vapor flow only in the center of the bed due to the strong downflow at the walls, as shown in Fig. 5.9. The wall region contains mostly N_2. Therefore, the rate of reaction in Fig. 5.9(d) takes place only in the center of the bed. The calculation at the outlet CO_2 concentration is 0.086, as shown in Table 5.3. With the negligible decomposition pressure of the carbonate, the conversion of CO_2 is 62.3 percent. Comparison of dimensionless conversion for CO_2 capture in fluidized beds to a plug flow model is shown in Fig. 5.10. CO_2 conversion is only slightly above that predicted by the plug flow model. Note that the used gas velocities in this study are the superficial velocity. The actual velocity of the gases is almost three times the superficial velocity, as shown in Fig. 5.8.

A simulation for a slow rate, with $k = 0.1\ s^{-1}$, was done in a five-meter-high bed. Solid particles filled up three meters. The height was made higher to achieve a high conversion for the slow rate. But with this length to diameter (L/D) ratio of 12, the bed slugs. Hence, when the sorbent activity decreases, simply increasing the inventory of particles is not a solution. This will be the time to regenerate the sorbent.

5.3.3 375 μm, Fast Rate Simulations ($k=1\ s^{-1}$)

. Fig. 5.11 and 5.12 show the initial behavior for 500 and 250 μm particles at 0, 0.2, 0.5 and 1 s, respectively. The bed was initially filled with an equal weight mixture of 250 and 500 μm particles. For the flow characteristics, there is a bubble formation at 0.2 s similarly with 75 μm mixture as shown in Figs. 5.4 and 5.5, respectively. However, the occurred bubble is much smaller than the bubble for the 75 μm mixture. The bubble does not detach itself from the inlet. Instead, Figs. 5.11 and 5.12 showed that there is simply a void at the inlet. The bubble size is smaller due to the fact that the ratio of average velocity to a minimum fluidization velocity is much smaller for the larger particles. Figs. 5.11 and 5.12 also show that the bed expanded at 0.2 s and contracted at 0.5 s. The bed expansion for this Geldart group B particle mixture is smaller than that for the previous group A particle mixture due to the smaller ratio of superficial to minimum fluidization velocity.

The time-averaged segregation is shown in Fig. 5.13. There are larger particles at the bottom of the bed than at the top. But unlike for the 75 μm mixture, there is very little radial segregation. Fig. 5.14 shows the time-average fluid axial velocity, 250 μm solid axial velocity, cm/s, and its time variation in the center of the bed. The fluid velocity, for most of the bed, is nearly uniform for the Geldart B mixture. Unlike the axial velocities in Fig. 5.7 for Geldart A particle, the particle velocity of 250 μm particles shows an up-flow in the center of the bed with down-flow at the walls. In the freeboard, there is strongly down-flow at the center of the bed, with up-flow at the walls. The particles oscillate with a frequency of about 0.07 s^{-1}, obtained from variations shown in Fig. 5.14. The variance of the axial velocity has a peak at the center of the bed at a height of about 0.1 m equal to 0.2 m^2/s^2. This high turbulent intensity prevents the formation of bubbles, as discussed in the turbulence criteria paragraph in Appendix A.

The time-averaged weight fractions of CO_2, H_2O and N_2 are shown in Fig. 5.15. They are more evenly distributed through-out the bed than those for 75 μm mixture. The reaction takes place uniformly through the bottom of the bed. Table 5.3 gives the outlet CO_2 concentration. A comparison to a plug flow solution is shown in Figure 5.9. The results of this oscillating bed give a better CO_2 conversion than the spouted type bed, since in this oscillating bed the reaction has occurred through-out the bed.

The CFD calculations for the low rate constant, k=0.1 s^{-1} are summarized in Table 5.3. A comparison to a plug flow model is given in Fig. 5.10. Again, the CO_2 conversion is better than for the plug flow model.

5.3.4. Thermal Design: Philosophy

For capturing CO_2 in bubbling beds, it is required cooling equipment due to the large heat of reaction of CO_2 and H_2O with the Na_2CO_3 or K_2CO_3 pellets. In the RTI International study (Nelson et al, 2007 and 2008) such cooling tubes were installed into a bubbling bed. Traditionally, such multiphase flow reactors are designed using empirical measured heat transfer coefficients. Fluidized bed heat transfer was reviewed by Grace

[41] and Xavier and Davidson [133]. The measured heat transfer coefficients increase very rapidly when gas velocity increased above the minimum fluidization velocity (u_{mf}) due to particle motion. Then, they decrease slowly with increasing gas velocity due to decreased particle concentration. At a constant gas velocity, the heat transfer coefficients decrease with particle size decreasing due to decreased particle motion at the same gas velocity. Typical high values of wall to bed heat transfer coefficients are the order of 0.5 kW/m^2 K. For boiling, the heat transfer coefficients are of the order of 7 kW/m^2 K for a horizontal wire in water and higher for boiling heat transfer in dilute emulsions [134].

Syamlal and Gidaspow [84] studied to compute wall to bed heat transfer coefficients using multiphase, followed by Kuipers et al. [135]. In both studies, the heat transfer coefficients, h, were computed using an effective bed thermal conductivity, k_e, and essentially a thermal boundary layer thickness, δ_t, as shown below,

$$h = \frac{k_{eff}}{\delta_t} \tag{5.26}$$

In our multiphase CFD code, k_{eff} is an input, given by a semi empirical equation, explained in the paper by Symlal and Gidaspow [84]. Physically, the effective conductivity consists of a laminar type and a turbulent type conductivity. The turbulent conductivity, k_{tur}, is computed by the CFD code automatically due to the turbulent oscillations of the gas and solid temperatures, volume fractions and velocities, as shown below.

$$turbulent\ heat\ \ flux = \rho_k C_{p_k} \varepsilon_k \overline{T'v'} = -k_{tur}\frac{dT}{dx} \tag{5.27}$$

Rather than computing these complicated local averages, the computation of an average heat transfer coefficient for fluidized bed from an overall energy balance, as given by:

$$T_{Bed} - T_W = \frac{\Delta H\left(Y_{CO_2,out} - Y_{CO_2,in}\right)}{Cp} - \frac{\dot{q}}{\dot{w}Cp} \tag{5.28}$$

where ΔH is the heat of the reaction, $\dot{q}$ is the rate of the heat removal and $\dot{w}$ is the mass flow rate of the flue gas.

5.3.5. Heat transfer calculation

Fluidized bed temperatures can be calculated by solving the steady-state energy balance in Eq. (5.28), together with conservation of the species equation if the heat transfer coefficient is known. But in the CFD model, the heat transfer coefficient is not an input into the code. It can be computed using Eq. (5.28) once the CO_2 conversion and the bulk temperature being computed. To make the computations, the initial bed temperature must be estimated. If the initial temperature is too far off from the true bed temperature, the computations become unreasonably long, since the bed temperature changes very slowly due to the large bed mass. In addition, the wall temperature has to be kept high for the energy to be useful for regeneration of the sorbent. Hence, it took many computations to obtain a useful simulation presented below.

This non-isothermal simulation used the energy equation shown in Table 5.1. The wall temperature was kept at 339 K to allow the heat to be useful for regeneration. The inlet temperature was 310 K to prevent the bulk temperature from being too high and the initial bed temperature was 358 K. The computed average volume fractions and the velocities were similar to those shown in Fig. 5.6 and Fig 5.7. The approach of the bed temperature to a steady state is shown in Fig. 5.16. The time-averaged temperature between 20 to 31 seconds is 358 K. Fig. 5.17 shows the horizontal variations of the time-averaged temperature at the center and the top of the bed. At the center of the bed and at the bottom, the temperature in the middle of the bed has a small dip due to the low entrance temperature. However, the temperature in the bed is uniform within about 1°C, except in the thermal boundary layers at the walls. The thermal boundary layers are about 1 cm thick.

Fig. 5.18 shows the computed weight fraction of CO_2 at the very top of the fluidized bed. The simulation results showed CO_2 concentration at the outlet is 0.20. From Table 5.2, the initial CO_2 weight fraction is 0.228. Therefore, CO_2 conversion is only 12.3% at this bed temperature of 358 K due to the high equilibrium vapor pressure of

K_2CO_3. In Eq. (5.28), the heat loss can be expressed in terms of the heat transfer coefficient, h, and the length to width ratio is as follows:

$$\frac{\dot{q}}{\dot{W}C_P} = \frac{2L}{W}\frac{h(T_b - T_w)}{\rho_g v_g C_p} \tag{5.29}$$

In this simulation, $\rho_g v_g C_p$ =1214 W/m^2 K and $\frac{2L}{W}$ = 8.8.

With T_{bed} = 358 K, T_{in} = 310 K and T_{wall} = 339 K, the wall-to-bed heat transfer coefficient, h, is equal to 319 W/m^2 K. This value is close to experimentally measured heat transfer coefficients for bubbling beds [41]. The computed value is sensitive to CO_2 conversion. With full conversion, it will rise to higher than 2000 W/m^2 K.

The thermal diffusivity can be estimated from the standard deviations of temperatures and velocities; see Fig. 5.19 and Fig. 5.20. The standard deviation of temperature in the wall regions is about 0.75 K and that of axial velocity equal to 0.15 m/s. This gives a thermal flux of 175 kW/m^2 from equation (5.27). The temperature gradient from Fig. 5.15 is 4.5x10^3 K/m. This gives a turbulent thermal conductivity of 3.9 W/m K, about four times that of glass. With a thermal boundary thickness of 0.01 m, the heat transfer coefficient is 388 W/m^2 K. This value is close to that computed from an overall energy balance.

Fig. 5.21 shows the effect of lowering wall temperature to 310 K. The steady state bed temperature is again 357 K. The outlet weight fraction of CO_2 is 0.21 at the top of the fluidized bed. However, in the freeboard it decreased to 0.197. Unfortunately, the values in the small freeboard are not accurate due to numerical problems. Using the outlet concentration of CO_2 at the top of the bed, the value of the heat transfer coefficients is again 319 W/m^2 K.

A better way to compute the heat transfer coefficient is to assign a constant heat generation rate, rather than rely on that produced by the reaction. Then, with the known heat transfer coefficient, optimization studies can be performed.

5.3.6. Approximate Design for 90% CO_2 Capture

The decomposition pressures of both Na_2CO_3 and K_2CO_3, as shown in Fig. 5.1, is so high. It implies that it is not possible to remove 90% of CO_2 from flue gases containing 15% CO_2 and water vapor at temperatures above 60°C, as shown by the plug flow solution in Eq. (5.28). For example, at 65°C, the decomposition pressure for the potassium carbonate is 2.6 kPa. Figure 5.9 shows that at $kL/V=1.1$, $C_{out}/C_{in}=0.35$. At this temperature, $C_{out}/C_{in} = 2.6/15 = 0.17$. This gives $C_{out} = 7.8$ kPa. In the second stage at 50°C, $C_{out} = 3.67$ kPa. In the third stage, $C_{out} = 1.35$ kPa yielding a 91% CO_2 capture. The heat at 50°C and 65°C can be used for sorbent regeneration in combination with reduced pressure [92], while the small portion of releasing heat at 20°C is a loss. Additional heat is available for cooling flue gases to 65°C. The height of each column will be one meter for the fast reaction ($k=1.0\ s^{-1}$) with the superficial velocity of the flue gases of 1.0 m/s. Hence, the total height of the absorber columns will be 3.0 m compared with the commercial amine absorber height of about 20 m.

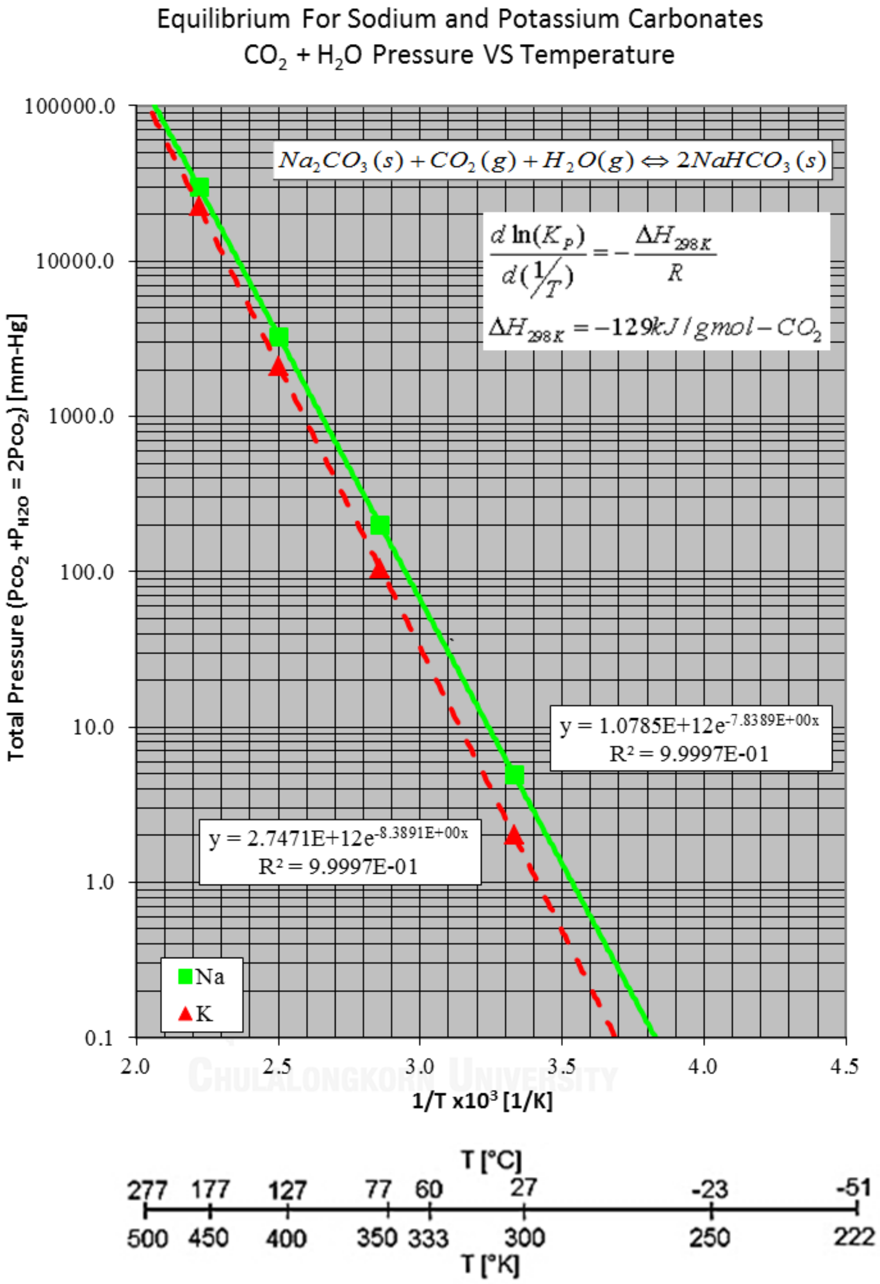

Fig. 5. 1 Equilibrium for Sodium and Potassium Carbonates/Bicarbonate, CO_2+H_2O Pressure vs Temperature [92] .

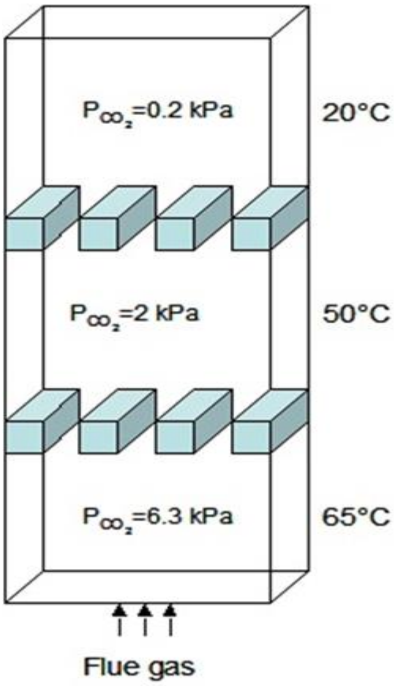

Fig. 5. 2 CO_2 capture design concept.

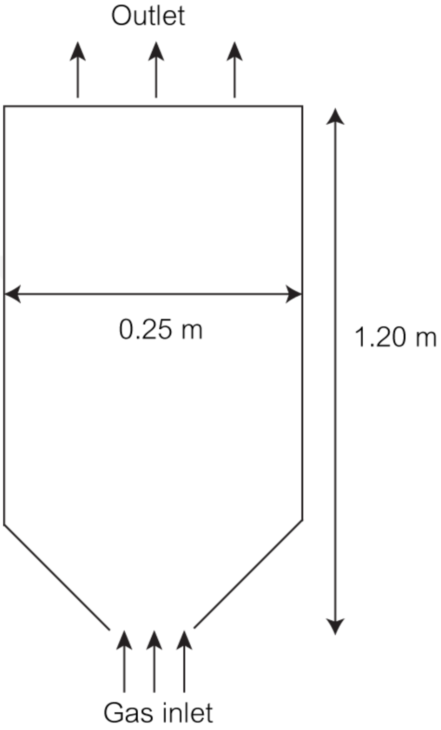

Fig. 5. 3 The schematic drawing of bubbling bed used in this study.

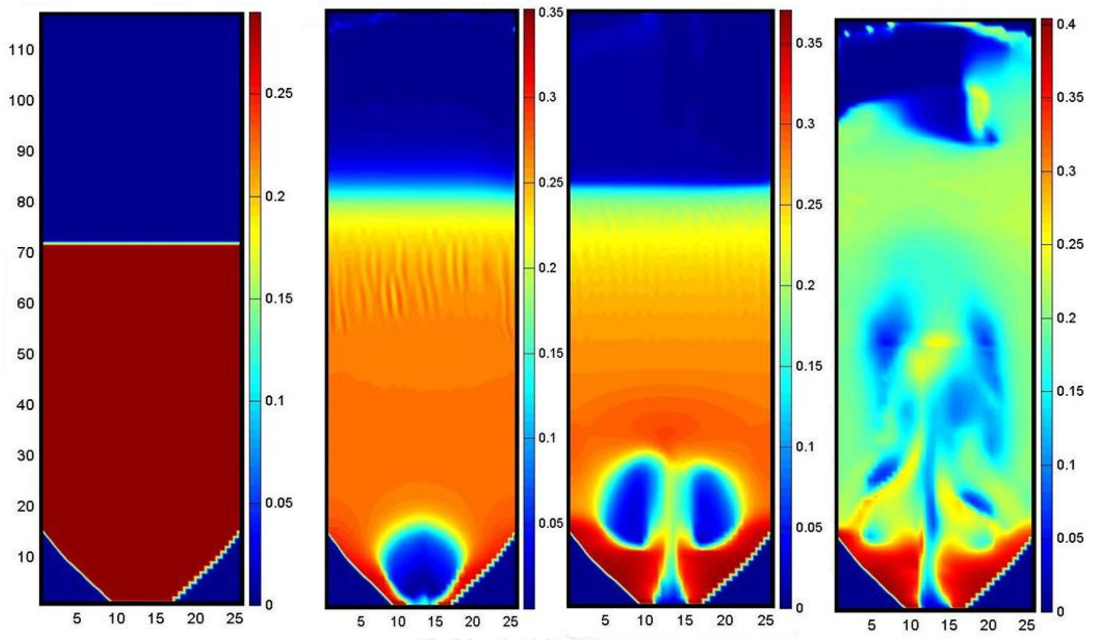

(a) (b)

Fig. 5. 4 The computed instantaneous solid volume fraction at initial behavior of 100 μm particles in a binary mixture with reaction for (a) coarse grid and (b) fine grid simulations.

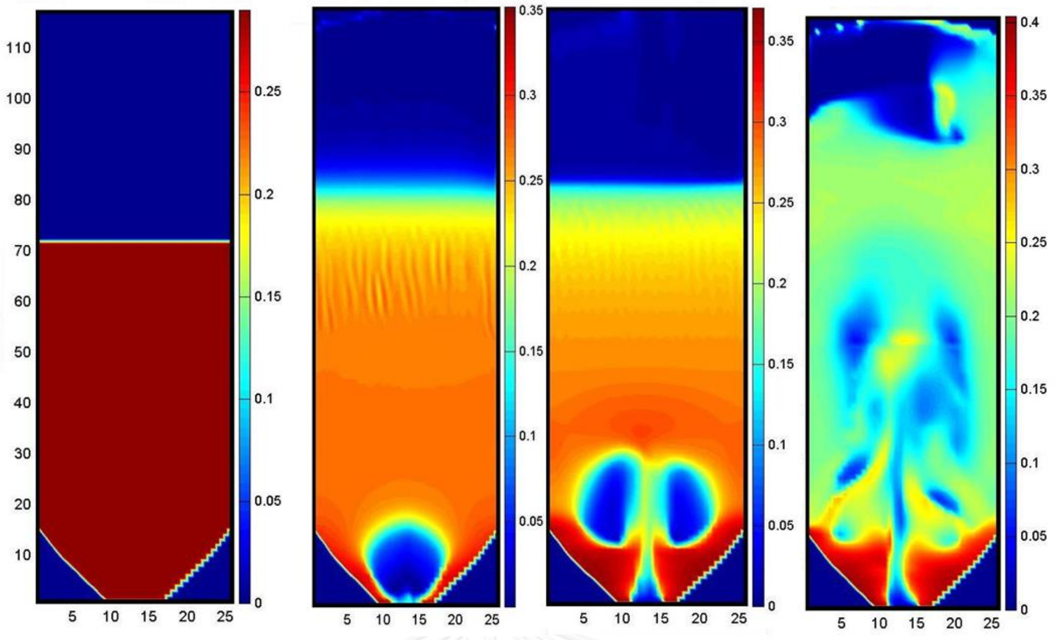

(a) (b) (c) (d)

Fig. 5. 5 Initial behavior for 100 μm particles in a binary mixture with reaction at (a) 0,(b) 0.2, (c) 0.5 and (d) 1 s.

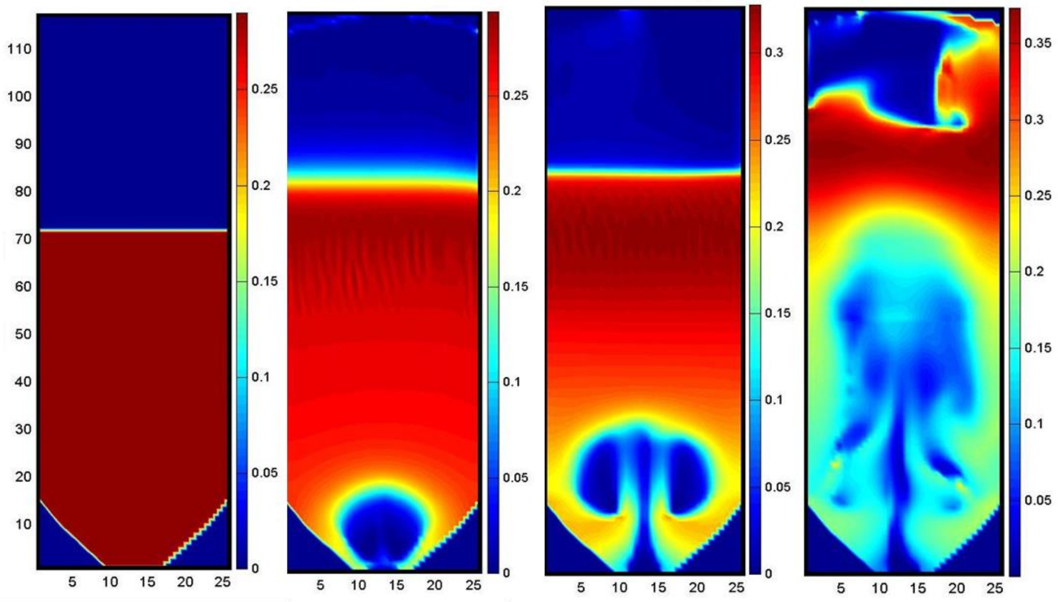

(a) (b) (c) (d)

Fig. 5. 6 Initial behavior for 50 μm particles in a binary mixture with reaction at (a) 0, (b) 0.2, (c) 0.5 and (d) 1 s.

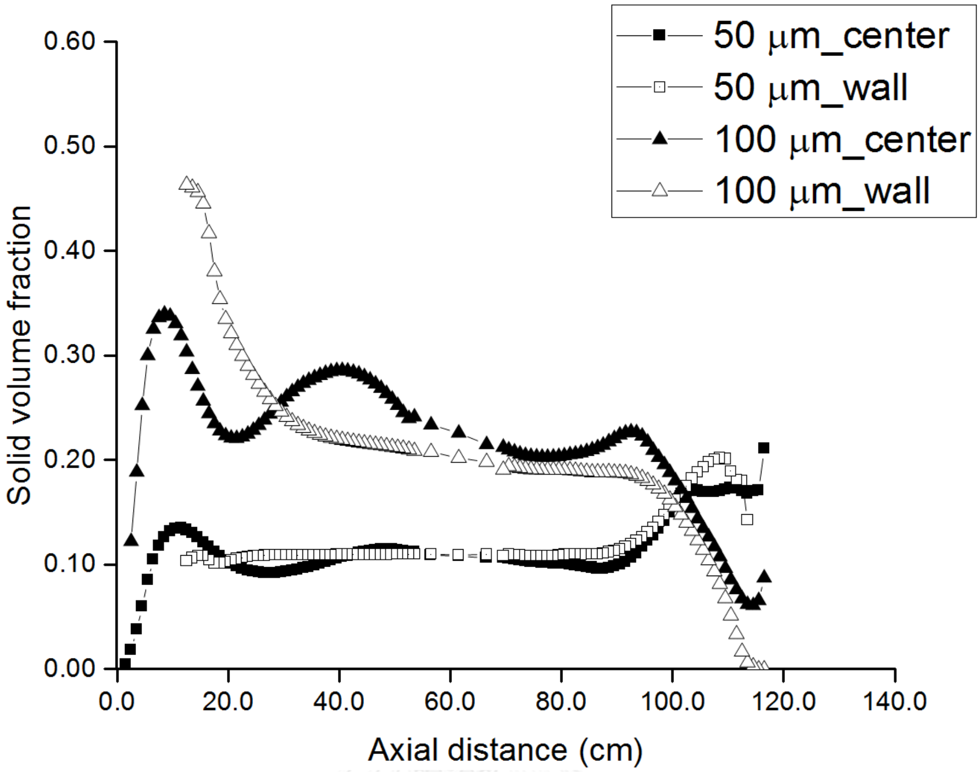

Fig. 5. 7 Volume fractions of 100 and 50 mm particles averaged from 5 to 25 s.

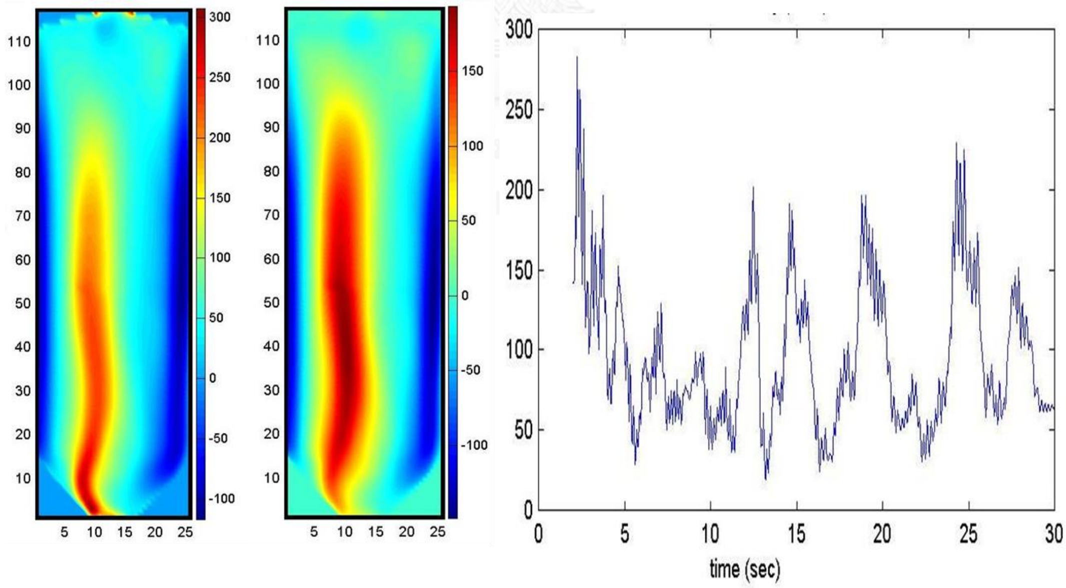

(a) (b) (c)

Fig. 5. 8 Time-averaged of (a) fluid axial velocity, (b) 50 μm solid axial velocity and (c) its time variation in the center of the bed.

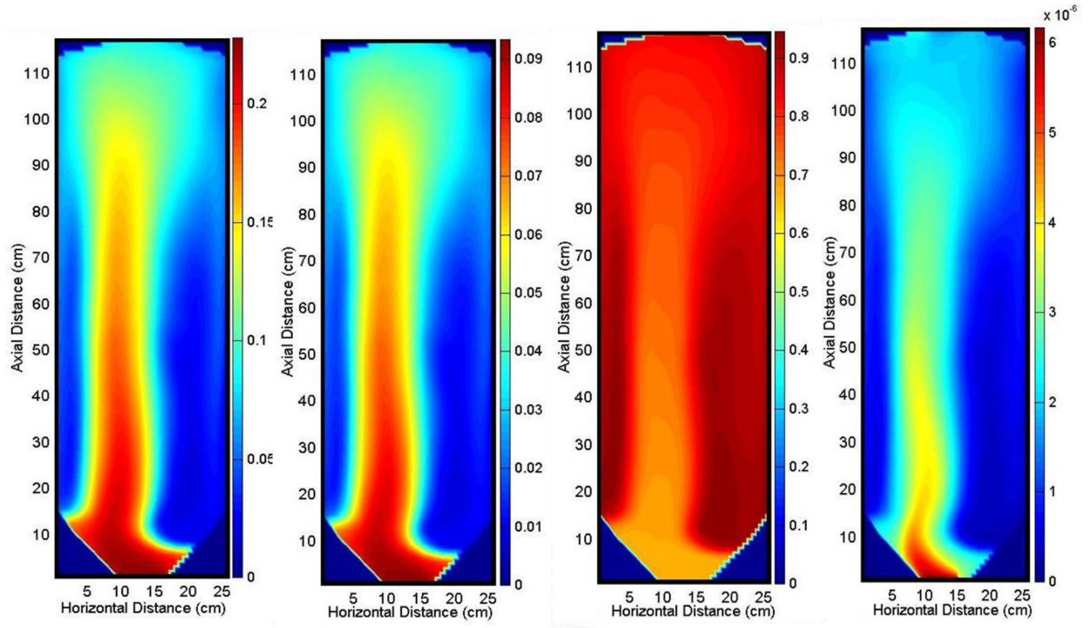

(a) (b) (c) (d)

Fig. 5. 9 Time-averaged weight fractions of (a) CO_2, (b) H_2O ,(c) N_2 and (d) rate of reaction (mole /m^3s)

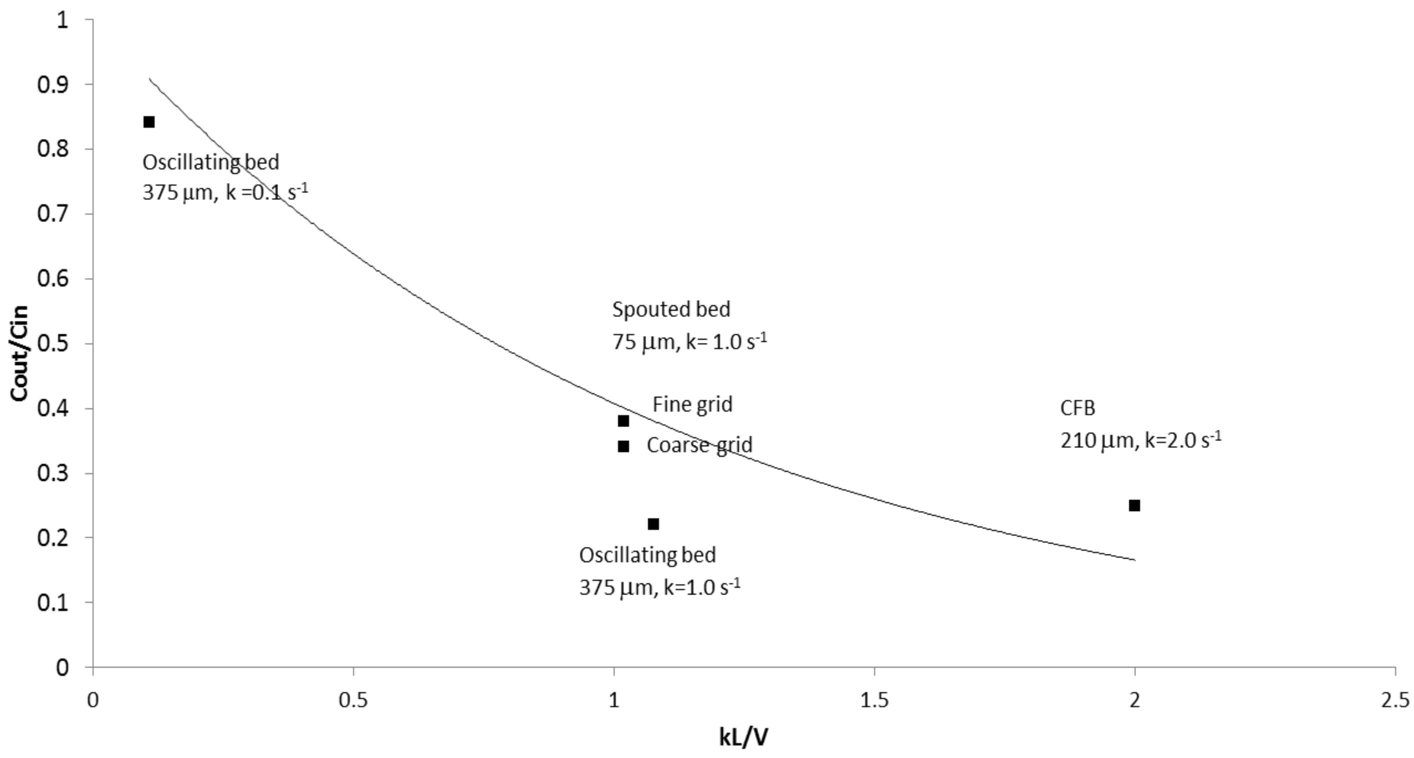

Fig. 5. 10 Comparison of dimensionless conversion for CO_2 capture in fluidized beds to a plug flow reaction model.

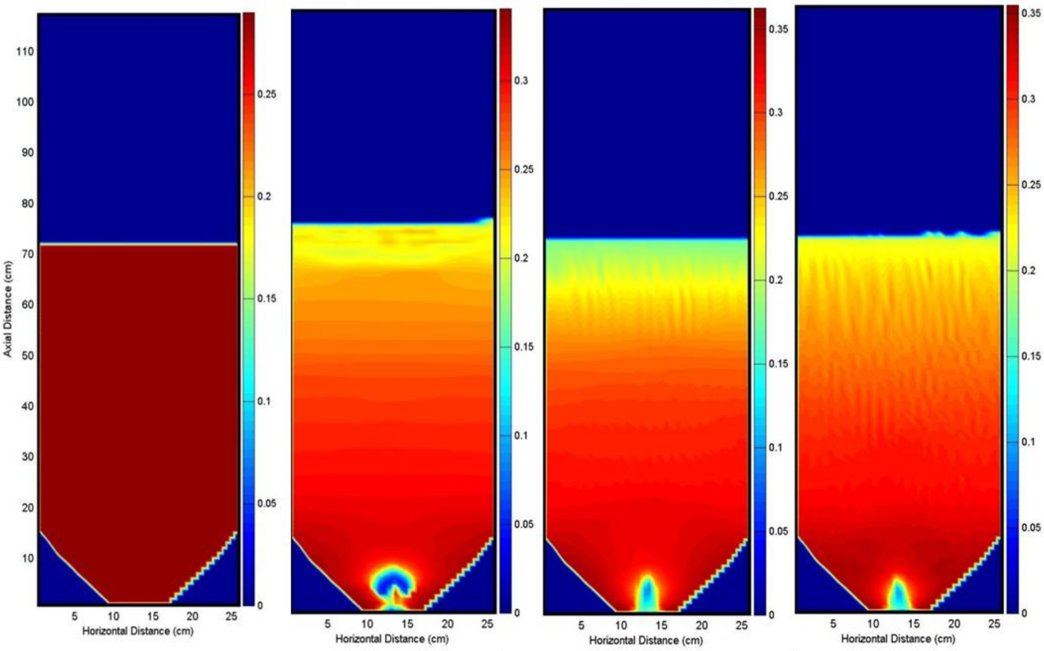

(a) (b) (c) (d)

Fig. 5. 11 Initial behavior for 500 μm particles in a binary mixture with reaction at (a) 0, (b) 0.2, (c) 0.5 and (d) 1 s.

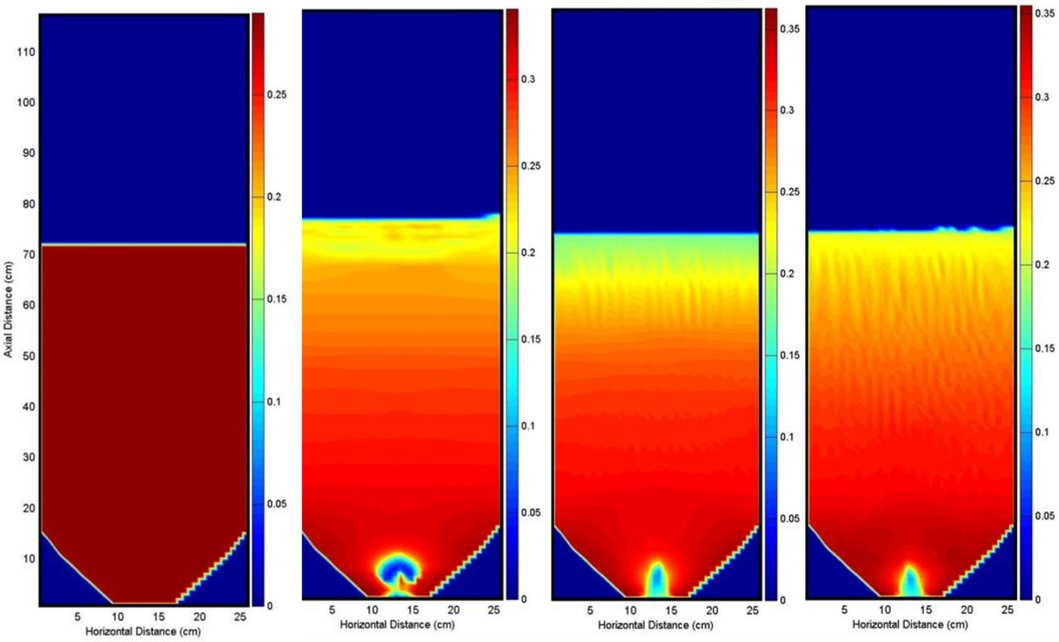

(a) (b) (c) (d)

Fig. 5. 12 Initial behavior for 250 μm particles in a binary mixture with reaction at (a) 0, (b) 0.2, (c)0.5 and (d) 1 s.

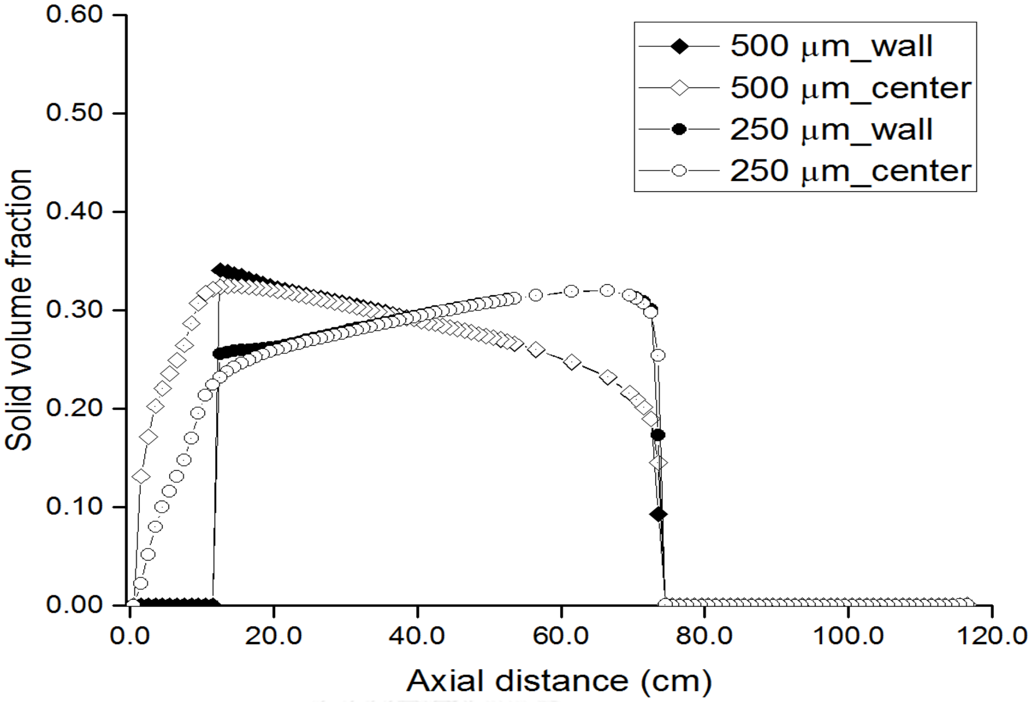

Fig. 5. 13 Volume fractions of 500 and 250 μm particles averaged from 5 to 25 s.

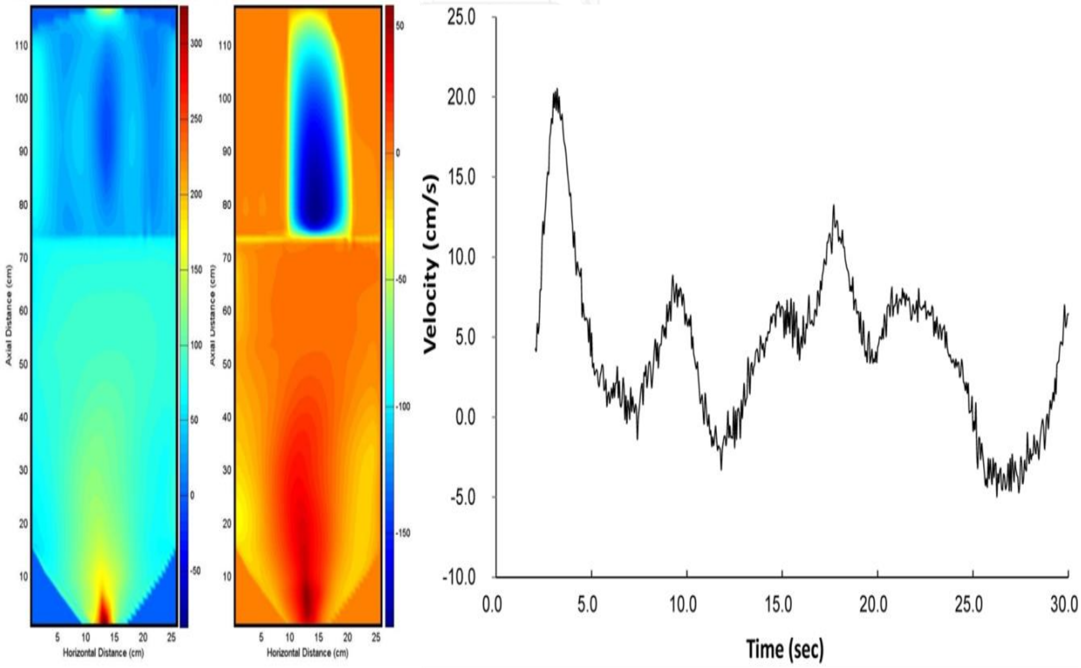

(a) (b) (c)

Fig. 5. 14 Time-averaged of (a) fluid axial velocity, (b) 250 μm solid axial velocity and (c) its time variation in the center of the bed.

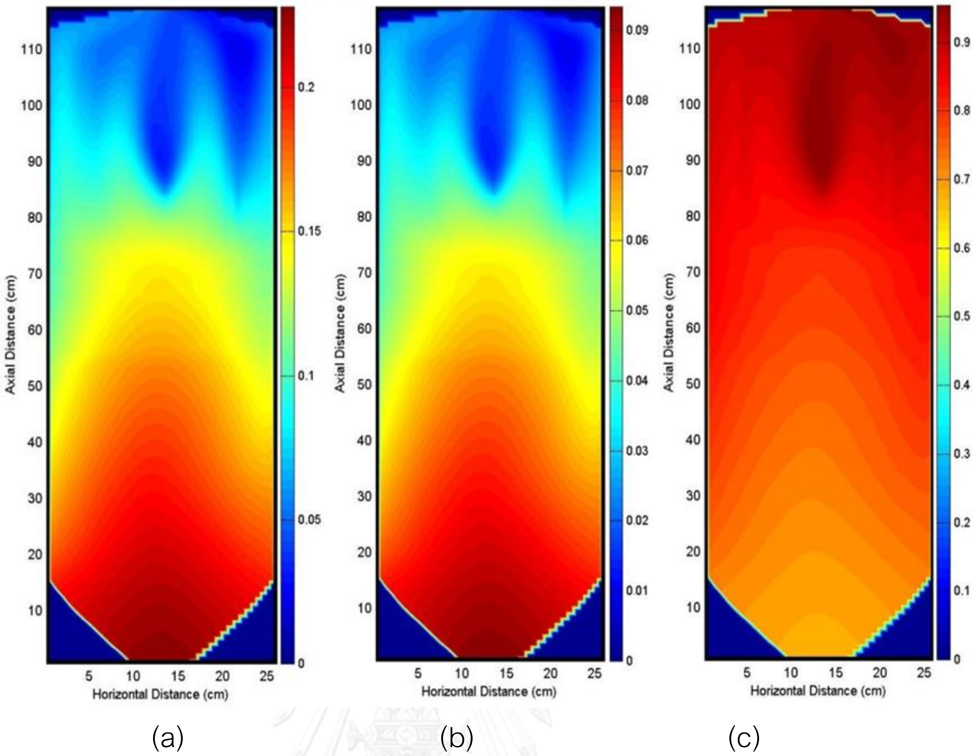

(a) (b) (c)

Fig. 5. 15 Time-averaged weight fractions of (a) CO_2, (b) H_2O, (c) N_2

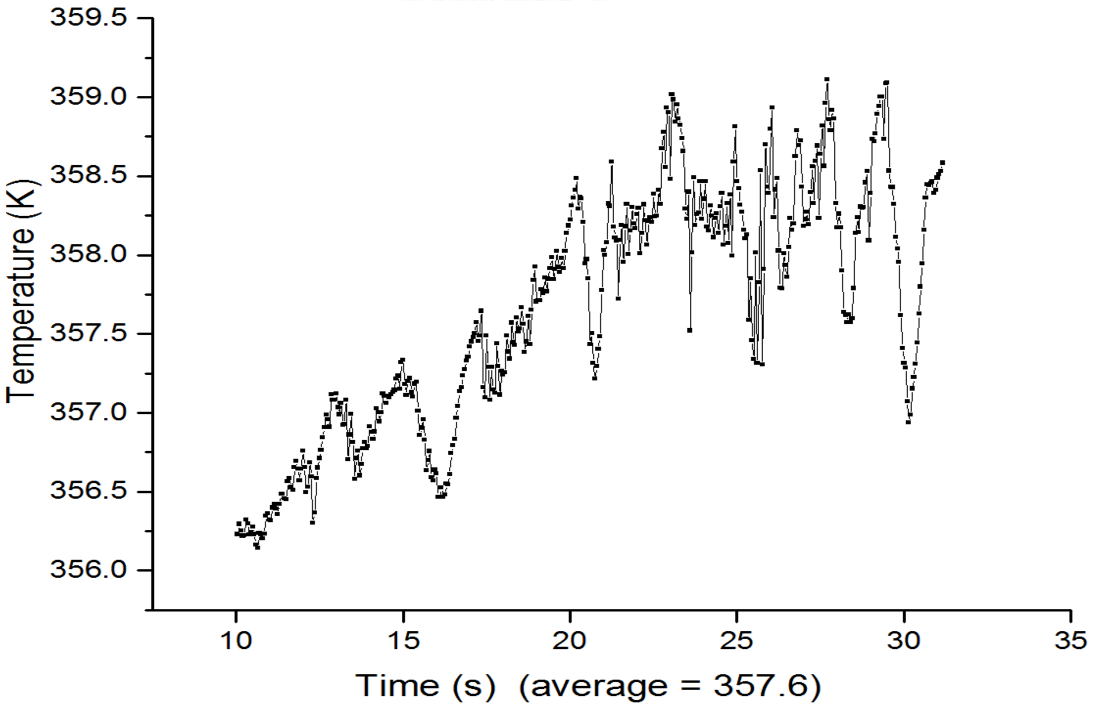

Fig. 5. 16 Approach of bed temperature at the center to a steady state.

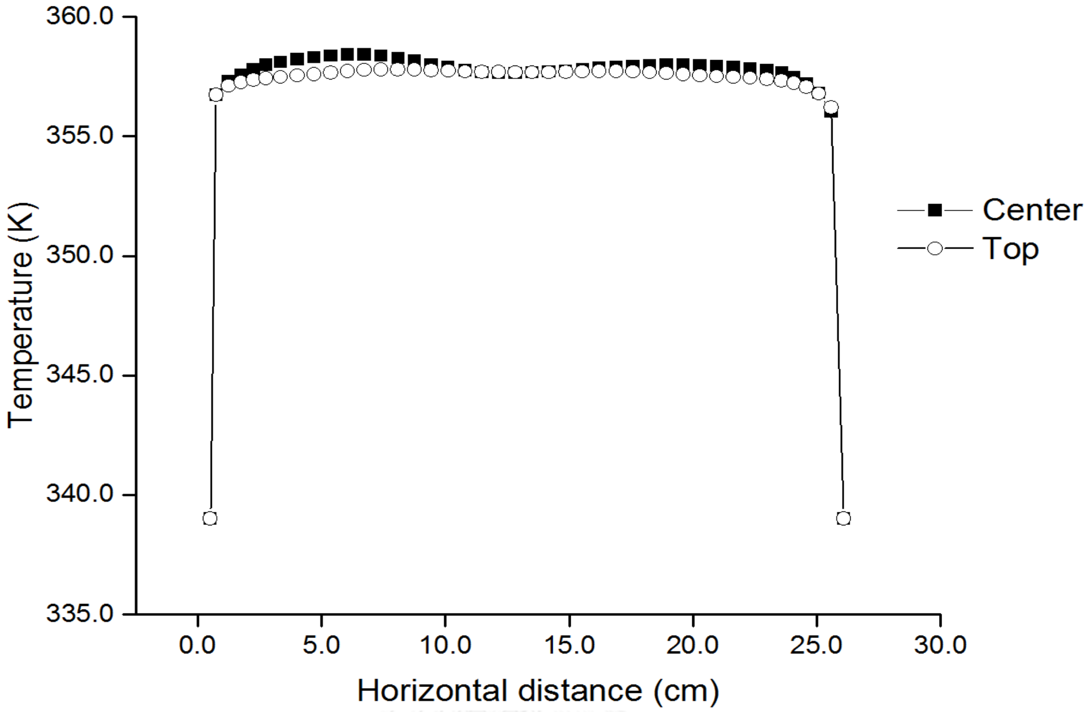

Fig. 5. 17 Time-averaged temperature distribution at the top and center.

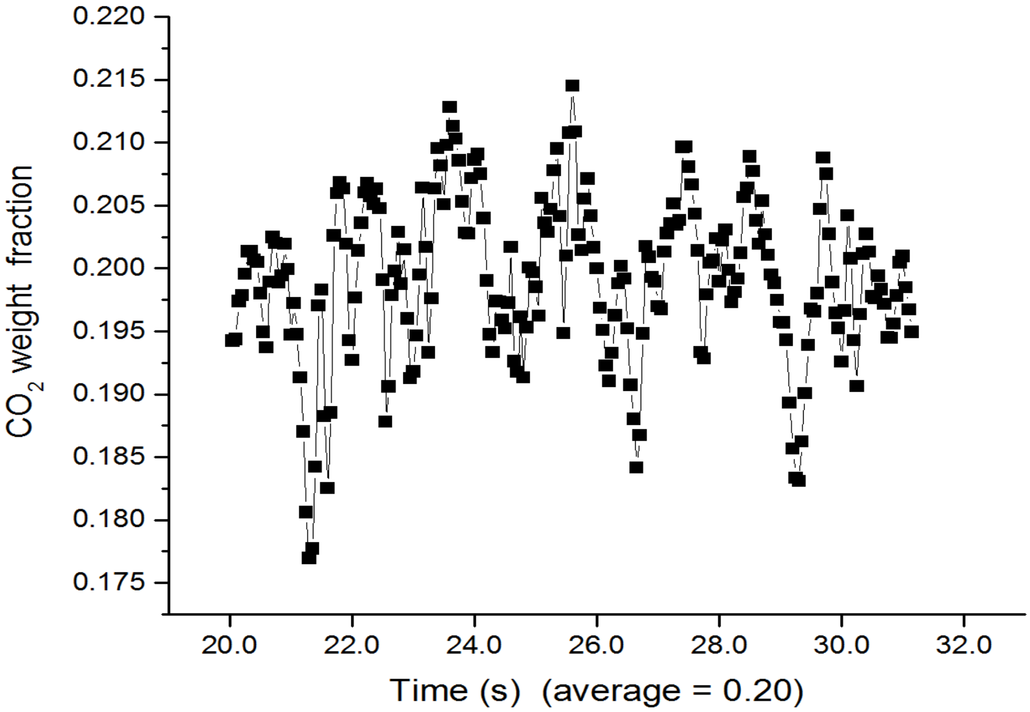

Fig. 5. 18 CO_2 weight fraction at the top of the bubbling bed.

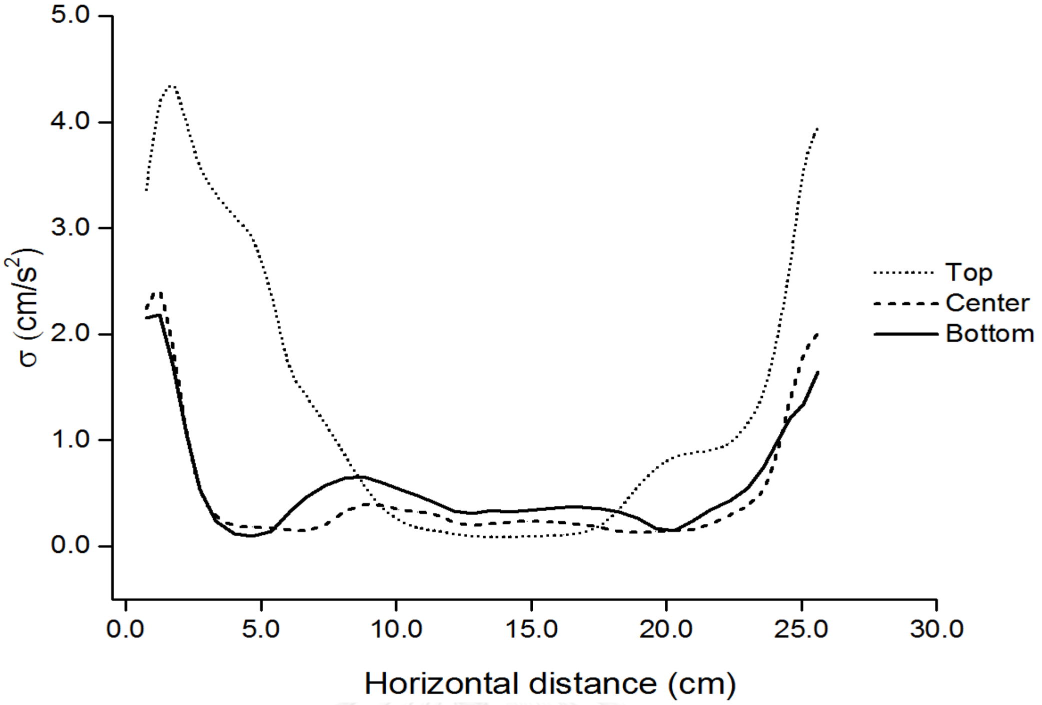

Fig. 5. 19 The variance of solid temperature along of the bed, averaged from 20 to 31 s.

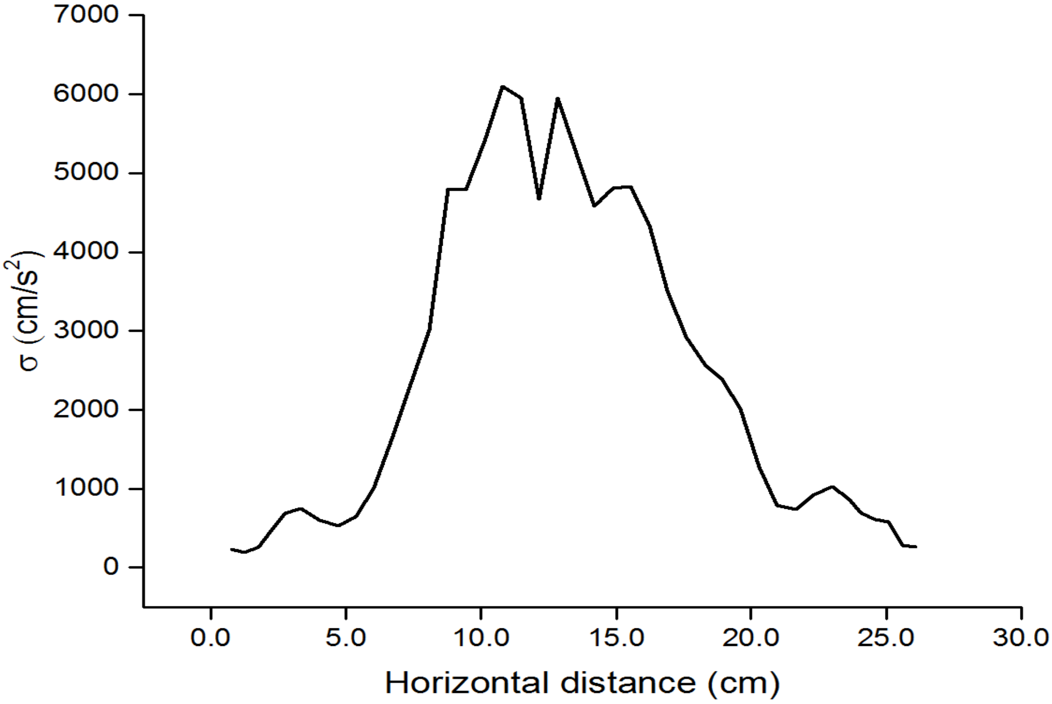

Fig. 5. 20 The variance of axial velocity of 50 μm solid in the center of the bed, averaged from 20 to 31 s.

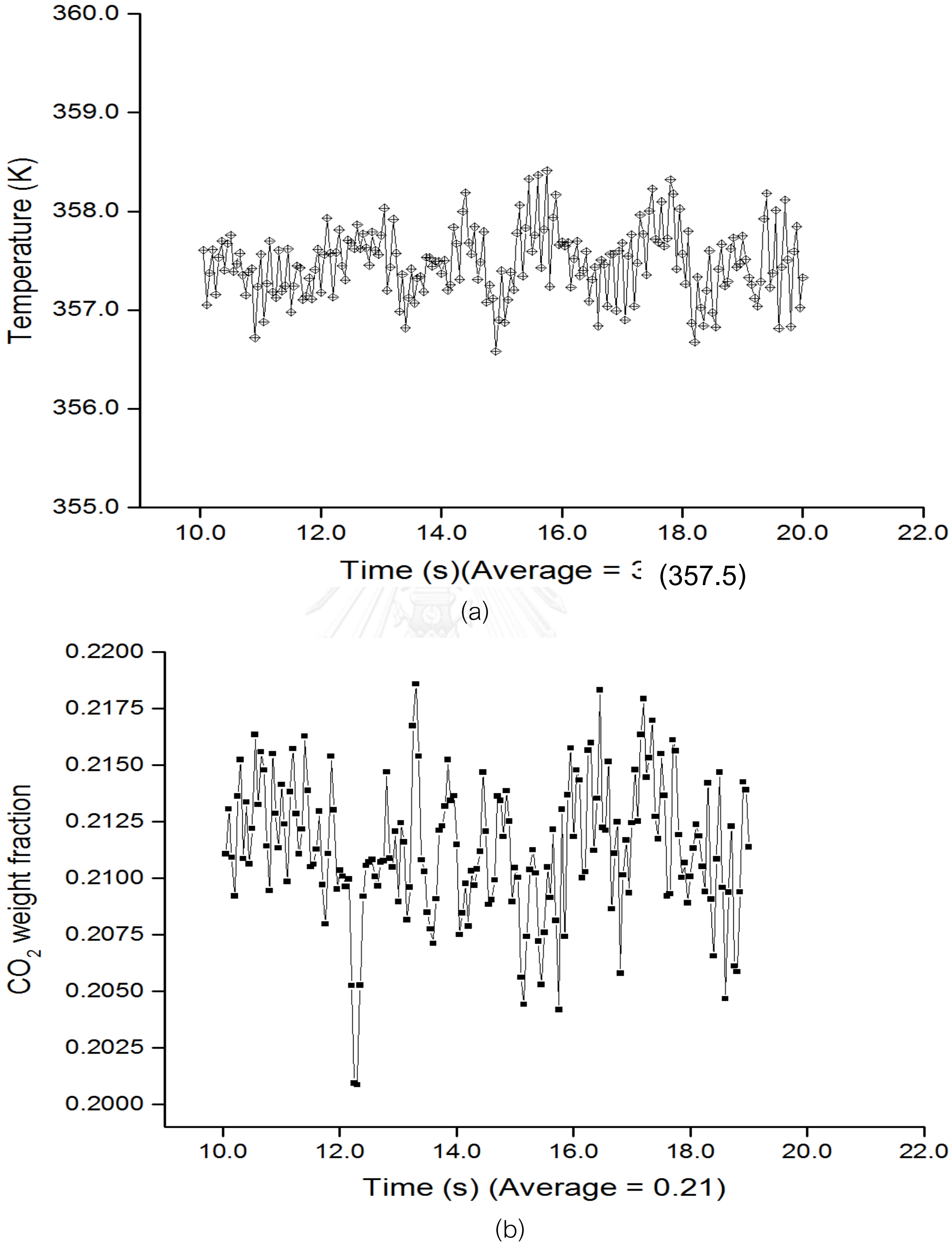

Fig. 5. 21 Effect of lower wall temperature, 310 K. (a) bed temperature at bed center.

(b): CO_2 weight fraction at the top of the fluidized bed.

Table 5. 1 Description of input data for 75 and 375 μm particles.

Geometry	
• Height (m)	1.2
• Inventory (m)	0.7
• Width (m)	0.25
Solid properties	
• Density (kg/m^3)	1.49
• Diameters	(1) 50 and 100 μm
	(2) 250 and 500 μm
Inlet fluid weight fractions	
• N_2	0.678
• CO_2	0.228
• H_2O	0.0934
Grid sizes	
• Lateral	$\Delta x = 6x10^{-3}$ m
• Axial	$\Delta y = 1x10^{-2}$ m fine and $\Delta y = 0.5x10^{-1}$ m coarse
Number of Grids	
• Radial x Axial	42 x 106 cells fine and 42 x 53 cells coarse
(Including boundary wall cells)	

Table 5. 2 Description of input data for 75 and 375 μm particles

Operating Conditions	
- Superficial gas velocity (m/s)	1.1
- Inlet velocities (m/s)	0.22, 2.25, 3.0, 2.25 and 0.22
- Initial solid volume fraction	0.58
- Pressure (atm)	1
- Temperature (K)	300
- Rate constant, k, s^{-1} (fast rate)	1
- Rate constant, k, s^{-1}(slow rate)	0.1

Table 5. 3 Operating conditions for various fluidized beds

(L, V and $Y_{(CO2)out}$ are estimated from calculations)

Average particle size (μm)	k(s^{-1})	L(m)	Superficial velocity, V(m/s)	$Y_{(CO2)out}$	$Y_{(CO2)in}$	$Y_{(CO2)out}/Y_{(CO2)in}$
375	1.0	0.7	0.65	0.05	0.228	0.22
375	0.1	0.7	0.65	0.192	0.228	0.84
75 (fine grid)	1.0	1.1	1.08	0.086	0.228	0.38
75 (coarse grid)	1.0	1.1	1.08	0.077	0.228	0.34
210	2.0	1.0	1.0	0.0015	0.006	0.25

Chapter VI

Two-dimensional CFD simulation of reducing operating pressure effect on the system hydrodynamics in a downer reactor

In this chapter, the system hydrodynamics of the downer reactor in a CFB downer (CFBD) reactor with reduced operating pressures attained by vacuum vent was investigated by computational fluid dynamics (CFD) simulation. The basis of using the current system is for desorbing CO_2 using dry solid sorbent capture process. Several solid mass fluxes were used to compare the flow behavior in axial and radial directions. The solid volume fraction and velocity distributions of the solid particles, as well as the system turbulences and granular temperature, were illustrated and discussed with five different reducing pressures and four different solid mass fluxes.

6.1.Introduction

Dry alkali metal-based solid sorbents (K_2CO_3 and Na_2CO_3) are one innovative method that has gained more attention due to their low energy-consumption and cost-effective nature [8, 136, 137]. The CO_2 sorption and regeneration capacities of solid sorbents have been evaluated at 60ºC and 150–400°C [7, 12, 138] but the system needs extra cooling or heating equipment. The difference in the temperature between the downer and riser reactors can lead to an ineffective CO_2 physical sorption. To avoid these differences in temperature, reducing the operating pressure in the downer reactor may be an appropriate solution for desorbing the CO_2 gas from the sorbents. Regeneration process is carried out by reducing pressure in the system. Since the pressure is proportional to temperature, lowering pressure leads to decrease of the regeneration temperature. However, a better understanding of this and the design of the downer reactor with an optional addition of reducing pressure is then an important requirement.

The circulating fluidized bed (CFB) system has been successfully used in both academic studies and industrial processes for several decades. Many advantages of the CFB exhibits in numerous processes, for example, enhance the mixing between gas-solid particles, reduce gas bubbles and improve high heat and mass transfers between the phases [13]. Conventionally, the CFB system consists of two main sections: a riser, which carries solid particles moving upward against the gravity force, and a downer where the solid particles from a riser move downwards in the same gravity direction. The downer section (reactor) is gaining more attention due to lower energy required for flowing gas and solid particles [139]. Since, in the downer reactor, the gas and solid particle flow co-currently downward without aeration needed. Moreover, the residence time distributions (RTD) curves showed a narrow peak, which means the solid dispersion in the axial and radial directions are dispersed uniformly comparing to the riser [140]. Recently, the numerical algorithm tools such as computational fluid dynamics (CFD) was widely applied for solving complicated equations and analyzing data in the past two decades for better understanding CFB hydrodynamics and chemical reactions. It was found that, the Eulerian-Eulerian approach is applied for calculating two- and three- dimensional downer reactors in many literatures [141-144].

6.2. System description, computational domain, boundary and operating conditions

The cold flow simulation of CFB system using a two-dimensional model downer reactor was developed as shown in Fig 6.1. A total height of circulating fluidized bed downer (CFBD) was 0.60 m and a width of 0.20 m and 0.10 m diameter were represented. At the initial time, the gas and solid particles moved downward through the system from the top at atmospheric pressure along with the gravity direction. Since the system is involved with lowering pressure, the conceptual design of this downer is to prevent solid particle blockage at the vacuum channel. Therefore, the downer section can be divided into two zones, the expanded (D_e) and the contracted (D_c) zones, respectively. The inlets of Nitrogen gas (N_2) were set both sides of the system at a slope angle above the bottom with a two-fold of minimum fluidization velocity ($2U_{mf}$). For the vacuum system, a two symmetrical side vacuum vents were located at 0.30 m below the top of the downer. The operating condition of solid mass flux entered in the downer reactor was estimated at 250, 500, 750 and 1,000 kg/m^2 s. The other operating conditions and boundary are represented in Table 6.1. For all velocities in this simulations, the studies of solid particle behavior were used a no-slip condition at the wall, except for the tangential velocity of the solid particle phase and the granular temperature. The boundary conditions of Johnson and Jackson [57] were used.

6.2.1. Mathematical model

As described in Chapter two, there are two methodology for modeling the gas-solid particle flow patterns including Eulerian-Eulerian (E-E) and Eulerian-Lagrangian (E-L) based groups. Generally, the Eulerian-Eulerian (E-E) approach is appropriate for fluidization study [22, 23]. The drag model or interphase exchange coefficient was used Gidaspow model due to this drag force is claimed to match with a high solid loading system and similar to the current study [24]. The mass and momentum conservations equations were solved by using numerical algorithms for each gas-solid phases. To close the governing equations and describe the solid particle characteristics, the kinetic theory of granular flow was carried out through the constitutive equations [25]. The simulation was used a commercial CFD software, Ansys Fluent 6.2.16. To couple the pressure and velocity, this study was used phase coupled SIMPLE algorithm.

6.3. Results and discussion

6.3.1. Validation of the CFD model

6.3.1.1 Grid independence test

The various computational cells or grid sizes were calculated in order to test the grid independency for the CFD results. To observe the optimum point of CFD model, a suitable condition between a simulation times and an acceptable accuracy of the solution are essential for those concern. In this study, the non-uniform computational cells used are performs for 4,000, 8,000 and 12,000 meshes in Fig. 6.2. The computed time-averaged solid volume fraction profiles which were calculated by using different computational cells are shown in Fig. 6.3. The simulation results illustrated that there were significant deviations in the using 4,000 mesh results because of the large gradients in the properties of the flow. On the other hand, the hydrodynamic behaviors results obtained with an increasing computational cells of 8,000 and 12,000 meshes were quite similar. According to the results, the computational cells with 8,000 meshes were sufficiently fine computational cells or grid sizes for calculating the simulation in the following sections.

6.1.1.2. Quasi-steady state test

In order to systematically explain the results, the quasi-steady state time-averaged range requires clarification, and so the results were averaged after the system reached a quasi-steady state condition. Comparison of the computed time-averaged solid volume fraction profiles for the CFBD reactor with three different time-averaged ranges (Fig. 6.4) revealed similar solid volume fraction results with 10–20 s and 20–30 s time-averaged ranges, but that from the shorter 0–10 s time-averaged range was slightly different. Thus, the CFBD reactor had entered the quasi steady-state conditions from simulation times of more than 10 s, and so in this study the CFB model would use the 10–30 s time-averaged range of the simulation time.

6.3.2. Comparison of the system hydrodynamics

6.3.2.1. Pressure drop

Fig. 6.5 shows the pressure drop profiles in the CFBD reactor with five different reducing pressures (0.99 to 0.90 atm) and four solid mass fluxes (250, 500, 750 and 1,000 kg/m^2 s), respectively. The simulation results provided that, from the top of the downer, the pressure drop profiles were nearly zero and constantly gravitated above the bottom of the column until 0.40 m system height for all the solid mass fluxes. Moreover, the results showed the various distribution of pressure drop at the connecting position of outlet vacuum vent at the expanded zones were considerably fluctuated which could disturb and lower the pressure drop inside the system. Pressure drop again drastically oscillated to match with the pressure at bottom outlet below the outlet vacuum vent. When increasing the solid mass fluxes, the calculated absolute pressure near the bottom section are increased since the acceleration by gravity force are more influence than the drag force in the upward direction. The calculation of pressure drop across the bed can obtain the net weight of the solid particles. Comparing the different operating pressures, it can be concluding that operating pressures of 0.90 and 0.99 atm gave the highest and lowest deviation in the pressure drop profiles, respectively. The lowest solid mass flux of 250 kg/m^2 s at the reducing pressures of 0.99 and 0.975 atm provided the lowest pressure drop fluctuation while the reducing pressure of 0.90 atm gave the highest pressure drop fluctuation and decreased with the solid mass flux. Furthermore, the pressure drop profile for the reducing pressures of 0.95 and 0.925 atm were constant throughout the simulation. This can be described by the amount of solid particles inside the system and the available movable space. The reducing pressure of 0.95 atm will be applied for further study.

6.3.2.2 Solid volume fraction

The simulation results for the instantaneous contours of the solid volume fraction at outlet pressure of 0.95 atm with solid mass fluxes of 250, 500, 750 and 1,000 kg/m^2 s in the CFBD reactor are shown in Fig. 6.6. The flow behaviors for each solid mass flux at the simulated snapshot of 10 s, 20 s and 30 s was remained constant. The solid volume concentration increased with the height of the CFBD reactor increased. At the top section of column, the particles had fallen downwards due to the gravitational acceleration and accumulated at the bottom region. The flow behavior moved towards on one side due to the self-sustained fluctuation by the sudden compression. At the bottom section, the influence of the secondary N_2 flow fed from the two-side inlets next to the bottom outlet oscillating the solid particles especially at the center region. The gas bubbles are formed and developed inside the system. These fluctuations between gas and solid particles increased with an increasing solid mass flux as a result of a high solid inventory. At the lowest solid mass flux condition, 250 kg/m^2 s, the solid volume fraction could be separated into the two main regions since the results show there is a lot of empty space in the CFBD reactor, but this space decreased to almost half of the expanded zone (De) at the higher solid mass flux of 500 kg/m^2 s which can be defined as the dilute and dense regions at the top and bottom of the CFBD reactor, respectively [26]. However, there was no space apparently at the higher solid mass flux of 750 and 1000 kg/m^2 s, and the system could not be visibly separated into different regions. Rather, the increase of solid mass flux resulted in the solid particles just reaching the connecting of the outlet vacuum vent at 0.30 m below the top of the CFBD reactor. Thus, this downer height is likely to be insufficient for a solid mass flux greater than 750 kg/m^2 s as the solid particles were flown out of the system.

Fig. 6.7 shows the comparison of the time- and area- averaged solid volume fraction profiles with the five different reducing pressures and four solid mass fluxes in the CFBD reactor. The solid volume fraction entered across the whole cross-sectional area with an initial solid volume fraction of 0.40 at the inlet and decreased to 0.20–0.30 as the solid particles flew into the contracted zone (Dc), and then the solid particles accumulated again at the bottom section. Fig. 6.7(a) to 6.7(d) showed the solid volume fraction of four solid mass fluxes entered uniformly from the entrance to 0.4 m above the bottom of the CFBD similarly with the pressure drop profiles since this area were not influenced from the vacuum vent. However, the solid volume fraction at lower 0.4 m above the bottom showed the various distribution along the CFBD height when solid mass fluxes increased. Due to the large pressure change between the exit and about 0.30 m above the outlet of the CFBD reactor, decreasing the operating pressure slightly affected the solid volume fraction. The highest outlet pressure (0.99 atm) showed the solid volume fraction profiles for all solid mass fluxes were not significantly different because it has the lowest difference between the operating pressures and the atmospheric pressure. Decreasing the operating pressure resulted in the solid particles being more expanded in the CFBD reactor, consistent with that previously reported [27], except at the lowest solid mass flux (250 kg/m^2 s) where the trend was not clearly seen due to the low density (quantity) of solid particles.

The applicable space in the CFBD reactor is inversely proportional to the solid mass flux due to the solid particles are available to move in the vacant places. At all operating pressures, the accumulation of solid particles occurred near the bottom outlet, except for that at the highest pressure (0.99 atm). Therefore, the flexibility of the solid particles in the system infers the turbulence inside the system. Since the explanation for the fluctuation in the radial solid volume fraction profiles with different operating pressures still have the unclear trend, which is similar to the previously reported in the hydrodynamics in a conventional riser in the bubbling regime but is different to that reported in a CFBD [5, 28]. The gas bubbles which occur inside the system are possibly improving the system highly heterogeneous.

6.3.2.3. Radial solid particle velocities

To investigate the hydrodynamic characteristics of gas-solid in the CFBD reactor, the particle velocity is an important parameter to study. The radial solid particle velocity profiles of the time- and area- averaged with the five different reducing pressures and four different solid mass fluxes represented a uniform distribution while entering from the top, but the oscillation occurred at a height approximately 0.20 m above the bottom outlet as shown in Fig. 6.8. At any radial position, the solid velocity profile can be calculated indirectly from the solid mass flux divided by solid volume fraction and solid density. As increasing of the solid mass flux and reducing pressure inside the system leads the radial solid particle velocities to oscillate more, the positive and negative values in the radial solid particle velocities can be implied that the solid particle motions were moved to the left and right system sides randomly.

6.3.2.4. Axial solid particle velocities

The axial solid particle velocity profiles of the time- and area- averaged with the five different reducing pressures and four different solid mass fluxes are shown in Fig. 6.9. Due to a period of free-fall condition, the solid particles at the axial solid particle velocity entered through the CFBD reactor with an initial value close to zero. Above the bottom outlet roughly at 0.35 m, the negative value appeared due to the solid particle motions move downward. Then, particle velocity increased and remained constant close to the outlet section results in the drag force has increased to equal the gravitational force. No significant effect on the axial solid velocity profiles was observed when increasing the amount of solid particles and operating pressure, which remained evenly distributed along the height of the CFBD reactor except for with a solid mass flux of 250 kg/m^2 s in Fig. 6.9(a). At the operating pressures of 0.90 and 0.925, which provided the highest deviation in the pressure drop profiles in section 6.3.2.1. When the lowest employed solid mass flux was influenced from high pressure drop of the sudden compression at the connecting of the outlet vacuum vent at 0.30 m, the system showed high axial solid particle velocities. Rather, the positive values can be implied that the solid particle motions were randomly moved up in the system. Furthermore, the axial solid particle velocity profiles decreased with increasing operating pressure under that low solid mass flux condition.

6.3.2.5. Normal Reynolds stresses

The main turbulence characteristic is produced by the additional stresses due to the high random velocity fluctuations, known as normal Reynolds stresses $(\overline{v_i^{'}v_i^{'}})$, where the subscript "i" refers to the direction. The normal Reynolds stress of a solid particle can be calculated in both the axial (y) and radial (x) system directions, as detailed by Gidaspow and Jiradilok [29] and shown in Eq. (6.30);

$$(\overline{v_i^{'}v_i^{'}}) = \frac{1}{m}\sum\nolimits_{k=1}^{m}(v_{ik}(r,t)-\bar{v}_i(r))(v_{ik}(r,t)-\bar{v}_i(r)) \qquad (6.30)$$

where m is the overall number of data in the period time.

The normal Reynolds stresses of the time- and area- averaged with the five different reducing pressures and four different solid mass fluxes are displayed in Fig. 6.10. It can be seen that, the normal Reynolds stresses at a solid mass flux of 250 kg/m^2 s had a higher fluctuation from approximately 0.30 m above the bottom outlet than those with the other three higher solid mass flux levels, again being due to that it is at the circulation zone. The large velocity fluctuation reflects the high system energy required to support the weight of the solid particles [28]. For the other three higher solid mass fluxes, increasing the solid mass flux did not have any effect on the normal Reynolds stress, where the profiles were uniform and close to zero along the reactor height.

The radial distributions of the time-averaged solid particle axial normal Reynolds stresses in the CFBD reactor at a height of 0.00 m, 0.10 m, 0.20 m and 0.30 m above the bottom outlet were consistent with that previously reported [5], where the solid particle normal Reynolds stresses were high in the section that has the ability of solid particles to move (500 and 750 kg/m^2 s are shown in Figs. 6.11 and 6.12, respectively). At 0.20 and 0.30 m, the results showed that the axial normal Reynolds stresses profiles are almost flat in the dilute zone from the top of the downer. While the oscillations display the same phenomena at the height of 0.00 and 0.10 m as appeared in the bubble fluidization in the dense zone [145]. In addition, these results are consistent with the time- and area-averaged radial solid particle normal Reynolds stresses in the CFBD reactor (Fig. 6.13) as well as the radial distributions of the time-averaged radial solid particle normal Reynolds stresses (Figs. 6.14 and 6.15, respectively), which can likewise be explained using the same reason as the axial solid particle normal Reynolds stress. The time-averaged solid axial and radial normal Reynolds stress are shown in Figs. 6.11 and 6.12 and Figs. 6.14 and 6.15, respectively. It can be seen that, at the axial direction which is the same direction of the flow, the normal Reynolds stresses were large comparing with at the axial direction [146].

6.3.2.6. Granular temperature

The granular temperature is defined as the kinetic energy of an oscillating solid particle. Chalermsinsuwan et al. [5, 28] Tartan [30] and Tartan and Gidaspow [31] described the equations for calculating granular temperature as shown in Eq. (6.31),

$$\theta(t,x) = \frac{1}{3}\left\langle v_r^{'} v_r^{'} \right\rangle + \frac{1}{3}\left\langle v_\theta^{'} v_\theta^{'} \right\rangle + \frac{1}{3}\left\langle v_z^{'} v_z^{'} \right\rangle \tag{6.31}$$

For two-dimensional CFD modeling system, velocity in the radial direction or non-flow direction is assumed to be the same. So, the turbulent granular temperature then can be rearranged by using equation in Eq. (6.32),

$$\theta(t,x) \cong \frac{2}{3}\left\langle v_r^{'} v_r^{'} \right\rangle + \frac{1}{3}\left\langle v_z^{'} v_z^{'} \right\rangle \tag{6.32}$$

A high granular temperature reflects particles with high energy that can make them move or shake. Accordingly, solid particles with a high granular temperature can transport more independently than those with a low granular temperature. The granular temperature of the time- and area- averaged with the five different reducing pressures and four different solid mass fluxes are displayed in Fig. 6.16 showed that the granular temperature significantly affected the system at a solid mass flux of less than 1000 kg/m^2 s. Since there were low solid particles in the system at those solid particle flow rates. Difference operating pressure revealed a high granular temperature at different regions of the CFBD reactor. At the highest operating pressure of 0.99 atm illustrated that there was a high granular temperature at the top section. On the other hand, at the lower operating pressure of 0.90 atm showed a high granular temperature at the center and the bottom sections. As the solid mass flux increased, the oscillations in the dense system or the high solid inventory were lower than those in the dilute system or the low solid inventory because of the vacant space between solid particles or solid particle clusters. The time-averaged granular temperature of the radial distributions in the CFBD reactor also displayed that the highest granular temperature at all heights above the bottom outlet was found at the lowest operating pressure of 0.90 atm, with that for the representative solid mass fluxes of 500 and 750 kg/m^2 s are shown in Figs. 6.17 and 6.18, respectively.

To present the results more generally for the downer system in the current study, the averaged total granular temperatures comparing with four different mass fluxes and five reducing pressures is displayed in Fig. 6.19. From the obtained results, it can be concluded that the system with solid mass flux less than 1,000 kg/m^2 s, the reducing pressure had an effect on the total granular temperature. There had a minimum condition for the total granular temperature. The low and high reducing pressures in the downer reactor make the solid particles to have high fluctuation inside the system. This can be explained by the effect of collision among particles and available movable space. The fluctuation inside the system was lowest for the reducing pressure of 0.925 atm. However, the total granular temperature at solid mass flux of 1,000 kg/m^2 s showed a low independently from pressure reduction because of the high amount of solid particle inside the system.

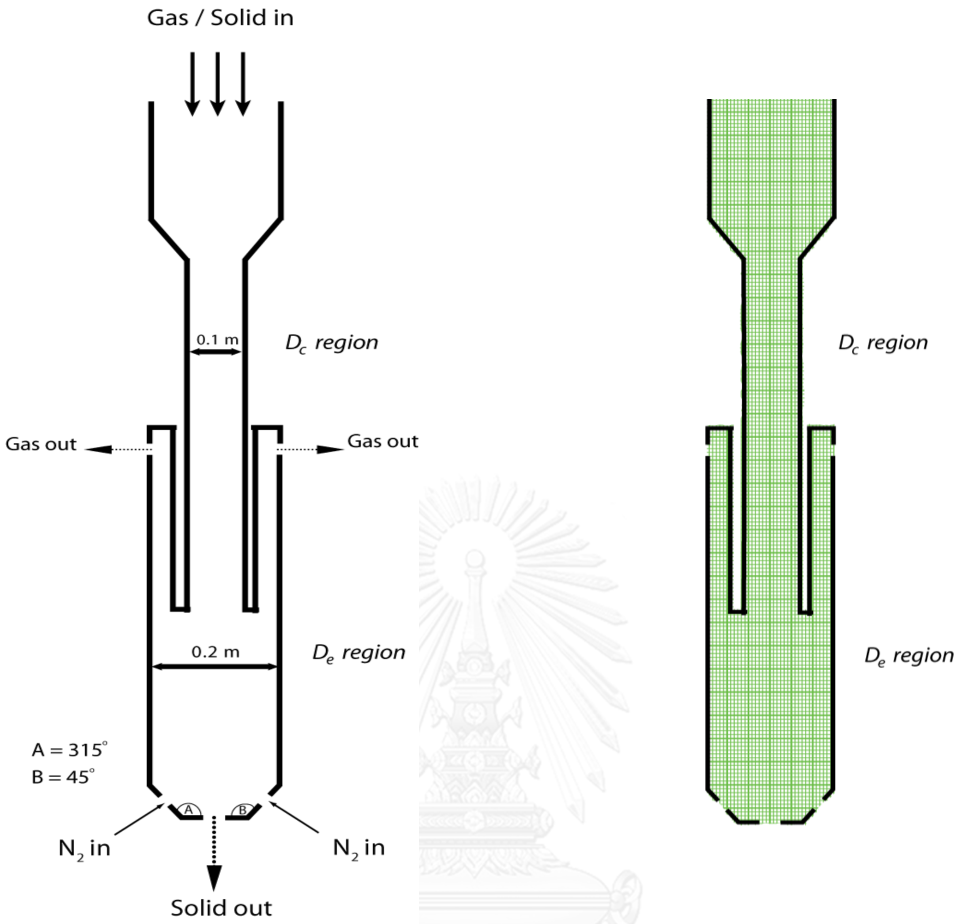

Fig. 6. 1 (a) Schematic drawing and (b) computational domains and their boundary conditions of the simplified CFBD reactor used in this study. D_e and D_c represent the expanded and contracted zones, respectively.

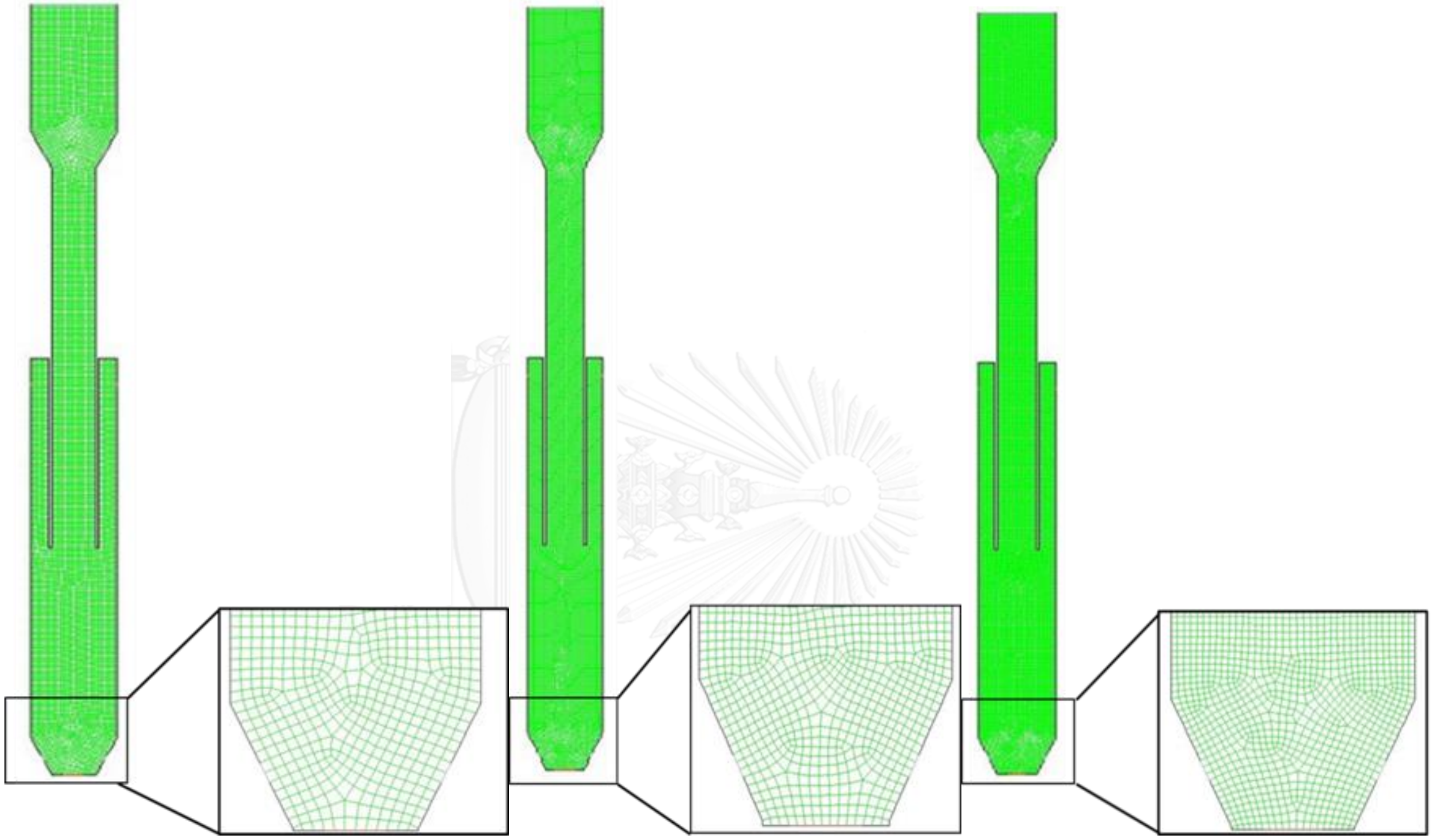

(a) (b) (c)

Fig. 6. 2 Grid independency test with computational cells of (a) 4,000, (b) 8,000 and (c) 12,000 meshes.

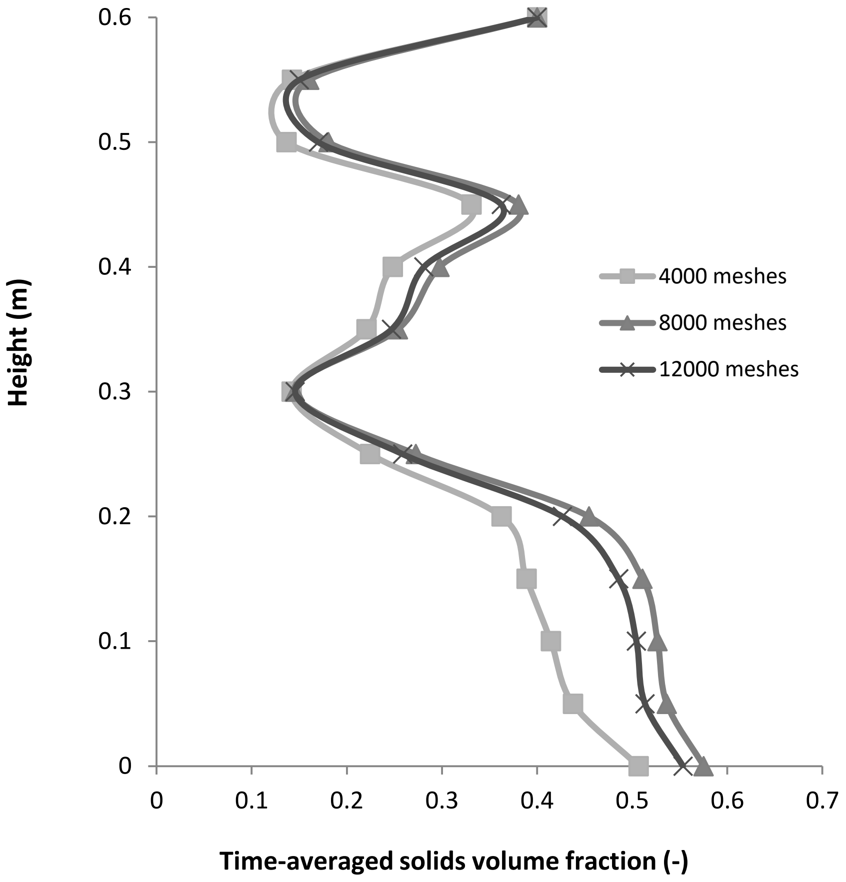

Fig. 6. 3 The computed solid volume fraction profiles in the CFBD reactor using computational cells with three different meshes.

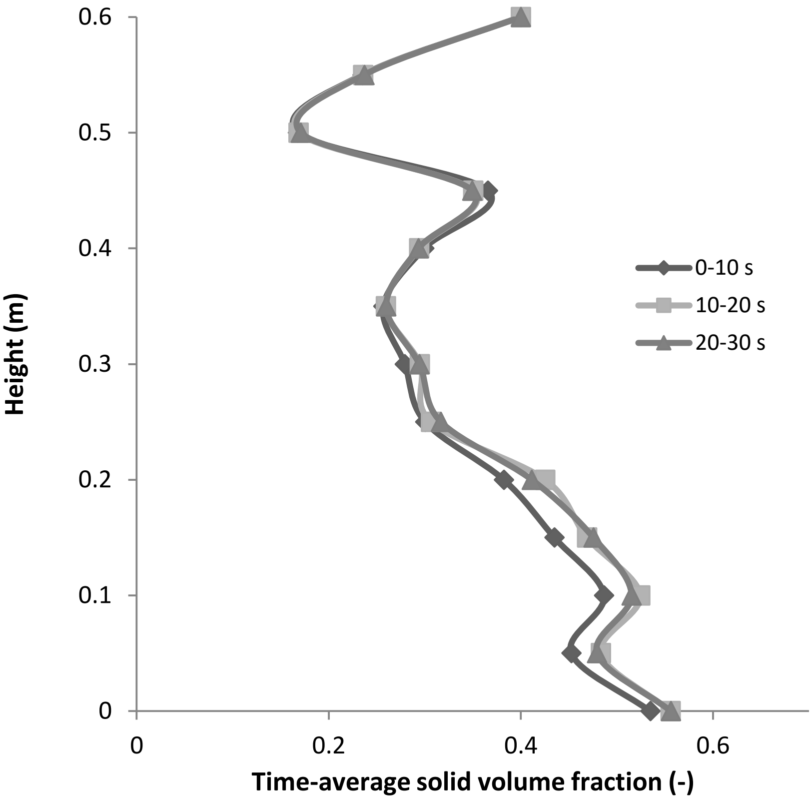

Fig. 6. 4 The computed solid volume fraction profiles in the CFBD reactor when derived from different time-averaged ranges.

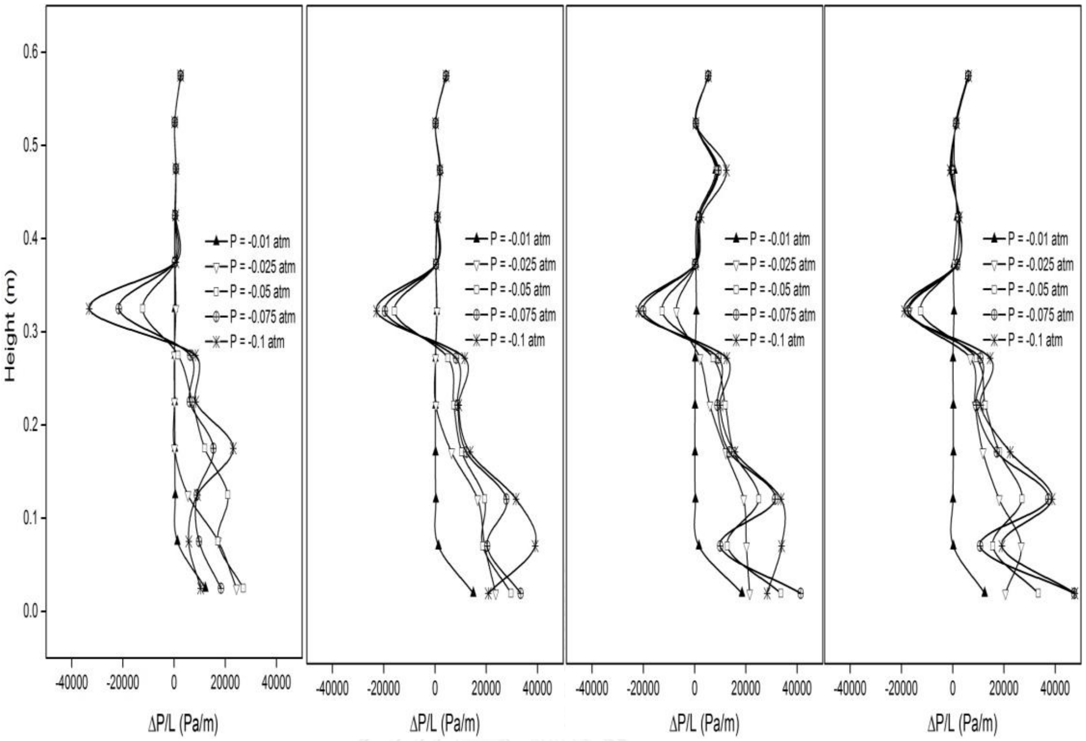

(a) (b) (c) (d)

Fig. 6. 5 The computed time-averaged pressure drop profiles in the CFBD reactor with a solid mass flux of (a) 250, (b) 500, (c) 750 and (d) 1,000 kg/m^2 s at five different reducing pressures.

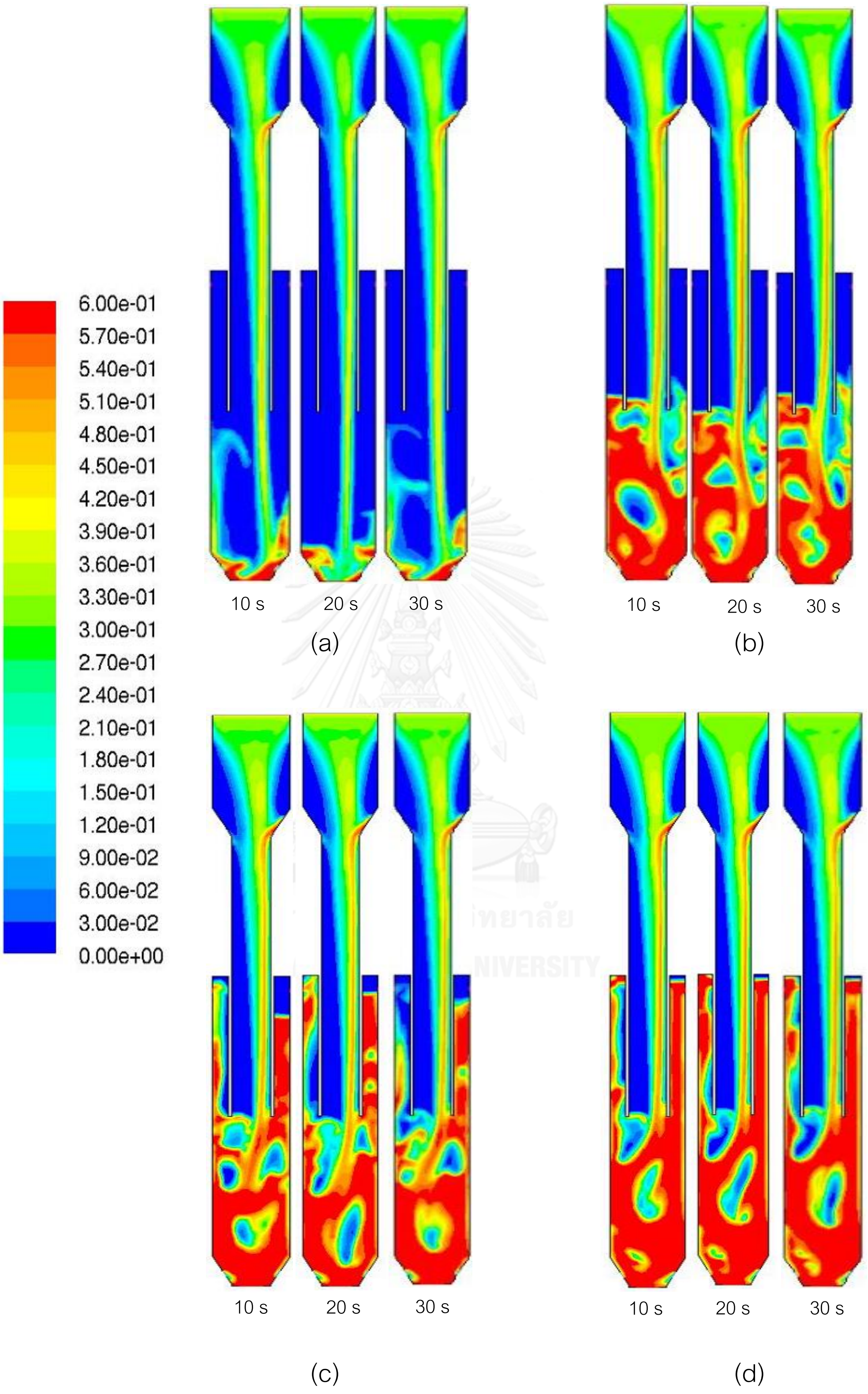

(a) (b) (c) (d)

Fig. 6. 6 The instantaneous contours of the solid volume fraction with solid mass fluxes of (a) 250, (b) 500, (c) 750 and (d) 1,000 kg/m^2 s at an operating pressure of 0.95 atm.

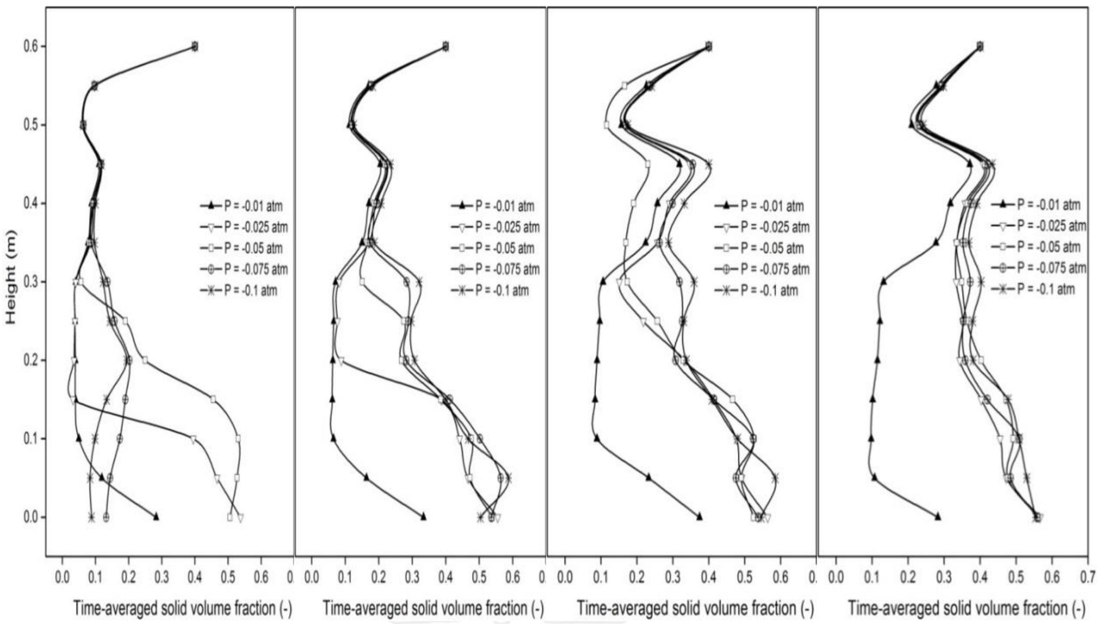

(a) (b) (c) (d)

Fig. 6. 7 The computed time-averaged solid volume fraction profiles in the CFBD reactor with a solid mass flux of (a) 250, (b) 500, (c) 750 and (d) 1,000 kg/m^2 s at five different reducing pressures.

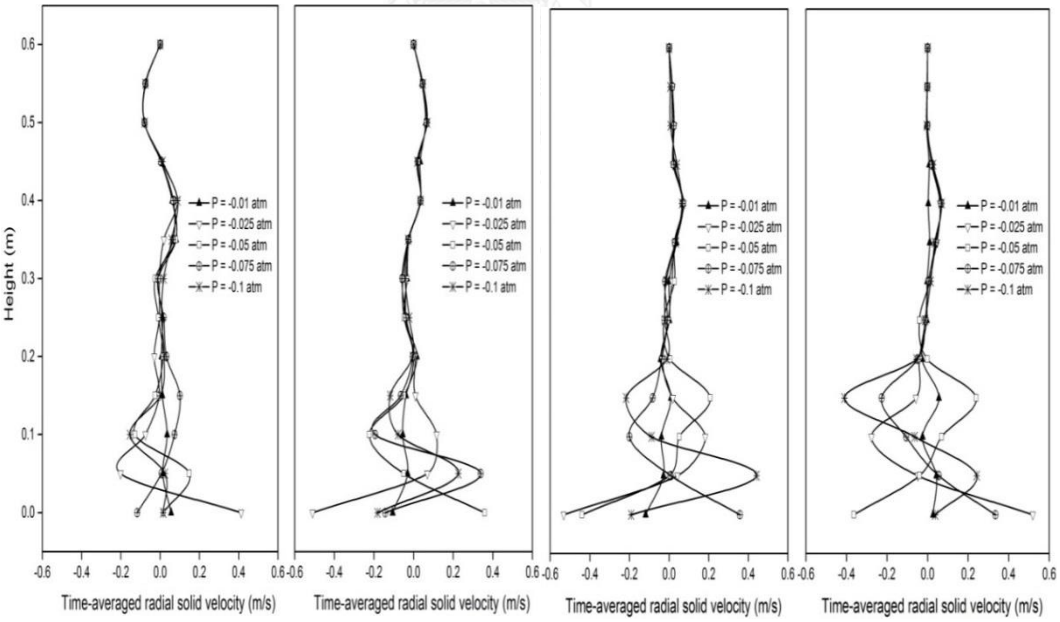

(a) (b) (c) (d)

Fig. 6. 8 The computed time-averaged radial solid particle velocity profiles in a CFBD reactor with a solid mass flux of (a) 250, (b) 500, (c) 750 and (d) 1,000 kg/m^2 s at five different reducing pressures.

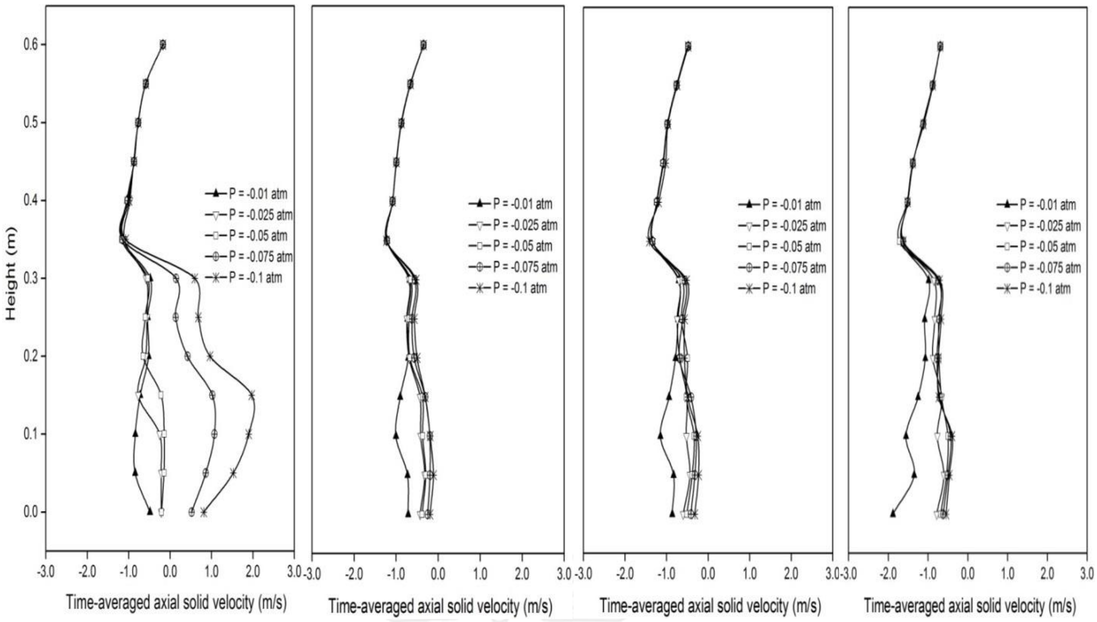

(a) (b) (c) (d)

Fig. 6. 9 The computed time-averaged axial solid particle velocity profiles in the CFBD reactor with a solid mass flux of (a) 250, (b) 500, (c) 750 and (d) 1,000 kg/m^2 s at five different reducing pressures.

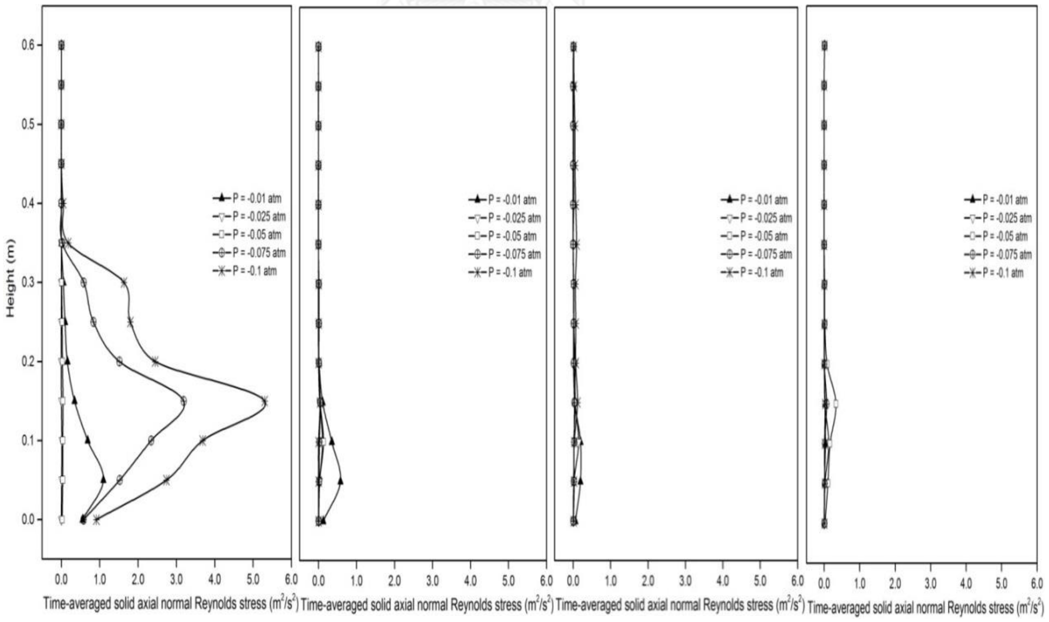

(a) (b) (c) (d)

Fig. 6. 10 The computed time-averaged solid axial normal Reynolds stress profiles in the CFBD reactor with a solid mass flux of (a) 250, (b) 500, (c) 750 and (d) 1,000 kg/m^2 s at five different reducing pressures.

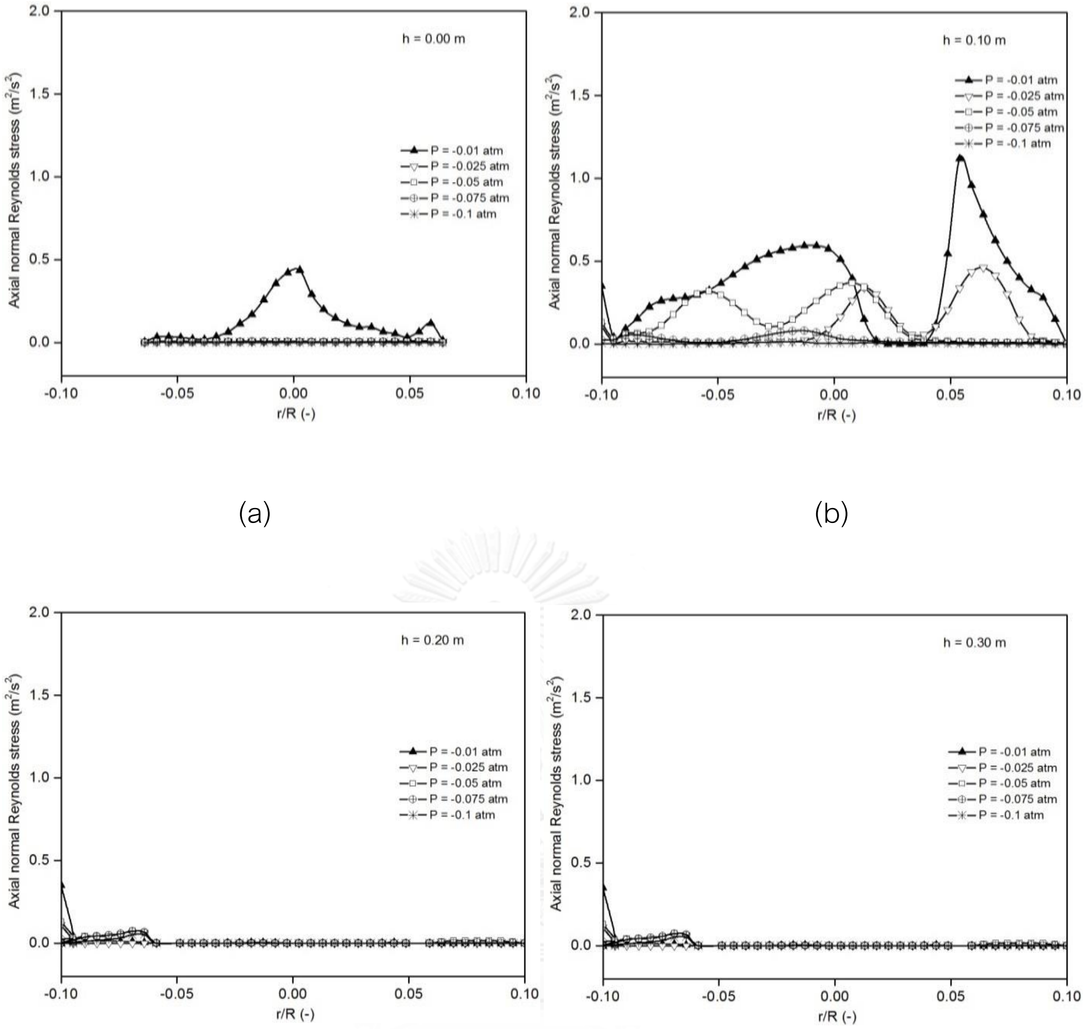

(a) (b)

(c) (d)

Fig. 6. 11 The radial distributions of the time-averaged solid axial normal Reynolds stress at a CFBD reactor height (h) of (a) 0.00, (b) 0.10, (c) 0.20 and (d) 0.30 m with a solid mass flux of 500 kg/m^2 s at five different reducing pressures.

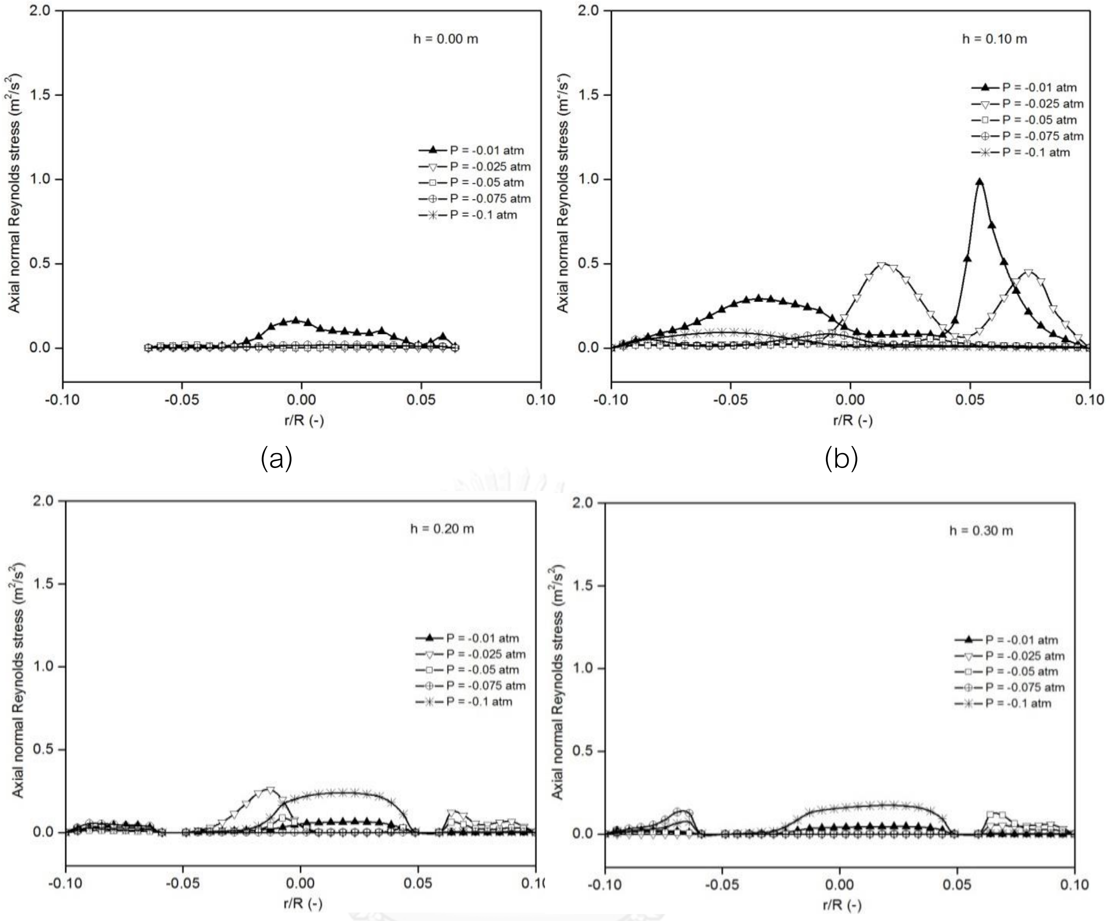

(a) (b)

(c) (d)

Fig. 6. 12 The radial distributions of the time-averaged solid axial normal Reynolds stress at a CFBD reactor height (h) of (a) 0.00, (b) 0.10, (c) 0.20 and (d) 0.30 m with a solid mass flux of 750 $kg/m^2 s$ at five different reducing pressures.

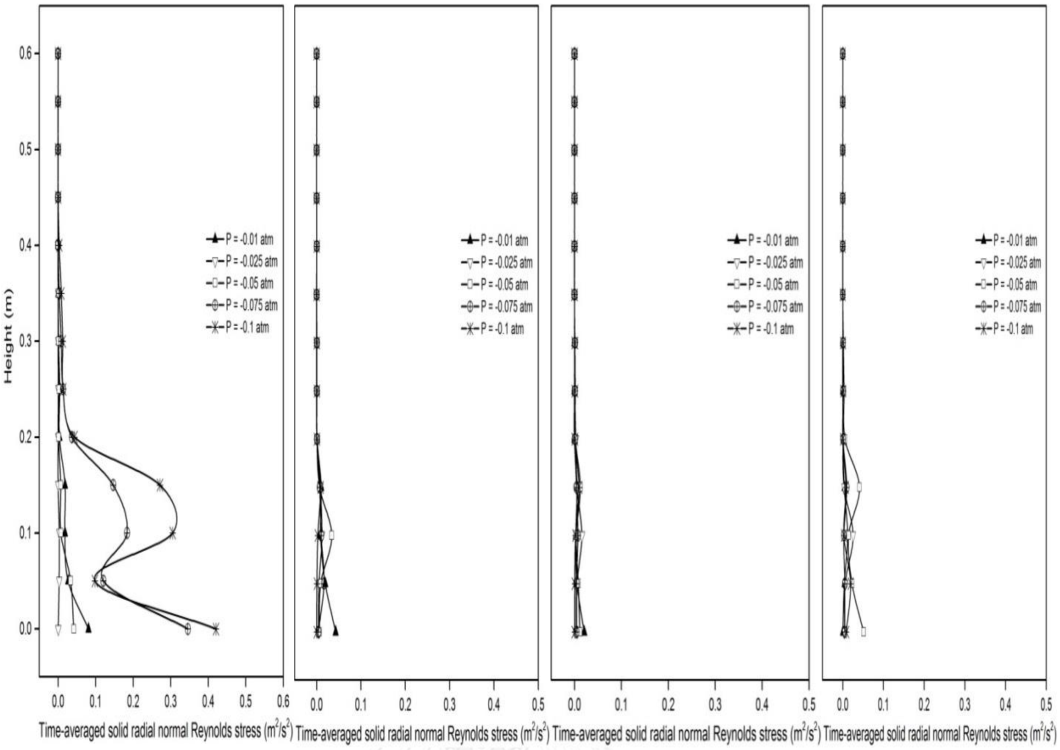

(a) (b) (c) (d)

Fig. 6. 13 The computed time-averaged solid radial normal Reynolds stress profiles in the CFBD reactor with a solid mass flux of (a) 250, (b) 500, (c) 750 and (d) 1,000 kg/m^2 s at five different reducing pressures.

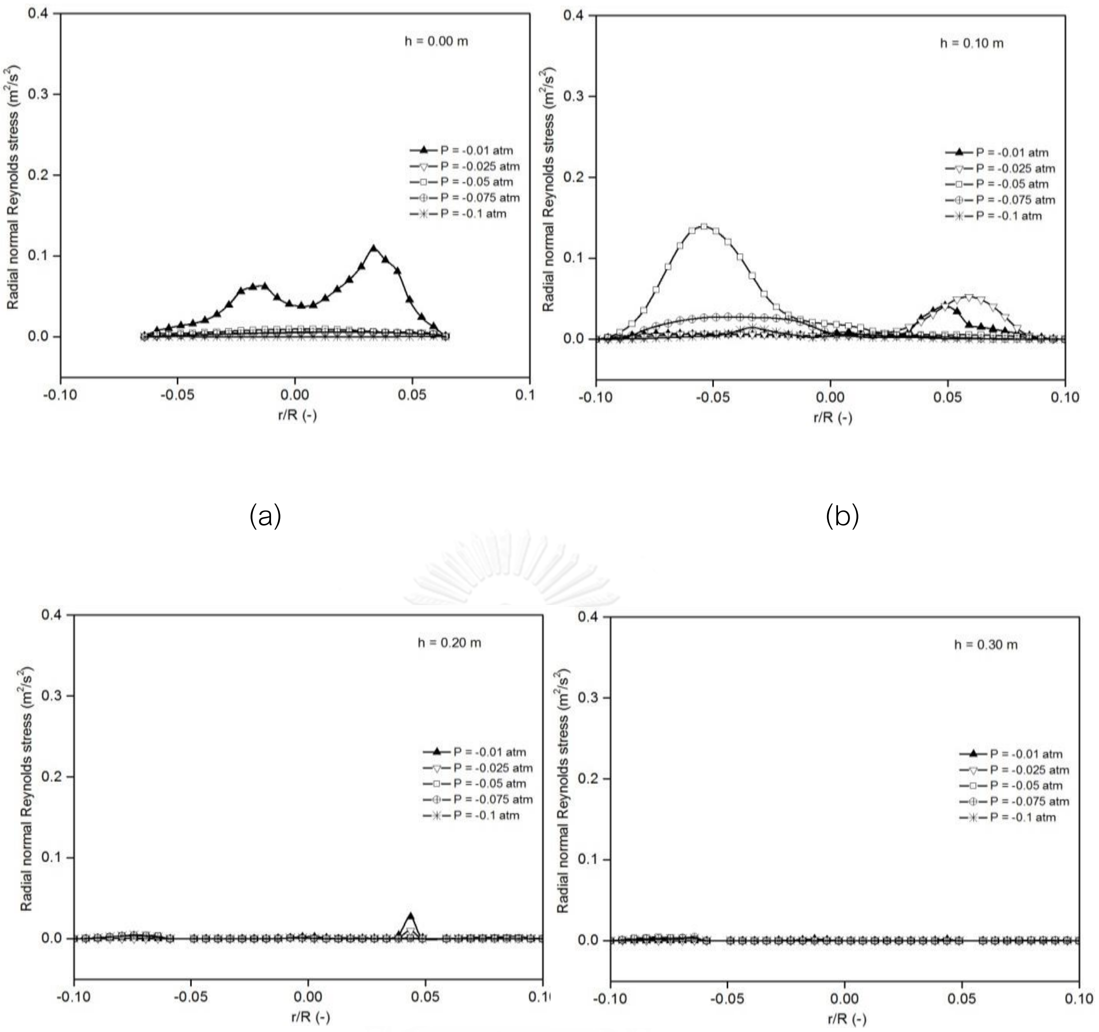

(a) (b)

(c) (d)

Fig. 6. 14 The radial distributions of the time-averaged solid radial normal Reynolds stress at a CFBD reactor height (h) of (a) 0.00, (b) 0.10, (c) 0.20 and (d) 0.30 m with a solid mass flux of 500 kg/m^2 s at five different reducing pressures.

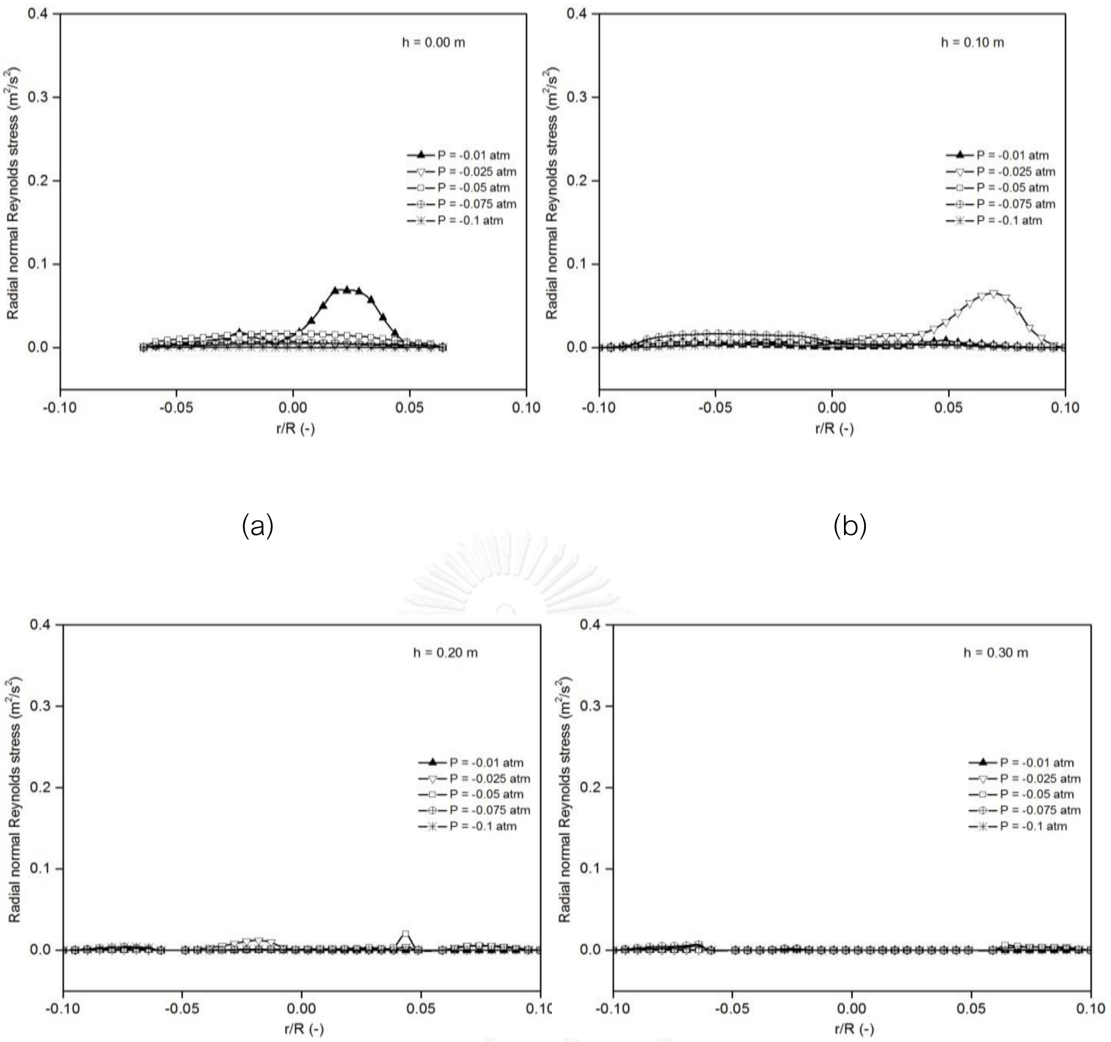

(a)

(b)

(c)

(d)

Fig. 6. 15 The radial distributions of the time-averaged solid radial normal Reynolds stress at a CFBD reactor height (h) of (a) 0.00, (b) 0.10, (c) 0.20 and (d) 0.30 m with a solid mass flux of 750 kg/m^2 s at five different reducing pressures.

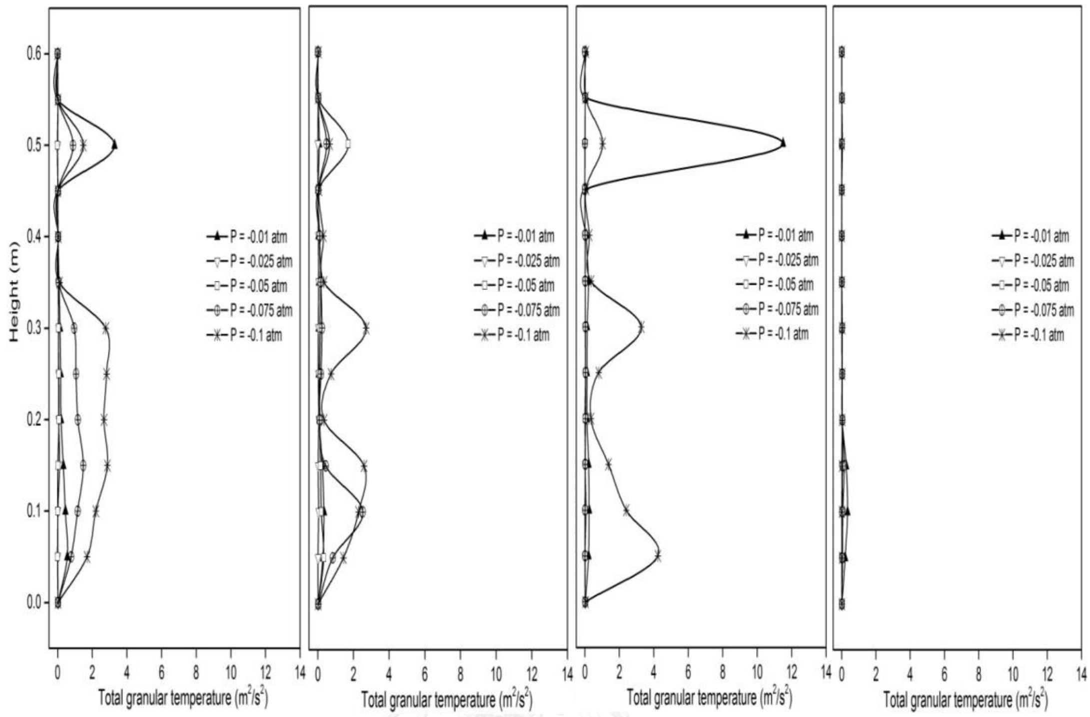

(a) (b) (c) (d)

Fig. 6. 16 The computed time-averaged granular temperature profiles in the CFBD reactor with a solid mass flux of (a) 250, (b) 500, (c) 750 and (d) 1,000 kg/m^2 s at five different reducing pressures.

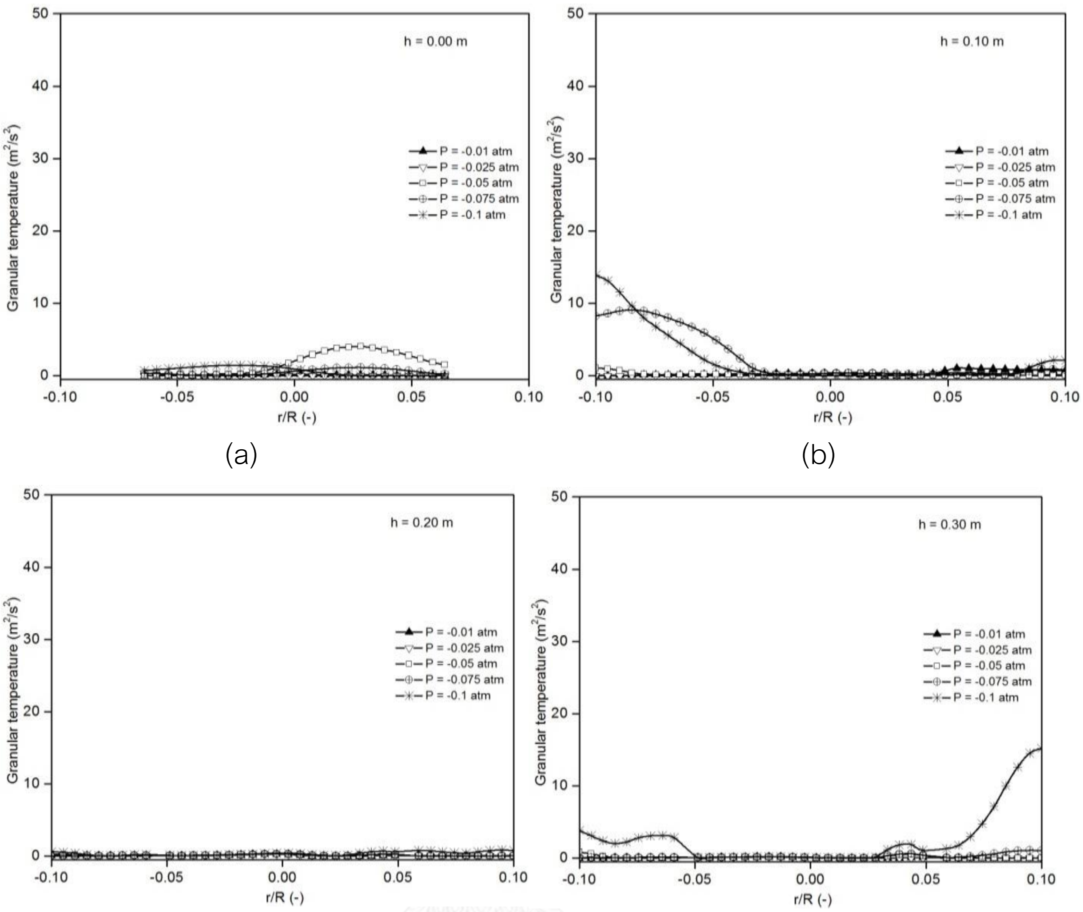

(a) (b)

(c) (d)

Fig. 6. 17 The radial distributions of the time-averaged granular temperature at a CFBD reactor height (h) of (a) 0.00, (b) 0.10, (c) 0.20 and (d) 0.30 m with a solid mass flux of 500 kg/m^2 s at five different reducing pressures.

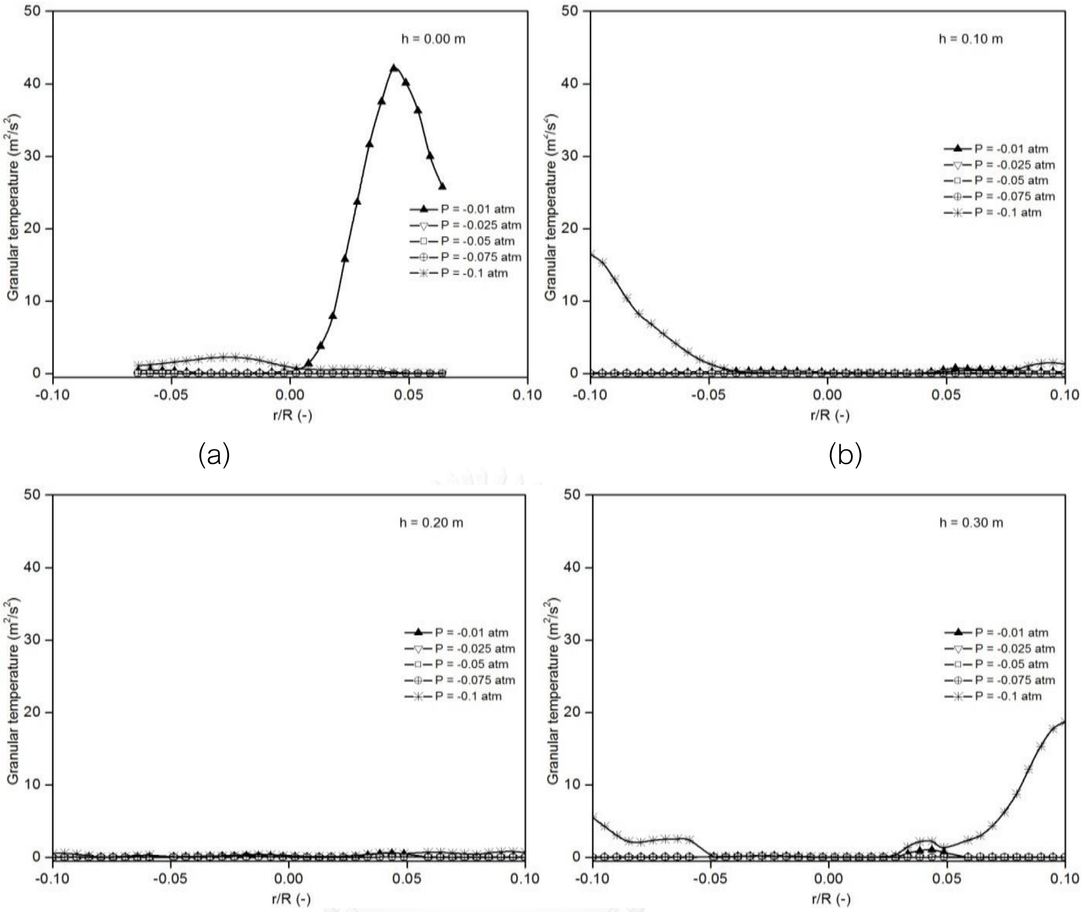

(a) (b)

(c) (d)

Fig. 6. 18 The radial distributions of the time-averaged granular temperature at a CFBD reactor height (h) of (a) 0.00, (b) 0.10, (c) 0.20 and (d) 0.30 m with a solid mass flux of 750 kg/m^2 s at five different reducing pressures.

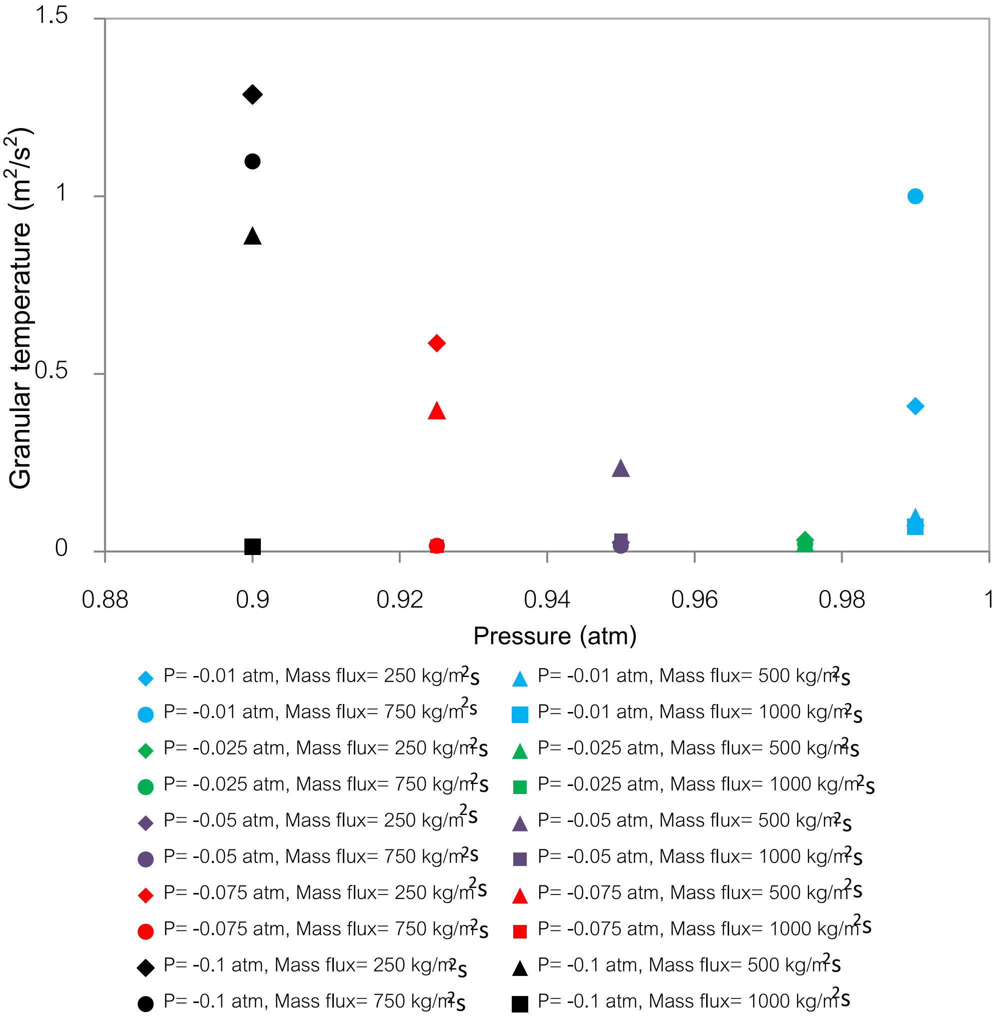

Fig. 6. 19 The comparison of the averaged total granular temperatures at four different mass fluxes with five reducing pressures.

Table 6. 1 Parameters used in this study.

Symbol	*Description*	*Value*
D_i	Inlet diameter of downer reactor (m)	0.20
D_o	Outlet diameter of downer reactor (m)	0.10
h	Height of downer reactor (m)	0.60
ρ_g	Gas density (kg/m^3)	1.138
μ_g	Gas viscosity (kg/m•s)	1.663e-05
ρ_s	Solid particle density (kg/m^3)	3,500
d_p	Solid particle diameter (μm)	100
v_g	Inlet gas velocity (m/s)	0.20
v_s	Inlet solid velocity (m/s)	0.18, 0.36, 0.51, 0.71
ε_s	Inlet solid volume fraction (-)	0.40
P	Pressure/Reducing pressure at outlet (atm)	0.90/-0.10, 0.925/-0.075, 0.95/ -0.05, 0.975/-0.025, 0.99/-0.01
e	Restitution coefficient between solid particles (-)	0.90
e_w	Restitution coefficient between solid particle and wall(-)	0.95
ϕ	Specularity coefficient (-)	0.50

Chapter VII

Conclusion and Recommendations

7.1 An investigation of circulating-turbulent fluidized bed flow regime (C-TFB) and CO_2 adsorption

The investigations of the pressure drop profile at different height in the axial direction of the riser were obtained for observing the circulating-turbulent fluidization regimes (C-TFB) solid volume fraction profile. The hydrodynamic behavior of the C-TFB provided that the solid volume fraction show uniformly along the bed height at the gas velocity at 1.0 m/s. For CO_2 capture study, C-TFB regime provided the highest CO_2 adsorption capacity. Moreover, C-TFB fluidization regime provided similar breakthrough curve pattern and values of k_0 and k_d with bubbling fluidized bed.

7.2 Chemical Kinetic for regeneration of potassium carbonate solid sorbent using temperature

Non-isothermal kinetic methods of the decomposition of potassium hydrogen carbonate ($KHCO_3$) were investigated by a thermogravimetry (TG) and Differential thermogravimetry (DTG). The kinetic parameter including the order of reaction (n), the pre-exponential factor (A) and activation energy (Ea) using four different models were obtained in this study. The results showed that the analytical method provided the most accurate results comparing with KAS, FWO and Kim-Park methods. Comparing to the experimental data, the R-squares for analytical method were higher than 0.95 for all the heating rates.

7.3 Two-dimensional CFD Design of a Sorber for CO_2 Capture

In this study, a fluidized bed of two binary mixtures of 75 and 375 μm particles carbonate based sorber design for removal of CO_2 from flue gases was investigated. CFD simulation of a binary mixture showed that a plug flow model is a good first approximation for the bubble-free fluidization achieved using two binary mixtures of 75 and 375 μm particles. In addition, the CO_2 capture from flue gas could be computed using a plug flow model. The computation of wall-to-bed heat transfer coefficients used in CFD model needed for an optimization design. Due to the equilibrium limitations, the several stages sorber are required for 90% CO_2 removal.

For a 75 μm binary mixture of a carbonate sorbent fluidized in a batch bed, bubbles appeared initially similar to spouted bed behavior. A binary mixture of 375 μm particles fluidized as an oscillating bed without bubble formation. The CO_2 capture for this oscillating bed was better than that computed from the plug flow solution.

7.4 Two-dimensional CFD simulation of reducing operating pressure effect on the system hydrodynamics in a downer reactor

The 2D CFD-based hydrodynamics simulation was used for evaluating in a CFBD reactor with five reduced operating pressures (0.90–0.99 atm) and four different solid mass fluxes (250–1000 kg/m^2s). The simulation results demonstrated that the CFBD reactor with a low solid mass flux (250 kg/m^2s) had a greater ability of the solid particles to move than when operated at a high solid mass flux condition. With respect to the effect of the reduced operating pressure, the large difference between the operating pressure and atmospheric pressure gave high system turbulence or oscillation, and accordingly a good solid circulation between gas and solid particles, as seen from the solid volume fraction, solid particle velocities, normal Reynolds stresses and granular temperature. In this study, the suitable mass flux was found to be between 500 to 750 kg/m^2s in terms of providing the appropriate solid particle amount and mixing in the system. However, this is only a preliminary study for the CFBD reactor under a reduced operating pressure.

Therefore, further studies should be performed to find the feasibility and appropriateness of the CFBD reactor under a reduced operating pressure.

7.5 Recommendations

In this study, a circulating-turbulent fluidized bed regime with K_2CO_3/Al_2O_3 solid sorbent was prepared by conventional impregnation method show a good performance for CO_2 capture from a wet flue gas. For further study, the suggestions are shown as follow,

1. To apply the concept of the CO_2 capture from emitted flue gas using K_2CO_3 solid sorbent for a large scale fluidized bed reactor, the dimensionless scaling parameters were used for investigation. However, there are more parameters need to be investigated such as heat transfer, pressure balancing of the closed loop system and the system design of the connected system.
2. To simulate a circulating-turbulent fluidized bed system, kinetic models of adsorption and desorption of the K_2CO_3/Al_2O_3 solid sorbent obtained in this study should be included in the next generation model.

REFERENCES

[1] D. Nikomborirak, “Gas in Thailand1,” 2011.

[2] S. C. Lee, and J. C. Kim, “Dry potassium-based sorbents for CO2 capture,” *Catalysis Surveys from Asia,* vol. 11, no. 4, pp. 171-185, 2007.

[3] C. Zhao, X. Chen, and C. Zhao, “CO2 absorption using dry potassium-based sorbents with different supports,” *Energy & Fuels,* vol. 23, no. 9, pp. 4683-4687, 2009.

[4] Y. Liang, D. Harrison, R. Gupta, D. Green, and W. McMichael, “Carbon dioxide capture using dry sodium-based sorbents,” *Energy & Fuels,* vol. 18, no. 2, pp. 569-575, 2004.

[5] C. K. Yi, “Development of Na and K-based sorbents for CO2 capture from flue gas,” 2005.

[6] S. C. Lee, B. Y. Choi, C. K. Ryu, Y. S. Ahn, T. J. Lee, and J. C. Kim, “The effect of water on the activation and the CO2 capture capacities of alkali metal-based sorbents,” *Korean Journal of Chemical Engineering,* vol. 23, no. 3, pp. 374-379, 2006.

[7] S. C. Lee, Y. M. Kwon, C. Y. Ryu, H. J. Chae, D. Ragupathy, S. Y. Jung, J. B. Lee, C. K. Ryu, and J. C. Kim, “Development of new alumina-modified sorbents for CO 2 sorption and regeneration at temperatures below 200 C,” *Fuel,* vol. 90, no. 4, pp. 1465-1470, 2011.

[8] C.-K. Yi, S.-H. Jo, Y. Seo, J.-B. Lee, and C.-K. Ryu, “Continuous operation of the potassium-based dry sorbent CO 2 capture process with two fluidized-bed reactors,” *International Journal of Greenhouse Gas Control,* vol. 1, no. 1, pp. 31-36, 2007.

[9] P. Khongprom, and D. Gidaspow, “Compact fluidized bed sorber for CO 2 capture,” *Particuology,* vol. 8, no. 6, pp. 531-535, 2010.

[10] D. Gidaspow, and M. Onischak, "Process for regenerative sorption of CO {HD 2," Google Patents, 1975.

[11] M. Onischak, and D. Gidaspow, “Separation of Gaseous Mixtures by Regenerative Sorption on Porous Solids: Part II. Regenerative Separation of CO 2,” *Recent developments in separation science,* vol. 2, pp. 72-93, 1972.

[12] Y. C. Park, S.-H. Jo, K.-W. Park, Y. S. Park, and C.-K. Yi, “Effect of bed height on the carbon dioxide capture by carbonation/regeneration cyclic operations using dry potassium-based sorbents,” *Korean Journal of Chemical Engineering,* vol. 26, no. 3, pp. 874-878, 2009.

[13] D. Kunii, and O. Levenspiel, *Fluidization engineering*: Elsevier, 2013.

[14] H. Zhu, and J. Zhu, “Comparative study of flow structures in a circulating-turbulent fluidized bed,” *Chemical Engineering Science,* vol. 63, no. 11, pp. 2920-2927, 2008.

[15] J. Parssinen, and J. Zhu, “Axial and radial solids distribution in a long and high-flux CFB riser,” *American Institute of Chemical Engineers. AIChE Journal,* vol. 47, no. 10, pp. 2197, 2001.

[16] J. Bastos, L. Rosa, M. Mori, F. Marini, and W. Martignoni, “Modelling and simulation of a gas–solids dispersion flow in a high-flux circulating fluidized bed (HFCFB) riser,” *Catalysis Today,* vol. 130, no. 2, pp. 462-470, 2008.

[17] H. Zhu, and J. Zhu, “Gas‐solids flow structures in a novel circulating‐turbulent fluidized bed,” *AIChE journal,* vol. 54, no. 5, pp. 1213-1223, 2008.

[18] S. Cloete, S. Amini, and S. T. Johansen, “A fine resolution parametric study on the numerical simulation of gas–solid flows in a periodic riser section,” *Powder Technology,* vol. 205, no. 1, pp. 103-111, 2011.

[19] M. Wang, A. Lawal, P. Stephenson, J. Sidders, and C. Ramshaw, “Post-combustion CO 2 capture with chemical absorption: a state-of-the-art review,” *Chemical Engineering Research and Design,* vol. 89, no. 9, pp. 1609-1624, 2011.

[20] B. Buhre, L. Elliott, C. Sheng, R. Gupta, and T. Wall, “Oxy-fuel combustion technology for coal-fired power generation,” *Progress in energy and combustion science,* vol. 31, no. 4, pp. 283-307, 2005.

[21] L.-S. Fan, *Chemical looping systems for fossil energy conversions*: John Wiley & Sons, 2011.

[22] S. Chakravarti, A. Gupta, and B. Hunek, "Advanced technology for the capture of carbon dioxide from flue gases." pp. 15-17.

[23] H. Hikita, S. Asai, Y. Katsu, and S. Ikuno, “Absorption of carbon dioxide into aqueous monoethanolamine solutions,” *AIChE Journal,* vol. 25, no. 5, pp. 793-800, 1979.

[24] P. Singh, *Amine based solvent for CO2 absorption" From molecular structure to process"*: University of Twente, 2011.

[25] R. S. Haszeldine, “Carbon capture and storage: how green can black be?,” *Science,* vol. 325, no. 5948, pp. 1647-1652, 2009.

[26] A. Aroonwilas, and A. Veawab, “Integration of CO 2 capture unit using single- and blended-amines into supercritical coal-fired power plants: implications for emission and energy management,” *International Journal of Greenhouse Gas Control,* vol. 1, no. 2, pp. 143-150, 2007.

[27] S. Sircar, “Pressure swing adsorption,” *Industrial & engineering chemistry research,* vol. 41, no. 6, pp. 1389-1392, 2002.

[28] A. Fuderer, and E. Rudelstorfer, "Selective adsorption process," Google Patents, 1976.

[29] M. Babicki, and A. Hall, “PSA technology,” *CHEMICAL PROCESSING,* vol. 66, no. 8, pp. 39-+, 2003.

[30] R. A. Khatri, S. S. Chuang, Y. Soong, and M. Gray, “Carbon dioxide capture by diamine-grafted SBA-15: A combined Fourier transform infrared and mass spectrometry study,” *Industrial & Engineering Chemistry Research,* vol. 44, no. 10, pp. 3702-3708, 2005.

[31] Z. Zhao, X. Cui, J. Ma, and R. Li, “Adsorption of carbon dioxide on alkali-modified zeolite 13X adsorbents,” *International Journal of Greenhouse Gas Control,* vol. 1, no. 3, pp. 355-359, 2007.

[32] D. M. Ruthven, *Principles of adsorption and adsorption processes*: John Wiley & Sons, 1984.

[33] C.-H. Huang, K.-P. Chang, C.-T. Yu, P.-C. Chiang, and C.-F. Wang, “Development of high-temperature CO 2 sorbents made of CaO-based mesoporous silica,” *Chemical Engineering Journal,* vol. 161, no. 1, pp. 129-135, 2010.

[34] S. C. Lee, H. J. Chae, S. J. Lee, B. Y. Choi, C. K. Yi, J. B. Lee, C. K. Ryu, and J. C. Kim, “Development of regenerable MgO-based sorbent promoted with K2CO3 for CO2 capture at low temperatures,” *Environmental science & technology,* vol. 42, no. 8, pp. 2736-2741, 2008.

[35] S. S. Burt, A. Baxter, C. Bence, and L. L. Baxter, "Cryogenic CO2 capture for improved efficiency at reduced cost."

[36] M. van Sint Annaland, M. Tuinier, and F. Gallucci, “Cryogenic CO2 Capture,” *Process Intensification for Sustainable Energy Conversion*, pp. 7, 2015.

[37] A. A. Olajire, “CO 2 capture and separation technologies for end-of-pipe applications–a review,” *Energy,* vol. 35, no. 6, pp. 2610-2628, 2010.

[38] D. Gidaspow, J. Jung, and R. K. Singh, “Hydrodynamics of fluidization using kinetic theory: an emerging paradigm: 2002 Flour-Daniel lecture,” *Powder Technology,* vol. 148, no. 2, pp. 123-141, 2004.

[39] S. Ergun, “Fluid flow through packed columns,” *Chemical engineering progress,* vol. 48, 1952.

[40] C. Wen, and Y. Yu, “A generalized method for predicting the minimum fluidization velocity,” *AIChE Journal,* vol. 12, no. 3, pp. 610-612, 1966.

[41] J. Grace, “Fluidized bed hydrodynamics,” *Handbook of multiphase systems,* vol. 5, 1982.

[42] D. Geldart, and A. R. Abrahamsen, “Homogeneous fluidization of fine powders using various gases and pressures,” *Powder Technology,* vol. 19, no. 1, pp. 133-136, 1978.

[43] P. Basu, *Combustion and gasification in fluidized beds*: CRC press, 2006.

[44] P. S. B. Stewart, and J. Davidson, “Slug flow in fluidised beds,” *Powder Technology,* vol. 1, no. 2, pp. 61-80, 1967.

[45] J. Yerushalmi, and N. Cankurt, “Further studies of the regimes of fluidization,” *Powder Technology,* vol. 24, no. 2, pp. 187-205, 1979.

[46] V. Jiradilok, D. Gidaspow, S. Damronglerd, W. J. Koves, and R. Mostofi, “Kinetic theory based CFD simulation of turbulent fluidization of FCC particles in a riser,” *Chemical Engineering Science,* vol. 61, no. 17, pp. 5544-5559, 2006.

[47] H. Bi, and J. Grace, “Effect of measurement method on the velocities used to demarcate the onset of turbulent fluidization,” *The Chemical Engineering Journal and the Biochemical Engineering Journal,* vol. 57, no. 3, pp. 261-271, 1995.

[48] M. Tsukada, D. Nakanishi, and M. Horio, “The effect of pressure on the phase transition from bubbling to turbulent fluidization,” *International journal of multiphase flow,* vol. 19, no. 1, pp. 27-34, 1993.

[49] M. Tsukada, D. Nakanishi, and M. Horio, “Effect of Pressure on'Transport Velocity'in a Circulating Fluidized Bed,” *Proceedings, Circulating Fluidized Bed Technology IV, AA Avidan, ed., AIChE, NY,* pp. 209-215, 1993.

[50] J. Yerushalmi, D. H. Turner, and A. M. Squires, “The fast fluidized bed,” *Industrial & Engineering Chemistry Process Design and Development,* vol. 15, no. 1, pp. 47-53, 1976.

[51] A. Avidan, and J. Yerushalmi, “Bed expansion in high velocity fluidization,” *Powder Technology,* vol. 32, no. 2, pp. 223-232, 1982.

[52] Y. Li, and M. Kwauk, "The dynamics of fast fluidization," *Fluidization*, pp. 537-544: Springer, 1980.

[53] C. Capes, and K. Nakamura, “Vertical pneumatic conveying: a theoretical study of uniform and annular particle flow models,” *The Canadian Journal of Chemical Engineering,* vol. 51, no. 1, pp. 39-46, 1973.

[54] K. Smolders, and J. Baeyens, “Gas fluidized beds operating at high velocities: a critical review of occurring regimes,” *Powder Technology,* vol. 119, no. 2, pp. 269-291, 2001.

[55] N. Balasubramanian, C. Srinivasakannan, and C. A. Basha, “Transition velocities in the riser of a circulating fluidized bed,” *Advanced Powder Technology,* vol. 16, no. 3, pp. 247-260, 2005.

[56] H. Bi, J. Grace, and J. Zhu, “Types of choking in vertical pneumatic systems,” *International Journal of Multiphase Flow,* vol. 19, no. 6, pp. 1077-1092, 1993.

[57] H. Bi, and L. Fan, "Regime transition in gas-solid circulating fluidized beds." p. 17.

[58] J. R. Grace, and H. Bi, "Introduction to circulating fluidized beds," *Circulating Fluidized Beds*, pp. 1-20: Springer, 1997.

[59] P. C. Johnson, and R. Jackson, “Frictional–collisional constitutive relations for granular materials, with application to plane shearing,” *Journal of Fluid Mechanics,* vol. 176, pp. 67-93, 1987.

[60] A. S. Issangya, J. R. Grace, D. Bai, and J. Zhu, “Further measurements of flow dynamics in a high-density circulating fluidized bed riser,” *Powder Technology,* vol. 111, no. 1, pp. 104-113, 2000.

[61] J. R. Grace, A. S. Issangya, D. Bai, H. Bi, and J. Zhu, “Situating the high‐density circulating fluidized bed,” *AIChE Journal,* vol. 45, no. 10, pp. 2108-2116, 1999.

[62] M. Durán-Guevara, J. Ortiz-Landeros, H. Pfeiffer, M. Espitia-Cabrera, and M. Contreras-García, “Potassium-based sorbents using mesostructured γ-alumina supports for low temperature CO 2 capture,” *Ceramics International,* vol. 41, no. 2, pp. 3036-3044, 2015.

[63] H. Luo, H. Chioyama, S. Thürmer, T. Ohba, and H. Kanoh, “Kinetics and Structural Changes in CO2 Capture of K2CO3 under a Moist Condition,” *Energy & Fuels,* vol. 29, no. 7, pp. 4472-4478, 2015.

[64] "POST-COMBUSTION CAPTURE OF CARBON DIOXIDE," 2015 June 13, 2015; http://www.co2crc.com.au/dls/factsheets/Post_comb_Solvent.pdf.

[65] S. Choi, Y. S. Kim, D. S. Park, S. J. Kim, J. M. Kim, H. C. Kim, S. H. Oh, T.-J. Kim, and D. H. Choo, "Catalytic cracking process using fast fluidization for the production of light olefins from hydrocarbon feedstock," Google Patents, 2012.

[66] D. Kunii, and O. Levenspiel, "Flow modeling of fast fluidized beds," *Circulating Fluidized Bed Technology III*, pp. 91-98: Pergamon Press Oxford, 1991.

[67] P. Basu, and S. A. Fraser, *Circulating fluidized bed boilers*: Springer, 1991.

[68] C. Zhao, X. Chen, C. Zhao, and Y. Liu, "Carbonation and hydration characteristics of dry potassium-based sorbents for CO2 capture," *Energy & Fuels,* vol. 23, no. 3, pp. 1766-1769, 2009.

[69] O.-a. Jaiboon, B. Chalermsinsuwan, L. Mekasut, and P. Piumsomboon, "Effect of flow patterns/regimes on CO 2 capture using K 2 CO 3 solid sorbent in fluidized bed/circulating fluidized bed," *Chemical engineering journal,* vol. 219, pp. 262-272, 2013.

[70] V. Mamleev, S. Bourbigot, and J. Yvon, "Kinetic analysis of the thermal decomposition of cellulose: the main step of mass loss," *Journal of Analytical and Applied Pyrolysis,* vol. 80, no. 1, pp. 151-165, 2007.

[71] K. Slopiecka, P. Bartocci, and F. Fantozzi, "Thermogravimetric analysis and kinetic study of poplar wood pyrolysis," *Applied Energy,* vol. 97, pp. 491-497, 2012.

[72] H. E. Kissinger, "Reaction kinetics in differential thermal analysis," *Analytical chemistry,* vol. 29, no. 11, pp. 1702-1706, 1957.

[73] T. Akahira, and T. Sunose, "Method of determining activation deterioration constant of electrical insulating materials," *Res Rep Chiba Inst Technol (Sci Technol),* vol. 16, pp. 22-31, 1971.

[74] C.-P. Lin, Y.-M. Chang, J. P. Gupta, and C.-M. Shu, "Comparisons of TGA and DSC approaches to evaluate nitrocellulose thermal degradation energy and stabilizer efficiencies," *Process Safety and Environmental Protection,* vol. 88, no. 6, pp. 413-419, 2010.

[75] J. H. Flynn, and L. A. Wall, "General treatment of the thermogravimetry of polymers," *J Res Nat Bur Stand,* vol. 70, no. 6, pp. 487-523, 1966.

[76] T. Ozawa, "A new method of analyzing thermogravimetric data," *Bulletin of the chemical society of Japan,* vol. 38, no. 11, pp. 1881-1886, 1965.

[77] C. Doyle, “Kinetic analysis of thermogravimetric data,” *Journal of applied polymer science,* vol. 5, no. 15, pp. 285-292, 1961.

[78] C. Doyle, “Estimating isothermal life from thermogravimetric data,” *Journal of Applied Polymer Science,* vol. 6, no. 24, pp. 639-642, 1962.

[79] S. Kim, and J. K. Park, “Characterization of thermal reaction by peak temperature and height of DTG curves,” *Thermochimica acta,* vol. 264, pp. 137-156, 1995.

[80] W. Tang, X. G. Li, and D. Yan, “Thermal decomposition kinetics of thermotropic copolyesters made from trans-p-hydroxycinnamic acid and p-hydroxybenzoic acid,” *Journal of applied polymer science,* vol. 91, no. 1, pp. 445-454, 2004.

[81] G. Zhu, X. Zhu, Z. Xiao, and F. Yi, “Study of cellulose pyrolysis using an in situ visualization technique and thermogravimetric analyzer,” *Journal of Analytical and Applied Pyrolysis,* vol. 94, pp. 126-130, 2012.

[82] I. C. Hisatsune, and T. Adl, “Thermal decomposition of potassium bicarbonate,” *The Journal of Physical Chemistry,* vol. 74, no. 15, pp. 2875-2877, 1970.

[83] A. Khawam, and D. R. Flanagan, “Role of isoconversional methods in varying activation energies of solid-state kinetics: II. Nonisothermal kinetic studies,” *Thermochimica Acta,* vol. 436, no. 1, pp. 101-112, 2005.

[84] M. Syamlal, and D. Gidaspow, “Hydrodynamics of fluidization: prediction of wall to bed heat transfer coefficients,” *AIChE Journal,* vol. 31, no. 1, pp. 127-135, 1985.

[85] G. T. Rochelle, “Amine scrubbing for CO2 capture,” *Science,* vol. 325, no. 5948, pp. 1652-1654, 2009.

[86] M. S. Jassim, and G. T. Rochelle, “Innovative absorber/stripper configurations for CO2 capture by aqueous monoethanolamine,” *Industrial & Engineering Chemistry Research,* vol. 45, no. 8, pp. 2465-2472, 2006.

[87] N. Holt, W. Owens, T. Buchanan, M. DeLallo, R. Schoff, J. White, and R. Wolk, “Evaluation of innovative fossil fuel power plants with CO2 removal,” *Electric Power Research Institute, Palo Alto, CA*, 2000.

[88] S. Freguia, and G. T. Rochelle, “Modeling of CO2 capture by aqueous monoethanolamine,” *AIChE Journal,* vol. 49, no. 7, pp. 1676-1686, 2003.

[89] M. Onischak, and D. Gidaspow, "Kinetics of the reaction of CO2 with solid K2CO3."

[90] T. O. Nelson, L. J. Coleman, D. A. Green, and R. P. Gupta, “The dry carbonate process: carbon dioxide recovery from power plant flue gas,” *Energy Procedia,* vol. 1, no. 1, pp. 1305-1311, 2009.

[91] B. Chalermsinsuwan, P. Piumsomboon, and D. Gidaspow, “A computational fluid dynamics design of a carbon dioxide sorption circulating fluidized bed,” *AIChE journal,* vol. 56, no. 11, pp. 2805-2824, 2010.

[92] S. Kongkitisupchai, “Carbon dioxide capture using solid sorbents in a fluidized bed with reduced pressure regeneration in a downer,” Illinios Institue of Technology, Chicago, 2012.

[93] S. Kongkitisupchai, and D. Gidaspow, “Carbon dioxide capture using solid sorbents in a fluidized bed with reduced pressure regeneration in a downer,” *AIChE Journal,* vol. 59, no. 12, pp. 4519-4537, 2013.

[94] C. C. Templeton, “Pressure-temperature relationship for decomposition of sodium bicarbonate from 200 to 600. degree. F,” *Journal of Chemical and Engineering Data,* vol. 23, no. 1, pp. 7-11, 1978.

[95] Z. Zhang, X. Ma, D. Wang, C. Song, and Y. Wang, “Development of silica-gel-supported polyethylenimine sorbents for CO2 capture from flue gas,” *AIChE Journal,* vol. 58, no. 8, pp. 2495-2502, 2012.

[96] C. Petit, and A.-H. A. Park, "Tuning the Physical and Chemical Properties of Novel CO2 Capture Solvents based on Hybrid Nanomaterials."

[97] D. Gidaspow, “Separation of Gaseous Mixtures by Regenerative Sorption on Porous Solids. Part I—A Fluid Porous Solid Reaction Model with Structural Changes,” *Recent Developments in Separation Science,* vol. 2, pp. 59-70, 1972.

[98] M. Syamlal, and T. J. O'Brien, “Fluid dynamic simulation of O3 decomposition in a bubbling fluidized bed,” *AIChE Journal,* vol. 49, no. 11, pp. 2793-2801, 2003.

[99] D. Gidaspow, and P. Chaiwang, “Bubble free fluidization of a binary mixture of large particles,” *Chemical Engineering Science,* vol. 97, pp. 152-161, 2013.

[100] L. Raynal, F. B. Rayana, and A. Royon-Lebeaud, “Use of CFD for CO 2 absorbers optimum design: from local scale to large industrial scale,” *Energy Procedia,* vol. 1, no. 1, pp. 917-924, 2009.

[101] C. Gentric, D. Mignon, J. Bousquet, and P. Tanguy, “Comparison of mixing in two industrial gas–liquid reactors using CFD simulations,” *Chemical engineering science,* vol. 60, no. 8, pp. 2253-2272, 2005.

[102] P. J. Stopford, “Recent applications of CFD modelling in the power generation and combustion industries,” *Applied Mathematical Modelling,* vol. 26, no. 2, pp. 351-374, 2002.

[103] D. Barthod, M. Del Pozo, and C. Mirgain, “CFD-aided design improves FCC performance,” *Oil & gas journal,* vol. 97, no. 14, pp. 66-69, 1999.

[104] A. Almuttahar, and F. Taghipour, “Computational fluid dynamics of high density circulating fluidized bed riser: Study of modeling parameters,” *Powder Technology,* vol. 185, no. 1, pp. 11-23, 2008.

[105] L. Huilin, H. Yurong, and D. Gidaspow, “Hydrodynamic modelling of binary mixture in a gas bubbling fluidized bed using the kinetic theory of granular flow,” *Chemical Engineering Science,* vol. 58, no. 7, pp. 1197-1205, 2003.

[106] M. Goldschmidt, J. Kuipers, and W. Van Swaaij, “Hydrodynamic modelling of dense gas-fluidised beds using the kinetic theory of granular flow: effect of coefficient of restitution on bed dynamics,” *Chemical Engineering Science,* vol. 56, no. 2, pp. 571-578, 2001.

[107] D. Gidaspow, *Multiphase flow and fluidization: continuum and kinetic theory descriptions*: Academic press, 1994.

[108] V. V. Ranade, *Computational flow modeling for chemical reactor engineering*: Academic press, 2001.

[109] C. Crowe, M. Sommerfeld, and Y. Tsuji, "Multiphase flows with particles and droplets," CRC Press, New York, 1998.

[110] C. S. Campbell, and C. E. Brennen, “Computer simulation of granular shear flows,” *Journal of Fluid Mechanics,* vol. 151, pp. 167-188, 1985.

[111] Y. Wang, and M. T. Mason, “Two-dimensional rigid-body collisions with friction,” *Journal of Applied Mechanics,* vol. 59, no. 3, pp. 635-642, 1992.

[112] P. A. Cundall, and O. D. Strack, “A discrete numerical model for granular assemblies,” *Geotechnique,* vol. 29, no. 1, pp. 47-65, 1979.

[113] Y. Tsuji, T. Kawaguchi, and T. Tanaka, “Discrete particle simulation of two-dimensional fluidized bed,” *Powder technology,* vol. 77, no. 1, pp. 79-87, 1993.

[114] G. Gouesbet, and A. Berlemont, “Eulerian and Lagrangian approaches for predicting the behaviour of discrete particles in turbulent flows,” *Progress in Energy and Combustion Science,* vol. 25, no. 2, pp. 133-159, 1999.

[115] J. Shirolkar, C. Coimbra, and M. Q. McQuay, “Fundamental aspects of modeling turbulent particle dispersion in dilute flows,” *Progress in Energy and Combustion Science,* vol. 22, no. 4, pp. 363-399, 1996.

[116] M. Rhodes, X. Wang, M. Nguyen, P. Stewart, and K. Liffman, “Use of discrete element method simulation in studying fluidization characteristics: influence of interparticle force,” *Chemical Engineering Science,* vol. 56, no. 1, pp. 69-76, 2001.

[117] K. Kuwagi, T. Mikami, and M. Horio, “Numerical simulation of metallic solid bridging particles in a fluidized bed at high temperature,” *Powder Technology,* vol. 109, no. 1, pp. 27-40, 2000.

[118] S. Limtrakul, A. Chalermwattanatai, K. Unggurawirote, Y. Tsuji, T. Kawaguchi, and W. Tanthapanichakoon, “Discrete particle simulation of solids motion in a gas–solid fluidized bed,” *Chemical Engineering Science,* vol. 58, no. 3, pp. 915-921, 2003.

[119] Y. Kaneko, T. Shiojima, and M. Horio, “DEM simulation of fluidized beds for gas-phase olefin polymerization,” *Chemical Engineering Science,* vol. 54, no. 24, pp. 5809-5821, 1999.

[120] X. Wang, and M. Rhodes, "Determination of particle residence time at the walls of gas fluidized beds by discrete element method simulation," *Chemical Engineering Science,* vol. 58, no. 2, pp. 387-395, 2003.

[121] N. Deen, M. V. S. Annaland, M. Van der Hoef, and J. Kuipers, "Review of discrete particle modeling of fluidized beds," *Chemical Engineering Science,* vol. 62, no. 1, pp. 28-44, 2007.

[122] A. Miller, and D. Gidaspow, "Dense, vertical gas-solid flow in a pipe," *AIChE journal,* vol. 38, no. 11, pp. 1801-1815, 1992.

[123] B. Sun, and D. Gidaspow, "Computation of circulating fluidized-bed riser flow for the fluidization VIII benchmark test," *Industrial & engineering chemistry research,* vol. 38, no. 3, pp. 787-792, 1999.

[124] L. Huilin, and D. Gidaspow, "Hydrodynamics of binary fluidization in a riser: CFD simulation using two granular temperatures," *Chemical Engineering Science,* vol. 58, no. 16, pp. 3777-3792, 2003.

[125] X. Gao, C. Wu, Y.-w. Cheng, L.-j. Wang, and X. Li, "Experimental and numerical investigation of solid behavior in a gas–solid turbulent fluidized bed," *Powder technology,* vol. 228, pp. 1-13, 2012.

[126] F. Inc, "Fluent 6.2 User's Guide," 2005a.

[127] D. Gunn, "Transfer of heat or mass to particles in fixed and fluidised beds," *International Journal of Heat and Mass Transfer,* vol. 21, no. 4, pp. 467-476, 1978.

[128] S. Chapman, and T. G. Cowling, *The mathematical theory of non-uniform gases: an account of the kinetic theory of viscosity, thermal conduction and diffusion in gases*: Cambridge university press, 1970.

[129] J. Jenkins, and S. Savage, "A theory for the rapid flow of identical, smooth, nearly elastic, spherical particles," *Journal of Fluid Mechanics,* vol. 130, pp. 187-202, 1983.

[130] C. Lun, S. B. Savage, D. Jeffrey, and N. Chepurniy, “Kinetic theories for granular flow: inelastic particles in Couette flow and slightly inelastic particles in a general flowfield,” *Journal of fluid mechanics,* vol. 140, pp. 223-256, 1984.

[131] D. Gidaspow, and V. Jiradilok, *Computational techniques: The multiphase CFD approach to fluidization and green energy technologies*: Nova Science Publishers, 2009.

[132] Z. Wang, H. Bi, and C. Lim, “CFD simulation of spouted beds using a pressure source term,” *Industrial & Engineering Chemistry Research,* vol. 49, no. 11, pp. 5053-5060, 2009.

[133] A. Xavier, and J. Davidson, “Heat transfer in fluidized beds: convective heat transfer in fluidized beds,” *Fluidization*, pp. 437, 1985.

[134] M. L. Roesle, and F. A. Kulacki, "Measurement of Heat Transfer Coefficients in a Boiling Emulsion," *Boiling Heat Transfer in Dilute Emulsions*, pp. 71-96: Springer, 2013.

[135] J. Kuipers, W. Prins, and W. Van Swaaij, “Numerical calculation of wall-to-bed heat-transfer coefficients in gas-fluidized beds,” *AIChE Journal,* vol. 38, no. 7, pp. 1079-1091, 1992.

[136] C.-K. Yi, S. Jo, Y. Seo, S. Park, K. Moon, J. Yoo, J. Lee, and C. Ryu, “CO 2 capture characteristics of dry sorbents in a fast fluidized reactor,” *Studies in surface science and catalysis,* vol. 159, pp. 501-504, 2006.

[137] L. Li, Y. Li, X. Wen, F. Wang, N. Zhao, F. Xiao, W. Wei, and Y. Sun, “CO2 capture over K2CO3/MgO/Al2O3 dry sorbent in a fluidized bed,” *Energy and Fuels,* vol. 25, no. 8, pp. 3835, 2011.

[138] S. C. Lee, B. Y. Choi, T. J. Lee, C. K. Ryu, Y. S. Ahn, and J. C. Kim, “CO 2 absorption and regeneration of alkali metal-based solid sorbents,” *Catalysis Today,* vol. 111, no. 3, pp. 385-390, 2006.

[139] Y. Cheng, Y. Guo, F. Wei, Y. Jin, and W. Lin, “Modeling the hydrodynamics of downer reactors based on kinetic theory,” *Chemical Engineering Science,* vol. 54, no. 13, pp. 2019-2027, 1999.

[140] F. Wei, and J.-X. Zhu, “Effect of flow direction on axial solid dispersion in gas—solids cocurrent upflow and downflow systems,” *The Chemical Engineering Journal and the Biochemical Engineering Journal,* vol. 64, no. 3, pp. 345-352, 1996.

[141] K. Ropelato, H. F. Meier, and M. A. Cremasco, “CFD study of gas–solid behavior in downer reactors: an Eulerian–Eulerian approach,” *Powder technology,* vol. 154, no. 2, pp. 179-184, 2005.

[142] T. Samruamphianskun, P. Piumsomboon, and B. Chalermsinsuwan, “Computation of system turbulences and dispersion coefficients in circulating fluidized bed downer using CFD simulation,” *Chemical Engineering Research and Design,* vol. 90, no. 12, pp. 2164-2178, 2012.

[143] X. Lan, W. Yan, C. Xu, J. Gao, and Z.-H. Luo, “Hydrodynamics of gas–solid turbulent fluidized bed of polydisperse binary particles,” *Powder Technology,* vol. 262, pp. 106-123, 2014.

[144] G.-Q. Chen, and Z.-H. Luo, “New insights into intraparticle transfer, particle kinetics, and gas–solid two-phase flow in polydisperse fluid catalytic cracking riser reactors under reaction conditions using multi-scale modeling,” *Chemical Engineering Science,* vol. 109, pp. 38-52, 2014.

[145] J. Jung, D. Gidaspow, and I. K. Gamwo, “Bubble computation, granular temperatures, and Reynolds stresses,” *Chemical Engineering Communications,* vol. 193, no. 8, pp. 946-975, 2006.

[146] B. Chalermsinsuwan, P. Piumsomboon, and D. Gidaspow, “Kinetic theory based computation of PSRI riser: Part I—Estimate of mass transfer coefficient,” *Chemical Engineering Science,* vol. 64, no. 6, pp. 1195-1211, 2009.

Appendix A

Conceptual design and well-mixed model

A1. Conceptual Design

Nelson et al. of RTI International (2009) demonstrated that solid 70 μm Na_2CO_3 sorbents are useful for capturing CO_2 from power plant flue gases. Their CO_2 absorber was a bubbling bed. Without heat removal, the temperature in a bubbling bed will rise to the decomposition temperature of the carbonate and the reaction will stop. The steady state temperature rise in the fluidized bed is given by the equation shown below (see Appendix A)

$$T_{Bed} - T_W = \frac{\Delta H \left(Y_{CO_2,out} - Y_{CO_2,in}\right)}{Cp} - \frac{\dot{q}}{\dot{w}Cp} \qquad \text{(A1)}$$

where ΔH is the heat of reaction, as shown in Figure 3.1, Y is the weight fraction of CO_2, C_p is the specific heat of the flue gas, $\dot{q}$ is the rate of the heat removal and $\dot{w}$ is the mass flow rate of the flue gas. Without heat removal, the temperature rise is about 750°C, since the heat of reaction, as shown in Figure 3.1 is about 1/3 that of combustion of coal. This heat of reaction must be recovered in the regeneration process. To keep the temperature rise in Eq (A1) to a few degrees requires a large surface area. In a fluidized bed combustor, this is done by inserting tubes into the reactor. These cooling tubes erode with time and will break the sorbent particles leading to high attrition. The alternative is to remove the heat as shown Figure 3.2 by placing hot water channels on both sides of thin two-dimensional fluidized beds. The hot water can then be used to supply at least part of the heat needed in the regenerator. As an alternative, the hot water channels can be replaced with sorbent regenerators.

A2: Well-mixed model

Energy Balance For The Sorber

The overall energy balance for the sorber is as follows:

$$\underbrace{\rho_g \vec{v}_g A(T_{bed} - T_{in})C_{pg}}_{\text{Net rate of energy outflow due to flow of gas}} = \underbrace{\Delta H \rho_g \vec{v}_g A(Y_{CO_2,in} - Y_{CO_2,out})}_{\text{Rate of heat generate due to reaction}} - \underbrace{\dot{q}}_{\text{Rate of heat loss through the walls}} \tag{A2}$$

In Equation (A2)

$$\dot{W} = \rho_g \vec{v}_g A \tag{A3}$$

The heat transfer coefficient, h,in Equation (9) is defined as

$$\dot{q} = A_{heat\_transfer}(T_{bed} - T_{wall}) \tag{A4}$$

This energy balance can then be used together with the plug flow reaction model to optimize the sorber system.

Appendix B

Solid volume fraction calculation

Solid volume fraction calculation

$$\varepsilon = \frac{\Delta P}{\Delta h \rho_s g}$$

when

ε = 3900 kg/m^3

ΔP = Pa

ρ_s = kg/m^3

g = 9.8 kg/s^2

Δh = m

$$\varepsilon = \frac{7401}{(0.1)(3900)(9.8)} = 0.19$$

VITA

Miss Pilaiwan Chaiwang was born on 3rd September, 1987. She graduated her Bachelor degree in Industrial Chemistry from the Faculty of Science, Chiang Mai University, Thailand. Pilaiwan started her doctorate program in the 2010 academic year in Department of Chemical Technology, Faculty of Science, Chulalongkorn University. She has received the Royal Golden Jubilee Ph.D. scholarship from Thailand Research Fund (TRF) and Chulalongkorn University (2010-2014) and Teaching Assistant Scholarship from Graduate School (2015) for her Ph.D. study.

The international publication articles entitled:

1. CFD design of a sorber for CO2 capture with 75 and 375 mircron particles has been published in Chemical Engineering Science 105 (2014): 32-45.

2. Thermogravimetric Analysis and Chemical Kinetics for Regeneration of Sodium and Potassium Carbonate Solid Sorbents. Chemical Engineering Communications 203.5 (2016): 581-588.

3. Two-Dimensional CFD Simulation of Reducing Operating Pressure Effect on the System Hydrodynamics in a Downer Reactor. ENGINEERING JOURNAL 21.2 (2016).

And Pilaiwan also presented her work in the international and national conferences:

1. System Hydrodynamics in the Circulating Fluidized Bed Downer with Reducing Pressure using 2D Computational Fluid Dynamics Simulation at Congress 9th World Congress of Chemical Engineering Incorporating 15th Asian Pacific Confederation of Chemical Engineering Congress (WCCE9 & APCChE 2013)

2. Thermogravimetric analysis and chemical kinetic for regeneration of potassium carbonate solid sorbent at 11th International Conference on Fluidized Bed Technology.